ABSTRACT

Title of Dissertation: NONLINEAR AND STOCHASTIC DYNAMICS OF OPTOELECTRONIC OSCILLATORS

Meenwook Ha
Doctor of Philosophy, 2024

Dissertation Directed by: Professor Yanne K. Chembo
Department of Electrical and Computer Engineering

Optoelectronic oscillators (OEOs) are nonlinear, time-delayed and self-sustained microwave photonic systems capable of generating ultrapure radiofrequency (RF) signals with extensive frequency tunabilities. Their hybrid architectures, comprising both optical and electronic paths, underscore their merits. One of the most notable points of OEOs can be unprecedentedly high quality factors, achieved by storing optical energies for RF signal generations. Thanks to their low phase noise and broad frequency tunabilities, OEOs have found diverse applications including chaos cryptography, reservoir computing, radar communications, parametric oscillator, clock recovery, and frequency comb generation. This thesis pursues two primary objectives. Firstly, we delve into the nonlinear dynamics of various OEO configurations, elucidating their universal behaviors by deriving corresponding envelope equations. Secondly, we present a stochastic equation delineating the dynamics of phases and explore the intricacies of the phase dynamics.

The outputs of OEOs are defined in their RF ports, with our primary focus directed towards understanding the dynamics of these RF signals. Regardless of their structural complexities,

we employ a consistent framework to explore these dynamics, relying on the same underlying principles that determine the oscillation frequencies of OEOs. To comprehend behaviors of OEOs, we analyze the dynamics of a variety of OEOs. For simpler systems, we can utilize the dynamic equations of bandpass filters, whereas more complex physics are required for expressing microwave photonic filtering. Utilizing an envelope approach, which characterizes the dynamics of OEOs in terms of complex envelopes of their RF signals, has proven to be an effective method for studying them. Consequently, we derive envelope equations of these systems and research nonlinear behaviors through analyses such as investigating bifurcations, stability evaluations, and numerical simulations. Comparing the envelope equations of different models reveals similarities in their dynamic equations, suggesting that their dynamics can be governed by a generalized universal form. Thus, we introduce the universal equation, which we refer to as the universal microwave envelope equation and conduct analytical investigations to further understand its implications.

While the deterministic universal equation offers a comprehensive tool for simultaneous exploration of various OEO dynamics, it falls short in describing the stochastic phase dynamics. Our secondary focus lies in investigating phase dynamics through the implementation of a stochastic approach, enabling us to optimize and comprehend phase noise performance effectively. We transform the deterministic universal envelope equation into a stochastic delay differential form, effectively describing the phase dynamics. In our analysis of the oscillators, we categorize noise sources into two types: additive noise contribution, due to random environmental and internal fluctuations, and multiplicative noise contribution, arising from noisy loop gains. The existence of the additive noise is independent of oscillation existence, while the multiplicative noise is intertwined with the noisy loop gains, nonlinearly mixing with signals above the threshold.

Therefore, we investigate both sub- and above-threshold regimes separately, where the multiplicative noise can be characterized as white noise and colored noise in respective regimes. For the above-threshold regime, we present the stochastic phase equation and derive an equation for describing phase noise spectra. We conduct thorough investigations into this equation and validate our approaches through experimental verification.

In the sub-threshold regime, we introduce frameworks to experimentally quantify the noise contributions discussed in the above-threshold part. Since no signal is present here and the oscillator is solely driven by the stochastic noise, it becomes feasible to reverse-engineer the noise powers using a Fourier transform formalism. Here, we introduce a stochastic expression written in terms of the real-valued RF signals, not the envelopes, and the transformation facilitates the expressions of additive and multiplicative noise contributions as functions of noisy RF output powers. The additive noise can be defined by deactivating the laser source or operating the intensity modulator at the minimum transmission point, given its independence from the loop gains. Conversely, the expression for the multiplicative noise indicates a dependence on the gain, however, experimental observations suggest that its magnitude may remain relatively constant beyond the threshold.

NONLINEAR AND STOCHASTIC DYNAMICS OF OPTOELECTRONIC OSCILLATORS

by

Meenwook Ha

Dissertation submitted to the Faculty of the Graduate School of the
University of Maryland, College Park in partial fulfillment
of the requirements for the degree of
Doctor of Philosophy
2024

Advisory Committee:
Professor Yanne K. Chembo, Chair/Advisor
Professor Thomas E. Murphy
Professor Kevin M. Daniels
Professor Cheng Gong
Professor Rajarshi Roy, Dean's Representative

Dedication

To my friends, family, and parents for always believing in me.

Acknowledgments

I would like to express my sincere gratitude to my advisor, Professor Yanne K. Chembo, for his unwavering support and guidance throughout my Ph.D. studies. His commitment to research, creativity, and responsibility has been a constant source of inspiration throughout this long journey. Working with him provided me with a priceless opportunity to learn about effective leadership, collaboration, and personal growth. I extend my heartfelt thanks to Professor Chembo for giving me the invaluable opportunity of working with him, and I take great pride in considering myself his academic protégé. His endless encouragement and support have been instrumental in making this work possible.

I would like to extend my deep appreciation to Professors Thomas E. Murphy, Kevin M. Daniels, Rajarshi Roy, and Cheng Gong for graciously serving on my dissertation committee and providing valuable feedback. It was a great honor to have them in my Ph.D. dissertation, and I consider it a unique opportunity to learn from their wealth of perspectives. Additionally, I extend my gratitude to all the faculty members with whom I have interacted at the University of Maryland, College Park.

I wish to express my appreciation to Professor C. Emre Koksal, who guided me through the *Honors Research Distinction Thesis Project* during my senior year at the Ohio State University. This marked my initiation into academic research, significantly accelerated my enthusiasm toward Ph.D. studies. This experience provided me with a comprehensive understanding of research fundamentals.

I also want to extend my sincere gratitude for the invaluable advice and guidance provided by Doctors Brian P. Ginsburg, Michael H. Perrott, and Juan A. Herbsommer during my summer internship at Kilby Labs, Texas Instruments in 2023. I learned valuable insights on effective leadership and engineering excellence from their guidance. I consider it one of the most unforgettable chapters of my life. The experience served as a turning point and a constant source of motivation.

I am thankful to all my fellow lab mates for making our lab an inspiring and collaborative environment. In particular, I extend my deepest thanks to Professor Elham Heidari for her invaluable guidance during her PostDoc period in the group. I appreciate the mutual support with Fengyu Liu since outset of our Ph.D. in August 2019.

I extend my appreciation to my dearest friends at the University of Maryland including Dr. Kyungjun Lee, Dr. Yongwan Park, Dr. Brian Kim, Dr. Yaesop Lee, Youngjoon Lee, and Muwon Kwon. Spending time with them in College Park has been an absolute pleasure, enriching my journey with happiness. Gratitude also goes to my friends beyond the university, with special thanks to Doohyun Cha. His unwavering support and dedication towards his goals have consistently served as a motivating force for me.

I owe an eternal debt of gratitude to my family for their unconditional support and care, extending beyond my Ph.D. studies to life in general. My heartfelt thanks go to my parents and my brother, who have consistently believed in me. This dissertation is dedicated to each of them.

Table of Contents

List of Figures

List of Abbreviations

BPF	Bandpass Filter
CCK	Counter Clockwise
CFBG	Chirped Fiber Bragg Grating
CK	Clockwise
DC	Direct Current
DP-MZM	Dual-Parallel Mach-Zehnder Modulator
FDL	Fiber Delay Line
FSR	Free Spectral Range
MATP	Maximum Transmission Point
MITP	Minimum Transmission Point
MPF	Microwave Photonic Filter
MZM	Mach-Zehnder Modulator
OEO	Optoelectronic Oscillator
PC	Polarization Controller
PD	Photodetector
PM	Phase Modulator
Pol	Polarizer
PSD	Power Spectral Density
QTP	Quadrature Transmission Point
RF	Radio Frequency
RFA	Radio Frequency Amplifier
RIN	Relative Intensity Noise
SBS	Stimulated Brillouin Scattering
SDDE	Stochastic Delay Differential Equation
VOA	Variable Optical Attenuator

Chapter 1: Introduction

The frequency range of microwave, typically spanning from 300 MHz to 300 GHz, holds increasing significance in contemporary communication systems due to its extensive spectral bandwidth and saturation of lower frequency ranges by existing communication networks. The demand for such frequencies is evident with the advent of 5G and the ongoing development of 6G communication technologies. Oscillators play a fundamental role in building communication links, serving as resonant devices that produce periodic oscillations matching the frequency requirements of systems. However, in the frequency regime, achieving precise frequency control becomes increasingly challenging due to the fact that the complexity of frequency controls in electronic devices escalates with higher frequencies. Therefore, as the frequency range increases, fully electronic oscillators encounter limitations in meeting requirements such as low phase noise, frequency tunability, and high frequency generation.

Optoelectronic oscillators (OEOs) are nonlinear, time-delayed and self-sustained microwave photonic systems able to generate ultrapure radiofrequency (RF) signals, which can satisfy the proposed concerns due to their extremely low phase noise and broad frequency tunabilities [1–4]. It arises from their hybrid structure, which consist of both optical and electrical paths. Between a lot of benefits from the optical path, the most significant one of these hybrid oscillators compared to fully electronic oscillators can be unprecedented high quality-factors (Q-factors) achieved through storing optical energies for RF signal generations [5–7]. In order to serve different purposes, OEOs have been developed in various configurations, and they can generally be categorized into two groups: broadband and narrowband groups, based on their spectral bandwidth.

The broad OEOs utilize their wide bandwidth in the microwave regime. A notable example within the family is chaos cryptography, wherein an audio signal is encrypted within a high dimensional chaotic fluctuations of the wavelength, enabling high-speed encrypted communication [8–10]. Additionally, broadband OEOs find applications in machine learning. The infinite dimensionality caused by time-delays and broad bandwidth allows their uses in reservoir computing, an information processing technique which projects input data into a high-dimensional space for computation purposes [11–14]. Moreover, their wide bandwidth are advantageous in radar communications, random bit generation, parametric oscillator, clock recovery, and frequency comb generation [15–20].

In the realm of the narrowband group, the OEOs primarily focus on generation of RF signals with exceptional purity. Consequently, the design of narrowband OEOs focuses on achieving high Q-factors and minimizing phase noise. In a single closed-loop system, the Q-factor of the OEO is proportional to the length of its fiber spool. For example, employing a 4 km length fiber spool yields a Q-factor greater than 10^6 at a 10 GHz oscillation, marking a truly remarkable achievement. The oscillation frequencies of OEOs typically rely on their center frequencies of narrow bandpass filters (BPFs). In order to achieve lower phase noise, the narrowband OEOs have been developed in many different ways such as having dual-loop structures, replacing fiber spools by resonators, and utilizing parity-time symmetricity [21–29].

Although OEOs have been classified into two families based on their applications, they can still be analyzed within a same framework as long as the BPFs maintain reasonable levels of narrowness. There are, however, some exceptional cases that necessitate slightly different approaches, such as those having very broad RF passband from very wide filters, using only low-pass filtering, or even not using any filter [30, 31]. Nevertheless, in most instances, even though the broad family may encompass a wider bandwidth, this breadth is considered relative to the narrow OEOs, with the broad groups still featuring limited passbands relative to their carriers. Moreover, the primary focus of this thesis centers on very narrow OEOs, and such, we do not make a distinction between the two families. We employ the same framework for analyzing the dynamics of OEOs and simply refer to both groups collectively as OEOs without classification.

Chapter 2 delves into a comprehensive exploration of a fundamental architecture of OEOs, featuring a single closed-loop configuration, composed of key components for basic OEO formation. These components include a laser, a polarization controller (PC), a Mach-Zehnder modulator (MZM), a fiber delay line (FDL), a photodetector (PD), a BPF, an RF amplifier (RFA), and an electric coupler. In the setup, the PD converts optical signals into RF signals, while the MZM performs electric to optic conversion by modulating the optical carrier sourced from the laser with an RF signal to close the loop. The RF signal, which feeds the modulator, is typically defined as the output signal of the oscillator. To analyze the dynamics of OEOs, a key approach is deriving envelope equations, which elucidates the dynamics of the output signal envelopes [32–34]. These equations encapsulate information about the phases and amplitudes of the output signals.

Despite the impressive phase noise performance of the basic setup outlined in Chapter 2 [35–40], one limitation of the setup can be challenges of achieving high microwave frequencies, particularly accessing the millimeter-wave range. This difficulty arises because the oscillation frequency is determined by the BPF, which implies that to generate higher frequencies, a corresponding filter is necessitated. However, this approach becomes impractical when considering the cost of BPFs in the millimeter-wave regime and the significant degradation in performance of electronic components with increased frequency range. To relieve this concern, a frequently employed method is frequency multiplication, a widely employed technique for easily accessing the millimeter-wave frequency range [41–51].

Chapter 3 investigates the dynamics of four frequency-multiplicative OEOs, as developed in the works referenced [47–50]. These OEOs employ multipath structures to tune the oscillation frequencies in their closed-loops while generating harmonics of the oscillation frequencies at separate output ports by controlling the states of polarization or phases of optical fields. Consequently, they mitigate the reliance on electronic components while offering access to significantly higher frequencies. However, although the frequency-multiplicative models can address the concerns proposed for the fundamental OEO, a critical drawback is that since the filtering still occurs in the RF domain, the resulting oscillators are generally not tunable in frequency. Additionally, narrowband RF filtering in the millimeter-wave range becomes progressively less effective as the frequency increases. These challenges can potentially be addressed by employing different frequency selection techniques, such as utilizing microwave photonic filters (MPFs) for frequency selections within optical domains.

Chapter 4 introduces a great example of it, OEOs based on stimulated Brillouin scattering (SBS). Using Brillouin scattering to enhance the functionalities of OEOs is a widespread strategy that has been implemented in various platforms [52–55]. In the configuration, a pump laser is injected into a highly nonlinear fiber spool to generate a Brillouin gain profile at an adjacent redshifted frequency. The process facilitates the selective amplification of a phase-modulated and contra-propagating laser signal. Notably, the RF oscillation frequency is solely determined by the spectral gap between the pump and signal lasers, rendering it is easily tunable. From that regard, a main characteristic of this approach is that frequency selection is achieved by the means of a MPF instead of an RF filter [56–58]. Several research groups have demonstrated that these SBS-based OEOs offer frequency tunability from DC to over 60 GHz and boast an ultra-low phase noise figure [59–61]. Remarkably, the km-long fiber spool can potentially be replaced by a sub-cm-long highly nonlinear waveguide, thereby providing the way for a chip-scale implementation [62].

Throughout Chapters 2, 3, and 4, we explore the dynamics of the various OEOs by deriving their respective microwave envelope equations. Comparing these envelope equations across different models reveal similarities between the dynamic equations, suggesting that their dynamics can be governed by an envelope equation that can be reformulated under a generalized universal form [63]. In Chapter 5, we introduce this universal equation, termed the universal microwave envelope equation, and conduct thorough analytical investigations. Additionally, we undertake stability analysis of the universal equation and suggest models that can be used to find solutions and evaluate their stabilities.

While the deterministic universal envelope equation offers a comprehensive tool for simultaneous exploration of various OEO dynamics, it falls short in describing the stochastic phase dynamics. Our focus shifts to investigating phase dynamics through the implementation of a stochastic approach, enabling us to optimize and comprehend phase noise performance effectively. In Chapter 6, we transform the deterministic universal envelope equation into a stochastic delay differential equation (SDDE), effectively describing the phase dynamics. In our analysis of the oscillators, we categorize noise sources into two types: additive noise contribution, due to random environmental and internal fluctuations, and multiplicative noise contribution, arising from noisy loop gains. The existence of the additive noise is independent of oscillation existence, while the multiplicative noise is intertwined with the noisy loop gains, nonlinearly mixing with signals above the threshold [35,64–66]. Therefore, we investigate both sub- and above-threshold regimes separately, where the multiplicative noise can be characterized as white and colored noise in respective regimes. For the above-threshold regime in Chapter 6, we proceed our analysis by characterizing the multiplicative noise as flicker and derive an equation for describing phase noise spectra. We validate the theoretical studies by the experimental results.

We perform the sub-threshold regime analysis in Chapter 7. We introduce frameworks to experimentally quantify the noise contributions discussed in the above-threshold part. Since no signal is present here and the oscillator is solely driven by stochastic noise, it becomes feasible to reverse-engineer the noise powers using a Fourier transform formalism. Here, we introduce a stochastic expression written in terms of the real-valued RF signals, because we do not need to express as complex envelops because there is no oscillation, no time-scale issue. However, both approaches are rooted from the same equation, so there is no dynamical difference between them, but only expression difference is there. The stochastic transformation facilitates the expressions of additive and multiplicative noise contributions as functions of noisy RF output powers. The additive noise can be defined by deactivating the laser source or biasing the intensity modulator at the minimum transmission point, given its independence from loop gains. The expression for the multiplicative noise indicates a dependence on gain, but experimental observations suggest that its magnitude may remain relatively constant beyond the threshold.

In Chapter 8, we conclude this work by summarizing the results presented in the previous sections.

Chapter 2: Optoelectronic Oscillators (OEOs)

2.1 Introduction of the Chapter

OEOs are nonlinear, self-sustained, and time-delayed microwave photonic systems capable of generating ultrapure microwave [1–4]. It arises from their hybrid structure, which comprise half-optical and half-electronic paths. Among many advantages from the optical path, the most significant conceptual breakthrough of these oscillators compared to fully electronic oscillators can be unprecedented high Q-factors achieved through storing optical energies for RF signal generation [5–7]. OEOs have been developed in various configurations to serve different purposes, and they can generally be categorized into two groups: broadband and narrowband families, based on their spectral bandwidth.

As the name implies, the broad OEOs make the best use of their wide bandwidths, which are achieved through high operating frequencies. An illustrative example within the broadband family is chaos cryptography, wherein an audio signal is encrypted within a high dimensional chaotic fluctuations of the wavelength, enabling high-speed encrypted communication [8–10]. Moreover, broadband OEOs find applications in machine learning. The infinite dimensionality resulting from time-delay and broad bandwidth facilitates their use in reservoir computing, an information processing technique that projects input data into a high-dimensional space for computation [11–14]. In addition, their wide bandwidth is advantageous in radar communications, random bit generation, parametric oscillator, clock recovery, and frequency comb generation [15–20].

In the realm of the narrowband family, the OEOs primarily focus on generation of RF signals with exceptionally high purity. Consequently, the design of narrowband OEOs emphasizes achieving a high Q-factor and minimizing phase noise. In a single closed-loop system, the Q-factor approximately follows $Q \sim f_0 T$, where f_0 represents the oscillation frequency and T denotes the time-delay in the optical path, typically equivalent to the delay induced by the fiber spool. For instance, a 4.4 km FDL introduce roughly a 22 μs delay ($T = n_g L / c_0$, where c_0 is the speed of light, L signifies the length of the fiber, and the group refractive index of silica is approximately $n_g = 1.48$), and a 10.5 GHz oscillation achieves a Q-factor greater than 2×10^6.

The oscillation frequencies of OEOs are typically determined by the center frequency of a narrow BPF and the free spectral range (FSR) from the time-delay. Essentially, OEOs are multi-mode devices, with the mode spacing corresponding to the FSR, given by FSR $= c_0/(n_g L)$. For a FDL spanning a few km, the FSR is measured in kHz. Ideally, the oscillation frequency of the system is selected as an integer multiple of the FSR, following the equation $f_0 = n \times$FSR where n can be any integer that brings the multiplication close to the center frequency of the filter.

The process of selecting oscillation frequencies of a fundamental OEO setup is depicted in Fig. 2.1. In the figure, (a) and (b) plots are obtained immediately after the pump while the bottom (c) plot corresponds to operation below the threshold. The center frequency of the filter employed is 10.5 GHz with a bandwidth of 21 MHz. A 4.4 km silica fiber spool is used where the length and the material introduce roughly a time delay of 22 μs. Each horizontal division on the plots represents a 50 kHz gap, with all three plots obtained within the range of 10.5048 GHz and 10.5051 GHz. Given the fiber spool, the theoretical FSR is expected to be approximately 45 kHz, which aligns with the observed distance. Comparing plots (a) and (b) reveals that every pump can have slightly different oscillation frequencies. Once the system is pumped, the oscillation frequency remains stable regardless of whether the gain is increased or decreased above the threshold regime. However, if the gain decreases below the threshold and the system is repumped, it may exhibit a different oscillation frequency.

A larger delay can give a higher Q, but it also results in a denser FSR, hampering a single-mode selection. To suppress unwanted modes, these systems employ extremely narrow BPFs. Typically, a filter is deemed narrow when its Q-factor (distinct from the Q-factor of OEOs) is greater than 1/2, but in OEO research, a Q-factor greater than 100 is generally expected to classify a filter as narrow. However, regardless of using very narrow filters, it is still difficult to suppress the unwanted modes. For example, the filter used in Fig. 2.1 has a 10.5 GHz oscillation frequency with a linewidth of 21 MHz, resulting in a Q-factor of 500, and it is very narrow. Nevertheless, despite the narrow linewidth, employing a 4.4 km fiber spool, resulting in FSR= 45 kHz, can yield more than 450 modes within the passband.

To address the proposed issues, various novel approaches have been proposed. One notable solution involves a dual-loop structure, connecting two fiber spools in different lengths in parallel. It capitalizes on the higher Q-factor provided by the longer fiber spool, while the shorter fiber mitigates the FSR through Vernier effect [21–23]. Another popular active strategy involves replacing the long FDLs by resonators, and this approach not only leads to a larger FSR but also maintains a high Q-factor through achieving a long photon lifetime [24–26]. Additionally, replacing a bulky fiber spool into a resonator allows to design an OEO in a small form factor. Also, the concept of parity-time symmetric OEO demonstrates a significant promise to ensure a single-mode oscillation by constructing two loops, which are one for gain and the other for loss where they have the equal magnitude [27–29].

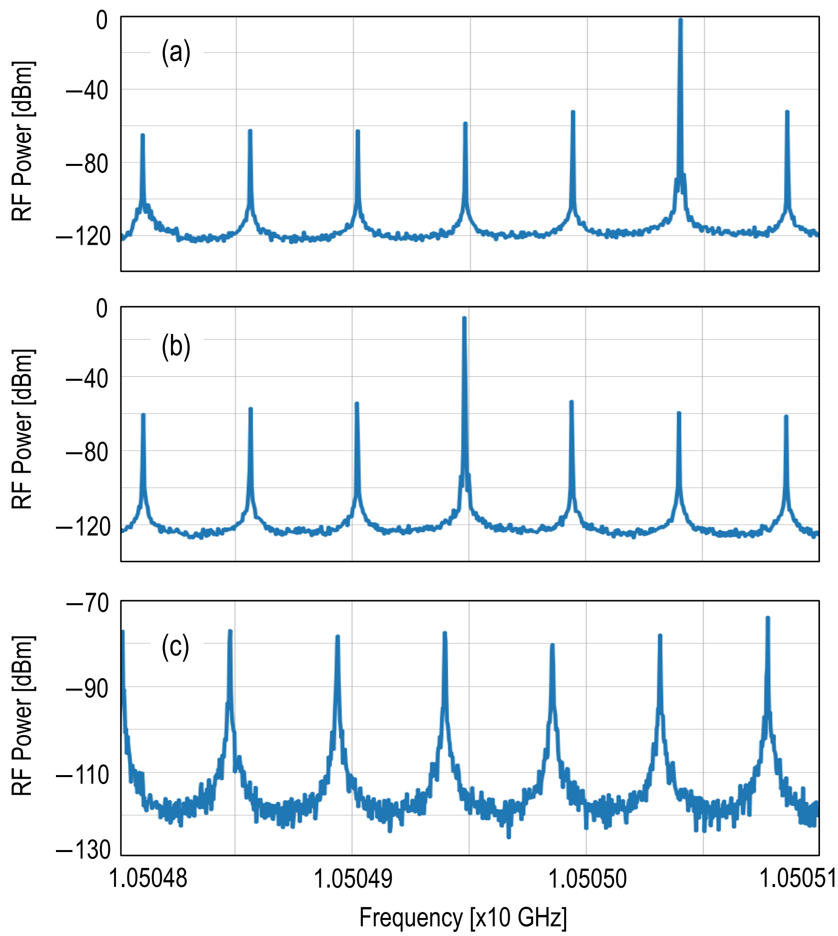

Figure 2.1: The process of selecting oscillation frequencies of a fundamental OEO setup where (a) and (b) plots are obtained immediately after the pump while the bottom (c) plot corresponds to operation below the threshold. The center frequency of the filter employed is 10.5 GHz with a bandwidth of 21 MHz. A 4.4 km silica fiber spool is used where the length and the material introduce roughly a time delay of 22 μs. Each horizontal division on the plots represents a 50 kHz gap, with all three plots obtained within the range of 10.5048 GHz and 10.5051 GHz. Given the fiber spool, the theoretical FSR is expected to be approximately 45 kHz, which aligns with the observed distance. Comparing plots (a) and (b) reveals that every pump can have slightly different oscillation frequencies where (a) presents 10.504950 GHz and (b) displays 10.505040 GHz as their oscillation frequencies, where the gap corresponds to 2×FSR.

Depending on their applications, OEOs have been classified into two families. However, they can still be studied within the same framework if they possess a reasonable level of Q-factor with a limited passband. There are some exceptional cases that necessitate slightly different approaches, such as those having very broad RF passband from very wide filters, employing only low-pass filtering, or even not using any filtering [30, 31]. However, in most OEOs, although the broad family utilizes a broad bandwidth, it defines this broad *relatively* in comparison to the narrow OEOs, and the broad families still have limited passbands relative to their carriers. Furthermore, the primary focus of the thesis is on very narrow OEOs, thus disregarding unusual cases. Consequently, we do not distinguish between the two families when studying the dynamics of OEOs and simply refer to both as OEOs without classification.

To grasp the dynamics of OEOs, this chapter presents and deeply examines a basic architecture of OEOs comprising a single closed-loop configuration, composed of key components for basic OEO formation. These components include a laser, a MZM, a FDL, a PD, a BPF, a RFA, and an electric coupler. The PD converts an optical signal into an RF signal, while the MZM performs electric to optic conversion by modulating the optical carrier sourced from the laser with an RF signal to close the loop. The RF signal, feeding the main modulator, is typically defined as the output signal of the oscillators. Depending on respective purposes of designing OEOs, the setups may include additional components, and their configurations and dynamics can become more intricate, as elaborated in Chapter 3 and 4. However, this chapter concentrates on presenting the basic setup.

To analyze the dynamics of OEOs, a key approach is to derive the envelope equations, which describes the dynamics of the output signal envelopes [32–34]. These equations encapsulate information about the phases and amplitudes of the output signals. In most OEO studies, the oscillation frequencies are known conditions, and the focus lies on comprehending the dynamics of the amplitudes and phases of RF output signals. The envelope equations serve as the primary tools for studying OEOs in the thesis, and this chapter presents a detailed derivation process of the envelope equation of the basic OEO setup in Sections 2.2 and 2.3. Additionally, the dynamics of the envelope equation is thoroughly explored. In Section 2.4, we find stationary state solutions and judge their stabilities. In addition, we verify the theoretical analysis by presenting numerical simulation results. Section 2.5 summarizes this chapter. Whenever we explore new setups in the thesis, we follow a similar process, as discussed in this chapter. Thus, this chapter holds significant importance.

2.2 System Setup

The most basic configuration of OEOs corresponds to Fig. 2.2 constituted of a continuous wave laser having an optical carrier ω_c and power P_0 and an oscillation loop which contains the following key elements: *(i)* a PC that controls polarization of the optical carrier; *(ii)* a MZM characterized by the RF half-wave voltage $V_{\pi_{\rm RF}}$ and DC half-wave voltage $V_{\pi_{\rm DC}}$ where a half-wave voltage is required amount of voltage to impose π phase shift; *(iii)* a FDL that causes a significant time-delay $T = L/v_g = n_0 L/c_0$ where again, v_g is the group velocity in the delay line, L is its length, and c_0 is the speed of light; *(iv)* a polarization insensitive PD that performs a fast direct detection characterized by the responsivity S in units of V/W; *(v)* a BPF of 3-dB bandwidth $\Delta\Omega$ around the center frequency Ω_0; *(vi)* a RFA with gain G; *(vii)* we also define the overall attenuation of a loop as κ which includes all loop losses. It should be noted that these parameters will also be considered in the rest of the proposal.

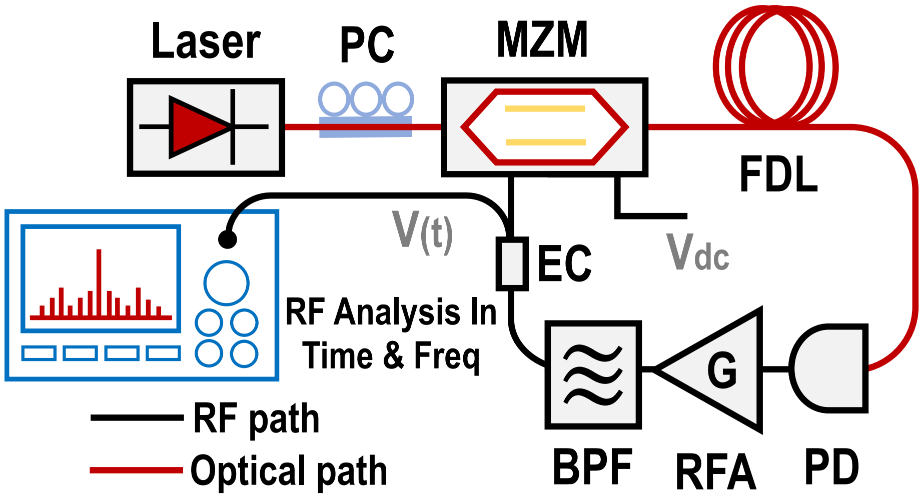

Figure 2.2: The schematic representation of the basic architecture of OEOs that consists of a continuous-wave laser, a polarization controller (PC), a Mach-Zehnder modulator (MZM), a fiber delay line (FDL), a photodetector (PD), a bandpass filter (BPF), a radiofrequency amplifier (RFA), and an electric coupler (EC). The laser pumps the OEO, and the signal is modulated by an RF signal, which also serves as the output signal of the OEO. After experiencing the time-delay at the FDL, the modulated signal is transformed back into an RF signal. Then, the RF signal undergoes amplification, bandpass filtering, and is looped back to the modulator, thereby closing the loop.

The laser pumps the OEO, and the signal is modulated by an RF signal, which also serves as the output signal of the OEO. After experiencing the time-delay at the fiber spool, the modulated signal is transformed back into an RF signal. Then, the RF signal undergoes amplification, bandpass filtering, and is looped back to the modulator, thereby closing the loop. The actual experimental setup is shown in Fig. 2.3. When we should run the setup for a long time, the modulator bias controller can be inserted in the loop to automatically control the transmission point. In addition, the erbium-doped fiber amplifier can be used to provide more optical power for increasing the loop gain.

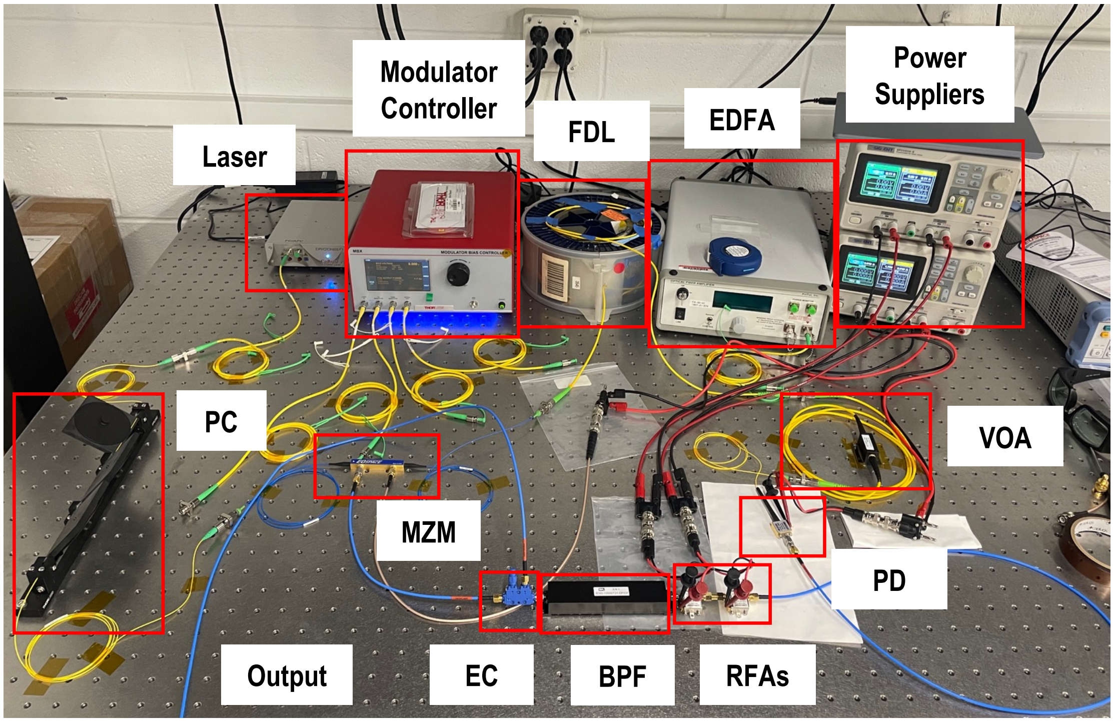

Figure 2.3: The picture describes the experimental setup of Fig. 2.2. The setup consists of a continuous-wave laser, a polarization controller (PC), a Mach-Zehnder modulator (MZM), a fiber delay line (FDL), a variable optical attenuator (VOA), a photodetector (PD), a bandpass filter (BPF), two radiofrequency amplifiers (RFAs), and an electric coupler (EC). The VOA is inserted to control the overall loop gain while we fix the power of the laser. The power suppliers are to provide powers for the two RFAs and the PD, and control the transmission point of the modulator. A modulator controller and an erbium-doped fiber amplifier (EDFA) are shown, where they can be also included in the loop to control the DC bias point automatically for a long running and overall loop gain.

2.3 System Modeling

Because of the hybrid structure, the oscillator has the capability to simultaneously produce signals in both the electrical and optical spectral ranges. Our research focus is on microwave generation, and we designate the output signal as

$$V(t) = |\mathcal{V}(t)| \cos[\Omega_0 t + \psi(t)] \tag{2.1}$$

where $\mathcal{V}(t)$ represents the complex amplitude of the signal. As mentioned previously, we are interested in the dynamics of the amplitude and phase rather than the oscillation frequency, which remains a known and constant condition in most OEO studies.

The purpose of the PC is to align the axes of the laser and MZM, thereby maximizing the output power of the modulator. The carrier is modulated by $V(t)$ in Eq. (2.1) at the MZM and the resulting output field envelope can be described as

$$\mathcal{E}(t) = \sqrt{P_0} \cos \left\{ \frac{\pi V(t)}{2V_{\pi\mathrm{RF}}} + \frac{\pi V_{\mathrm{B}}}{2V_{\pi\mathrm{DC}}} \right\} \tag{2.2}$$

which is in units of $\mathrm{W}^{\frac{1}{2}}$.

2.3.1 Dynamics at Bandpass Filters

The dynamics of RF BPFs can be taken into account for deriving the dynamic equation of the system, as the oscillation frequency is determined by the filters. If we define $V_{\mathrm{in}}(t)$ and $V_{\mathrm{out}}(t)$ as the input and output of the BPF respectively, the dynamics of the RLC filters can be expressed as follows:

$$\hat{\mathsf{H}}[V_{\mathrm{out}}(t)] \equiv V_{\mathrm{out}}(t) + \frac{1}{\Delta\Omega} \frac{dV_{\mathrm{out}}(t)}{dt} + \frac{\Omega_0^2}{\Delta\Omega} \int_{t_0}^{t} V_{\mathrm{out}}(s) ds = V_{\mathrm{in}}(t) \tag{2.3}$$

$\hat{\mathsf{H}}$ is called the integro-differential operator of narrow filters. To utilize the provided equation, we need to define the input and output signals. As depicted in Fig. 2.2, $V_{\mathrm{out}}(t)$ is already represented as $V(t)$, as given in Eq. (2.1). Therefore, our next step is to express the output of the amplifier in terms of $V(t)$.

After the modulated field experiences the time-delay T, the signal reaches the input of the detector and its power can be expressed using the square-law as follows: $P(t) = |\mathcal{E}(t)|^2$, corresponding to

$$P(t) = P_0 \cos^2 \left\{ \frac{\pi V(t-T)}{2V_{\pi \mathrm{RF}}} + \frac{\pi V_{\mathrm{B}}}{2V_{\pi \mathrm{DC}}} \right\}. \tag{2.4}$$

Given the conversion gain S, the cumulative loss κ, including the loss of every electronic, optic, and opto-electronic devices, and the gain of the amplifier G, the input voltage of the BPF can be defined as $V_{\mathrm{in}}(t) = \kappa GSP(t)$, and we can rewrite Eq. (2.3) as

$$V(t) + \frac{1}{\Delta\Omega}\frac{dV(t)}{dt} + \frac{\Omega_0^2}{\Delta\Omega}\int_{t_0}^{t} V(s)ds = \kappa SGP_0 \cos^2 \left\{ \frac{\pi V(t-T)}{2V_{\pi \mathrm{RF}}} + \frac{\pi V_{\mathrm{B}}}{2V_{\pi \mathrm{DC}}} \right\}. \tag{2.5}$$

To simplify, we normalize the output signal as a dimensionless voltage $x(t) = \pi V(t)/(2V_{\pi \mathrm{RF}})$. Then, Eq. (2.5) can be rewritten as

$$x(t) + \frac{1}{\Delta\Omega}\frac{dx(t)}{dt} + \frac{\Omega_0^2}{\Delta\Omega}\int_{t_0}^{t} x(s)ds = \beta \cos^2[x_T + \phi]. \tag{2.6}$$

where the subscript of T denotes the time-delayed function, equivalent to $x_T \equiv x(t-T)$. The normalized feedback gain parameter is defined by

$$\beta = \frac{\pi \kappa GSP_0}{2V_{\pi \mathrm{RF}}}, \tag{2.7}$$

and the offset phase corresponds to

$$\phi = \frac{\pi V_{\mathrm{B}}}{2V_{\pi\mathrm{DC}}}. \tag{2.8}$$

The feedback gain serves as the bifurcation parameter of the system, which can be finely controlled by the optical power in a closed-loop state or using an optical attenuator, as will be discussed in a later chapter.

To comprehend the transmission points of MZMs and the significance of the offset phase, it is beneficial to introduce Jacobi-Anger expansion, given by:

$$e^{i[z\cos(\alpha)+\eta]} = \sum_{n=-\infty}^{\infty} i^n \mathrm{J}_n(z) e^{i(n\alpha+\eta)} \tag{2.9}$$

where $\mathrm{J}_n(z)$ is the n-th order Bessel function of the first kind and the argument must be positive. Using a trigonometry identity, it can also be written in a sinusoidal waveform, given by:

$$\cos\Big[z\cos(\alpha)+\eta\Big] = \cos(\eta)\mathrm{J}_0(z) + 2\sum_{n=1}^{\infty} \epsilon_n(\eta)\mathrm{J}_n(z)\cos(n\alpha) \tag{2.10}$$

where the epsilon function obeys

$$\epsilon_n(\eta) = \frac{1}{2}[e^{i\eta} + (-1)^n e^{-i\eta}]i^n = \begin{cases} (-1)^{\frac{n}{2}}\cos(\eta), & \text{if } n \text{ is even} \\ (-1)^{\frac{n+1}{2}}\sin(\eta), & \text{if } n \text{ is odd.} \end{cases} \tag{2.11}$$

Modulators are most commonly biased at three specific points: *(i)* Quadrature transmission point (QTP) that generates both the odd and even-ordered modes biased at $\eta = \pi/4$; *(ii)* Maximum

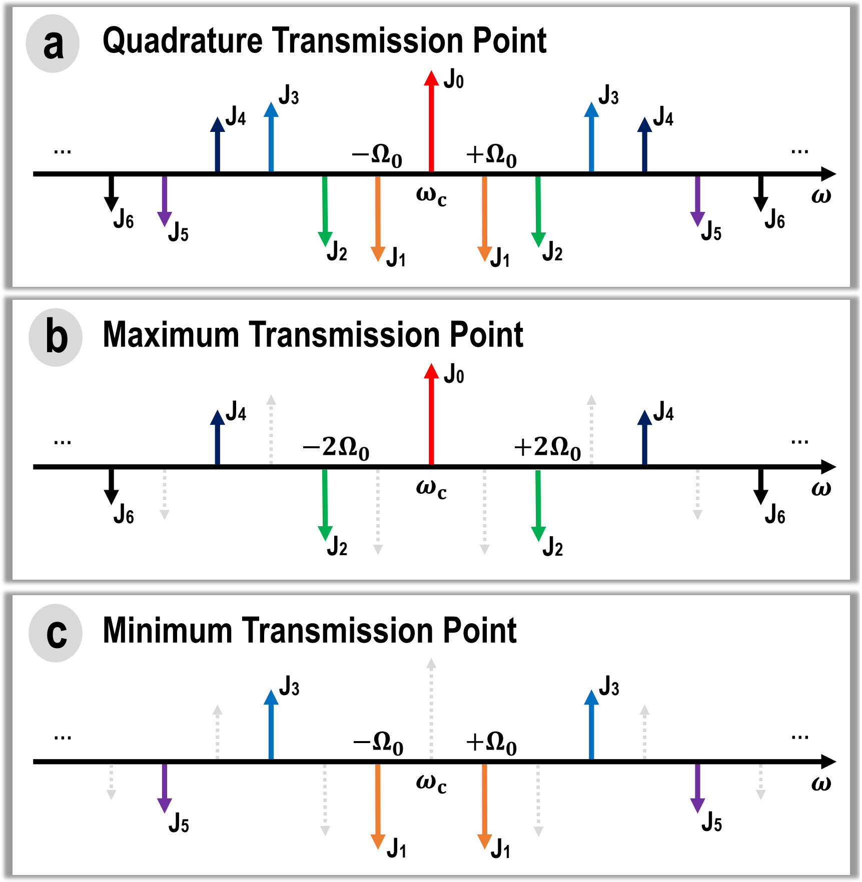

Figure 2.4: Transmission point representation in the frequency domain. J_n denotes n-th order Bessel function of the first kind. The quadrature transmission point (QTP) generates both the odd and even-ordered modes while the maximum transmission point (MATP) and minimum transmission point (MITP) generate only the even and odd-ordered modes respectively. The distance between adjacent modes of the QTP is Ω_0 while the intermodal distance in the MATP and the MITP is $2\Omega_0$. The modes of same color have the same amplitudes and the same distance from the optical carrier ω_c.

transmission point (MATP) that generates only even-ordered frequencies biased at $\eta = 0$ or π; *(iii)* Minimum transmission point (MITP) that generates only odd-ordered frequencies biased at $\eta = \pi/2$ or $3\pi/2$. Therefore, the transmission point not only controls the transmission efficiency of the power but also gets involved with frequency generation at PDs, a key concept of frequency-multiplication. The graphical expressions of the transmission points are shown in Fig. 2.4.

2.3.2 Derivation of Envelope Equation

Continuing research under the form of Eq. (2.6) poses a challenge due to substantial time-scale differences between the fastest and slowest terms, namely the integration and time-delayed terms inside the cosine function. The scale difference is due to the large time-delay and fast oscillation where the oscillation frequency is a known condition for OEO research while the time-delay is a key that should be considered. In order to overcome this challenge, we derive a new expression for $x(t)$. When the BPF is narrow enough to reject the subsequent harmonics of Ω_0, it is possible to write $x(t)$ in terms of its complex slowly-varying envelope, as follows:

$$x(t) = \frac{1}{2}\mathcal{A}(t)e^{i\Omega_0 t} + \frac{1}{2}\mathcal{A}^*(t)e^{-i\Omega_0 t}, \tag{2.12}$$

where we can write the following property due to its slowly-varying property: $|\dot{\mathcal{A}}(t)| \ll \Omega_0|\mathcal{A}(t)|$. Moreover, comparing the expressions of Eqs. (2.1) and (2.12), we can represent $\mathcal{A}(t)$ in phasor notation as $\mathcal{A}(t) = |\mathcal{A}(t)|e^{i\psi(t)}$ and $x(t)$ in a sinusoidal form as $x(t) = |\mathcal{A}(t)|\cos[\Omega_0 t + \psi(t)]$.

Using Jacobi-Anger expansion provided in Eqs. (2.9), (2.10), and (2.11), we can first incorporate the envelope expression into the right-hand side of Eq. (2.6), yielding

$$x(t) + \frac{1}{\Delta\Omega}\frac{dx(t)}{dt} + \frac{\Omega_0^2}{\Delta\Omega}\int_{t_0}^{t} x(s)ds = -\gamma \mathrm{J}_1[2|\mathcal{A}_T|]\cos[\Omega_0(t-T) + \psi_T]. \tag{2.13}$$

where the DC and generated harmonic terms on the right-hand side are not considered by considering filtering, and we define the effective loop gain as

$$\gamma = \beta \sin 2\phi. \tag{2.14}$$

The given expression represents that the RF signal is maximized at the QTP, $\phi = \pi/4$, and thus, we usually operate the modulator at the QTP for signal generation.

In order to circumvent the difficulty of dealing with an integral term, we introduce a variable $u(t) = \int_{t_0}^{t} x(s)ds$. The variable can also be represented in terms of its complex slowly varying envelope. If we denote the envelope as $\mathcal{B}(t)$, the integration term can be written as

$$u(t) = \frac{1}{2}\mathcal{B}(t)e^{i\Omega_0 t} + \frac{1}{2}\mathcal{B}^*(t)e^{-i\Omega_0 t}. \tag{2.15}$$

Using the defined envelope expressions, given in Eqs. (2.12) and (2.15), the filter equation can be re-expressed as

$$\begin{aligned}\frac{1}{2}\mathcal{A}(t)e^{i\Omega_0 t} + \frac{1}{2\Delta\Omega}[\dot{\mathcal{A}}(t) + i\Omega_0\mathcal{A}(t)]e^{i\Omega_0 t} + \frac{\Omega_0^2}{2\Delta\Omega}\mathcal{B}(t)e^{i\Omega_0 t} + \mathcal{C}.\mathcal{C}. =\\ -\frac{\gamma}{2}\mathrm{J}_1[2|\mathcal{A}_T|]e^{i\Omega_0(t-T)}e^{i\psi_T} + \mathcal{C}.\mathcal{C}.\end{aligned} \tag{2.16}$$

where the upperdot denotes the time-derivative of the envelope, and $\mathcal{C}.\mathcal{C}.$ signifies the complex conjugates of all preceding terms on the sides. In the subsequent step, we disregard the complex conjugate terms, since they yield the same equation, meaning Eq. (2.16) can be simplified into as a coupled equation, rendering it redundant.

Based on the definition of $\dot{u}(t) = x(t)$ with Eqs. (2.12) and (2.15), we can derive the relationship between the two complex envelopes, resulting in $\mathcal{A}(t) = \dot{\mathcal{B}}(t) + i\Omega_0\mathcal{B}(t)$. Through the expression, the left-hand side of Eq. (2.16) can be represented only in terms of $\mathcal{B}(t)$, as follows:

$$\dot{\mathcal{B}}(t) + i\Omega_0\mathcal{B}(t) + \frac{1}{\Delta\Omega}[\ddot{\mathcal{B}}(t) + 2i\Omega_0\dot{\mathcal{B}}(t)] = -2\gamma e^{-i\sigma}\mathrm{Jc}_1[2|\mathcal{A}_T|]\mathcal{A}_T \tag{2.17}$$

where we define the detuning factor $\sigma = \Omega_0 T$ and Bessel-Cardinal function $\mathrm{Jc}_1(x) = \mathrm{J}_1(x)/x$, qualitatively displays a similar behavior as the sine-cardinal (sinc) function. Since $\mathcal{B}(t)$ is also slowly-varying as $\mathcal{A}(t)$ does, the envelope should satisfy the following condition: $\ddot{\mathcal{B}}(t) \ll \Omega_0\dot{\mathcal{B}}(t) \ll \Omega_0^2\dot{\mathcal{B}}(t)$. The property indeed simplifies Eq. (2.17) as

$$i\Omega_0\mathcal{B}(t) + i\frac{2}{\Delta\Omega}\Omega_0\dot{\mathcal{B}}(t) = -2\gamma e^{-i\sigma}\mathrm{Jc}_1[2|\mathcal{A}_T|]\mathcal{A}_T \tag{2.18}$$

In addition, under the slowly-varying condition, the relationship between the two envelopes can be further simplified as $\mathcal{A}(t) = \dot{\mathcal{B}}(t) + i\Omega_0\mathcal{B}(t) \simeq i\Omega_0\mathcal{B}(t)$. Finally, we can express Eq. (2.18) solely in terms of $\mathcal{A}(t)$, yielding our final envelope equation as

$$\dot{\mathcal{A}} = -\mu e^{i\vartheta}\mathcal{A} - 2\mu\gamma e^{i\vartheta}e^{-i\sigma}\mathrm{Jc}_1[2|\mathcal{A}_T|]\mathcal{A}_T \tag{2.19}$$

where we omit the time-domain expression for the envelope, $\mathcal{A}(t) \to \mathcal{A}$ for simplicity. It is worth noting that we consistently use the simplified envelope notation throughout the entire thesis. We also define the half-bandwidth as

$$\mu = \frac{\Delta\Omega/2}{\sqrt{1+[1/(2Q_{\mathrm{rf}})]^2}} \text{ and } \vartheta = \arctan\left[\frac{1}{2Q_{\mathrm{rf}}}\right]. \tag{2.20}$$

In general, the RF Q-factor, $Q_{\mathrm{rf}} = \Omega_0/\Delta\Omega$, is high enough to approximate $\mu \simeq \Delta\Omega/2$ and $\vartheta \simeq 1/(2Q_{\mathrm{rf}})$.

2.4 Stationary States and Their Stability

2.4.1 Stationary State Solutions

In this section, we explore the nonlinear dynamics of the envelope equation Eq. (2.19). We first identify the stationary state solutions, also known as the fixed points, of the system and evaluate their stabilities. Here, we make the approximation $\vartheta \simeq 0$ considering this parameter to be small due to its inverse relation with Q_{rf} as mathematically described in Eq. (2.20) although the parameter should not be disregarded to explore the phase dynamics in Chapter 6. To find the stationary state solutions, we apply that there is no time-variance and rewrite Eq. (2.19) as

$$\mathcal{A}_{\mathrm{st}} + 2e^{-i\sigma}\gamma \mathrm{Jc}_1[2|\mathcal{A}_{\mathrm{st}}|]\mathcal{A}_{\mathrm{st}} = 0 \tag{2.21}$$

where $\mathcal{A}_{\mathrm{st}}$ denotes the complex-valued stationary envelope solutions. Here, due to a phase matching condition on both sides, it becomes possible to determine the detuning factor as $e^{-i\sigma} = \pm 1$. Since the system should have a proper pumping for oscillation, we should select a solution set from the following two options: $\sigma = \pi \mathrm{mod}[2\pi]$ and $\gamma > 0$, or $\sigma = 2\pi \mathrm{mod}[2\pi]$ and $\gamma < 0$.

As γ represents the loop gain, we opt for $\sigma = \pi \text{mod}[2\pi]$ and $\gamma > 0$, indicating that we need $\phi = \pi/4$ as β is a positive value.

By plugging the solution set into Eq. (2.19), we can employ another phase matching condition $\psi(t) = \psi(t-T)$ and it leads to extract the dynamics of the magnitude $|\mathcal{A}|$, as follows

$$\dot{A} = -\mu A + 2\mu\gamma \text{Jc}_1[2A_T]A_T \tag{2.22}$$

where we do calligraphic font out, $|\mathcal{A}| \to A$, for the real-valued variable. The expression enables us to focus solely on investigating the dynamics of the magnitude, and we opt for this approach as the investigation of the phase dynamics will be addressed differently in Chapter 6. Moreover, in the stationary state analysis, the phase term can be eliminated since both phase and magnitude are time-invariant. Now, Eq. (2.21) can be rewritten as

$$A_{\text{st}} = 2\gamma \text{Jc}_1[2A_{\text{st}}]A_{\text{st}}, \tag{2.23}$$

which generates two types of solutions that can be respectively referred to as a trivial and an oscillatory solution, as follows

$$A_{\text{tr}} = 0 \tag{2.24}$$

$$A_{\text{osc}} = \frac{1}{2}\text{Jc}_1^{-1}\left[\frac{1}{2\gamma}\right] \simeq \sqrt{3}\left[1 - \frac{1}{\sqrt{3}}\sqrt{\frac{4}{\gamma} - 1}\right]^{1/2}. \tag{2.25}$$

The illustrated approximation for the oscillatory solution can be achieved through a fifth-order expansion within a specified range of $\gamma < 5$ [7]. Even though this approximation may limit the validity of the solution to cases where $\gamma < 5$, it is insignificant because attaining a gain greater than $\gamma = 5$ is extremely challenging when we consider maximum input powers of components and $V_{\pi\mathrm{rf}}$ values of modulators. Considering that the Bessel-Cardinal function approaches its maximum value of $1/2$ near zero, the oscillatory solution can be existed for $\gamma > 1$.

2.4.2 Stability of the Trivial Solution

In order to evaluate the stability of the trivial solution, we can consider small perturbation near the solution. We first can define the complex valued perturbation as

$$\delta\mathcal{A} = \delta\mathcal{A}_0 e^{(\lambda_{\mathrm{st}} + i\xi_{\mathrm{st}})t} \tag{2.26}$$

where $\delta\mathcal{A}_0$ denotes the magnitude, while λ_{tr} and ξ_{tr} signify the real and imaginary eigenvalues of a stationary state solution. In this context, we evaluate the stability of the trivial solution first by substituting $A_{\mathrm{st}} \to A_{\mathrm{tr}} + \delta\mathcal{A} = \delta\mathcal{A}$ into the dynamic equation Eq. (2.22), yielding the below expression:

$$\begin{aligned} \delta\dot{\mathcal{A}} &= -\mu\delta\mathcal{A} + 2\mu\gamma\mathrm{Jc}_1[2A_{\mathrm{tr}} + 2\delta\mathcal{A}_T]\delta\mathcal{A}_T \\ &\simeq -\mu\delta\mathcal{A} + \mu\gamma\delta\mathcal{A}_T \end{aligned} \tag{2.27}$$

where we apply a Taylor expansion to the Bessel-Cardinal function and consider only up to the first order, as $\delta\mathcal{A}_T$ and $\delta\mathcal{A}$ represent extremely small perturbations. Next, we substitute the eigenvalue expression defined in Eq. (2.26) into Eq. (2.27) to evaluate the stability. Subsequently, we can express the real and imaginary eigenvalues respectively as

$$\lambda_{\text{tr}} = -\mu + \mu\gamma e^{-\lambda_{\text{tr}}T}\cos\xi_{\text{tr}}T$$

$$\xi_{\text{tr}} = -\mu\gamma e^{-\lambda_{\text{tr}}T}\sin\xi_{\text{tr}}T. \tag{2.28}$$

To further simplify the above expression, we can consider the fact that a bifurcation occurs where the real part changes its sign. For the real part expression, we employ a Taylor expansion to the exponential term, yielding $e^{-\lambda_{\text{tr}}T} \simeq 1 - \lambda_{\text{tr}}T$. Regarding the imaginary part, we can simply assume $\lambda_{\text{tr}} = 0$, leading to further simplification of the coupled expressions as:

$$\lambda_{\text{tr}} = \frac{-\mu + \mu\gamma\cos\xi_{\text{tr}}T}{1 + \mu T\gamma\cos\xi_{\text{tr}}T} \tag{2.29}$$

$$\xi_{\text{tr}} = -\mu\gamma\sin\xi_{\text{tr}}T. \tag{2.30}$$

By considering the huge scale difference on both sides in Eq. (2.30) due to μ, we can first determine the two possible solutions for the imaginary part as 0 or π/T. From the imaginary part solutions, we could obtain the following two possible solution sets as:

$$\lambda_{\text{tr}} = \frac{\mu\gamma - \mu}{1 + \mu T\gamma} \simeq \frac{\gamma - 1}{T\gamma} \ \text{ if } \ \gamma > 0 \ \text{ and } \ \xi_{\text{tr}} = 0 \tag{2.31}$$

$$\lambda_{\text{tr}} = \frac{-\mu\gamma - \mu}{1 - \mu T\gamma} \simeq \frac{\gamma + 1}{T\gamma} \ \text{ if } \ \gamma < 0 \ \text{ and } \ \xi_{\text{tr}} = \frac{\pi}{T}. \tag{2.32}$$

In order to derive the two solutions, we utilize the important approximation $\mu T \gg 1$. This is a highly significant approximation in OEO research which originates from $T \gg 1/\mu$, implying that the delay is far greater than the filter response time. For the first solution set, the stability can be established if $\gamma < 1$, while the trivial solution becomes unstable elsewhere. Regarding the second solution, the solution is only achieved for $-1 < \gamma < 0$. However, since we have previously defined γ as a positive number during the phase matching for Eq. (2.21), this solution set is invalid. Therefore, we could summarize the result of the trivial solution analysis as follows: the trivial solution is stable for $\gamma < 1$.

2.4.3 Stability of the Oscillatory Solution

In order to evaluate the stability of the oscillatory solution, we follow a similar process as for the trivial solution. We examine small perturbations near the oscillatory solution and substitute $A_{\text{tr}} \to A_{\text{osc}} + \delta\mathcal{A}$ into Eq. (2.22), yielding the following equation:

$$\begin{aligned}
\delta\dot{\mathcal{A}} &= -\mu(A_{\text{osc}} + \delta\mathcal{A}) + 2\mu\gamma(A_{\text{osc}} + \delta\mathcal{A}_T)\Big\{\mathrm{Jc}_1[2A_{\text{osc}}] + 2\delta\mathcal{A}_T\mathrm{Jc}_1'[2A_{\text{osc}}]\Big\} \\
&= -\mu\delta\mathcal{A} + \mu\delta\mathcal{A}_T + 4\mu\gamma A_{\text{osc}}\mathrm{Jc}_1'[2A_{\text{osc}}]\delta\mathcal{A}_T \\
&= -\mu\delta\mathcal{A} - \mu\delta\mathcal{A}_T + 2\mu\gamma\mathrm{J}_0[2A_{\text{osc}}]\delta\mathcal{A}_T
\end{aligned} \tag{2.33}$$

where we have employed the identity related to the Bessel-Cardinal function identity, defined as:

$$\mathrm{Jc}_1'(x) = \frac{1}{x}\mathrm{J}_0(x) - \frac{2}{x}\mathrm{Jc}_1(x). \tag{2.34}$$

By plugging the eigenvalue expression, $\delta\mathcal{A} = \delta\mathcal{A}_0 e^{(\lambda_{\text{osc}}+i\xi_{\text{osc}})t}$, into Eq.(2.22), we could obtain the expressions for the real and imaginary parts as

$$\lambda_{\text{osc}} = \frac{-\mu + \mu\alpha\cos\xi_{\text{osc}}T}{1+\mu T\alpha\cos\xi_{\text{osc}}T} \tag{2.35}$$

$$\xi_{\text{osc}} = -\mu\alpha\sin\xi_{\text{osc}}T \tag{2.36}$$

where we define the alpha parameter as

$$\alpha = 2\gamma \mathrm{J}_0[2A_{\text{osc}}] - 1. \tag{2.37}$$

Due to a huge scale difference, the two possible solutions for the imaginary part can be $\xi_{\text{osc}} = 0$ and $\xi_{\text{osc}} = \pi/T$, and the following two possible solution sets can be written as

$$\lambda_{\text{osc}} = \frac{\mu\alpha-\mu}{1+\mu T\alpha} \simeq \frac{\alpha-1}{T} \;\text{ if }\; \alpha > 0 \;\text{ and }\; \xi_{\text{osc}} = 0 \tag{2.38}$$

$$\lambda_{\text{osc}} = \frac{-\mu\alpha-\mu}{1-\mu T\alpha} \simeq \frac{\alpha+1}{T\alpha} \;\text{ if }\; \alpha < 0 \;\text{ and }\; \xi_{\text{osc}} = \frac{\pi}{T}. \tag{2.39}$$

The first solution can achieve stability if $\alpha < 1$, and it corresponds to $\mathrm{J}_0[2A_{\text{osc}}] < 1/\gamma$ as indicated in Eq. (2.37). We can now utilize the approximated expression for the oscillatory solution, defined in Eq. (2.25), to express the range solely in terms of γ as:

$$\mathrm{J}_0\left[2\sqrt{3-\left(\frac{12}{\gamma}-3\right)^{1/2}}\right] < \frac{1}{\gamma}. \tag{2.40}$$

The above expression reveals that the solution is stable for $\gamma > 1$. On the other hand, the second solution, as indicated in Eq. (2.39), suggests stability for the oscillatory solution when $\gamma < 2.31$. Consequently, considering both solutions, we can conclude that the oscillatory solution is stable for $1 < \gamma < 2.31$.

From the stability analysis of the two solutions, it is evident that the trivial solution is stable for $\gamma < 1$, while the oscillatory solution is unstable in the range, indicating a lack of oscillations in the output of the system. However, once the gain exceeds unity, a Hopf bifurcation occurs, resulting in a switch in the stabilities of the two solutions. Therefore, the oscillatory solution becomes stable above the gain, leading us to designate this point as the threshold gain $\gamma_{\mathrm{th}} = 1$. However, if the gain surpasses $\gamma = 2.31$, the system experiences a secondary bifurcation, known as the secondary Hopf bifurcation or Neimark-Sacker bifurcation, where no solutions are stable in the regime. We term this point the critical gain $\gamma_{\mathrm{cr}} = 2.31$. In the next subsection, we validate these theoretical interpretations through numerical simulations.

2.4.4 Numerical Simulation

Numerical simulation results of Eq. (2.19) are depicted in Fig. 2.5. Based on these results, it is possible to validate the theoretical stability analysis conducted previously. A comparison between Fig. 2.5 (a) and (b) illustrates the dynamics before and after reaching the threshold gain. Below the threshold, the amplitude goes to zero as the trivial solution is stable in this region. By further increasing the gain beyond the threshold, the oscillatory solution becomes stable, as the system undergoes the Hopf bifurcation, leading to a switch in the stability of the solutions [67]. Comparing Fig. 2.5 (c) and (d) reveals that as the gain exceeds the critical value,

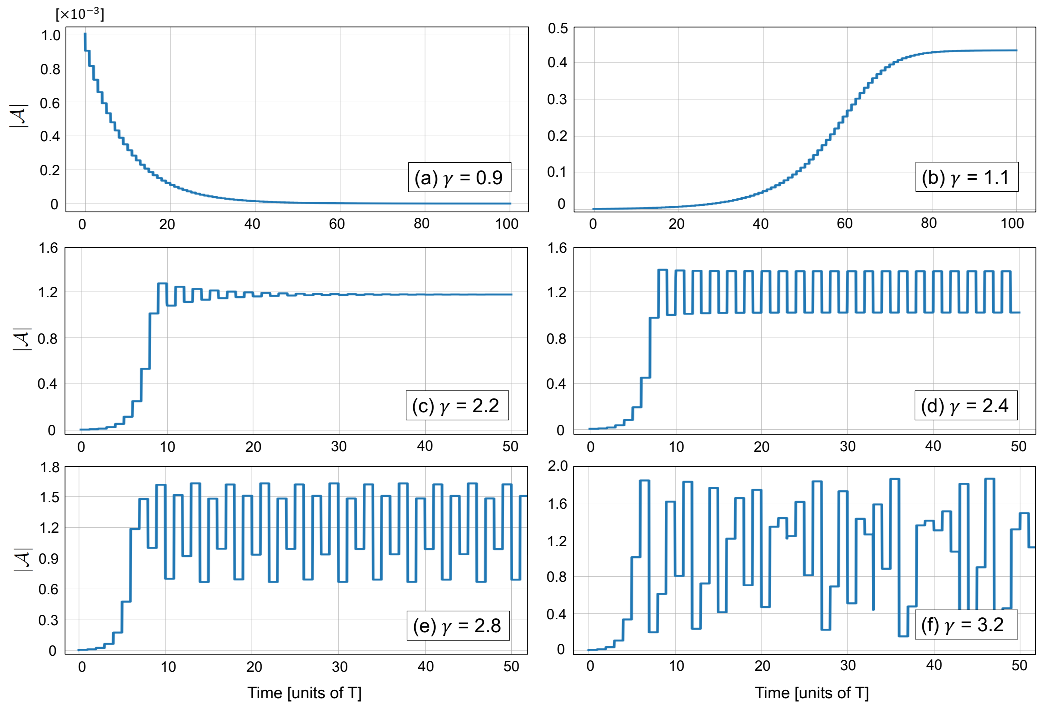

Figure 2.5: Numerical simulation of the envelope equation of the basic OEO, shown in Eq. (2.19), with parameters $\mu = 2\pi \times 25$ MHz, $T = 20$ μs, and an initial condition $\mathcal{A} = 0.001$ for $t \in [-T, 0]$. The gains at each specified point are (a) $\gamma = 0.9$, (b) $\gamma = 1.1$, (c) $\gamma = 2.2$, (d) $\gamma = 2.4$, (e) $\gamma = 2.8$, and (f) $\gamma = 3.2$. A comparison between (a) and (b) illustrates the dynamics before and after reaching the threshold gain. Below the threshold, the amplitude diminishes to zero as the trivial solution is stable in the region. By further increasing the gain beyond the threshold, the oscillatory solution becomes stable while the trivial solution becomes unstable. Comparing (c) and (d) reveals that as the gain exceeds the critical value, the oscillatory solution becomes unstable, leading to an amplitude modulation at the frequency $1/(2T)$. Further gain increase results in $4T$-periodic amplitude modulation, as shown in (e), eventually leading to chaotic behavior, as depicted in (f).

the oscillatory solution becomes unstable, resulting in an amplitude modulation at the frequency $1/(2T)$, referred to as $2T$-periodicity, due to the occurrence of the secondary Hopf bifurcation or Neimark-Sacker bifurcation. Further gain increase results in $4T$-periodic amplitude modulation, as shown in Fig. 2.5 (e), eventually leading to chaotic behavior, as depicted in Fig. 2.5 (f).

The bifurcation diagram of the aforementioned dynamics is presented in Fig. 2.6. In the region between the two specific gains, it is possible to observe that respective gains have certain oscillatory solutions, indicating clear oscillations. Conversely, as the gain becomes higher, each

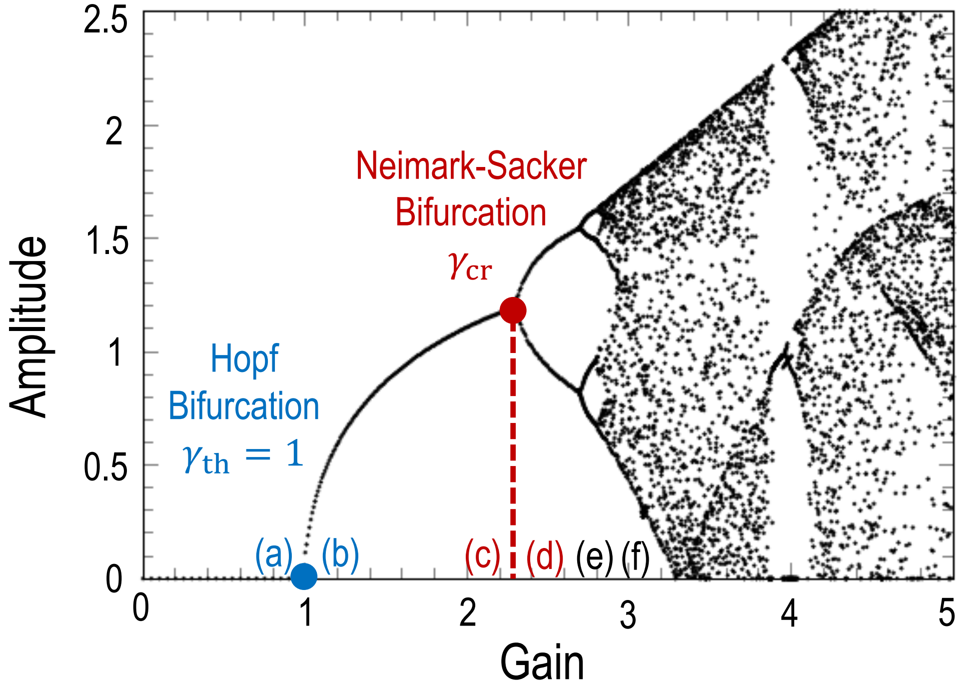

Figure 2.6: Bifurcation diagram plotted by numerical simulation of the envelope equation of the basic OEO, shown in (2.19), with parameters $\mu = 2\pi \times 25$ MHz, $T = 20$ μs, and an initial condition $\mathcal{A} = 0.001$ for $t \in [-T, 0]$. The gains at each expressed point are (a) $\gamma = 0.9$, (b) $\gamma = 1.1$, (c) $\gamma = 2.2$, (d) $\gamma = 2.4$, (e) $\gamma = 2.8$, and (f) $\gamma = 3.2$. The blue and red points represent where the Hopf and Neimark-Sacker bifurcation occur.

gain exhibits more than one solution, suggesting that the oscillation is no longer stable. Through these simulation results, it is possible to experimentally confirm the theoretical analysis presented in this section.

2.5 Conclusion of the Chapter

This chapter successfully derived the microwave envelope equation for the basic OEO, which describes the nonlinear dynamics of the system by delivering the phase and amplitude information of the output signal. The dynamics of the setup depends on the dynamics of the filter as the oscillation frequency is determined there. However, it was shown that in case of the time-delayed system, the filter equation has a timescale issue because of the significant disparity between the slowest and fastest dynamical timescales. In the situation, expressing the output signal in terms of its complex conjugate envelopes proves to be the most effective strategy. This approach nullifies the oscillation frequency terms and effectively resolves the timescale issue, offering a comprehensive solution to the problem at hand.

The analysis of the envelope equation reveals two distinct solutions: a trivial solution and an oscillatory solution, and their stabilities shift as the loop gain increases. Below the threshold gain, the trivial solution is stable, and no oscillations manifest. The first bifurcation, known as the Hopf bifurcation, occurs precisely at the threshold gain, leading to a switch in stability between the two solutions. In the interval from the threshold gain to the critical gain, the oscillatory solution remains stable, rendering this region optimal for pure microwave generation. The oscillatory solution is gain-dependent and each gain in the region has its unique oscillatory solution. Upon reaching the critical gain, the system undergoes the second bifurcation, referred to as the secondary Hopf bifurcation or the Neimark-Sacker bifurcation. Right after the bifurcation, the amplitude modulations can be shown and the results present $2T$ and $4T$ periodicity. However, further increasing gain leads to the chaotic dynamics, and no clear amplitude modulation is shown there. The above explained dynamics was theoretical proposed and numerically proved, as shown in Figs. 2.5 and 2.6.

The fundamental setup has already demonstrated impressive performance across various metrics. Performance evaluation encompasses criteria such as phase noise, frequency tunability, size, cost, and frequency range, among others. Between these, phase noise performance emerges as one of the most important parameters, given its primary objective in achieving high-quality microwave generation. The phase noise spectrum can be quantified through experimental measurements using an electrical spectrum analyzer. Additionally, the microwave envelope equation provides a means to predict the noise spectrum, a topic that will be discussed in Chapter 5.

In an ideal oscillator, characterized by the absence of phase noise, the frequency spectrum at the oscillation frequency should exhibit a Dirac peak. However, achieving this in real-world oscillators is not feasible. Instead, a flat noisy background is typically added to the spectrum primarily due to *amplitude noise*, while the linewidth is broadened as a consequence of *phase noise*. Although the amplitude noise can usually be managed effectively, our primary concern centers around addressing phase noise.

Unless various spectral diversity can happen by depending on the sources of noise, the best approximation of the line broadening due to phase noise can be represented by a Lorentzian shape,

$$\mathcal{L}(f_{\text{off}}) \propto \frac{D}{D^2 + f_{\text{off}}^2} \tag{2.41}$$

near the carrier frequency, expressed in units of dBc/Hz (decibels relative to the carrier), where f_{off} represents the offset frequency from the carrier, and D denotes the diffusion constant of Gaussian white noise [68]. Phase noise spectrum can represent relative power differences between a power at a carrier frequency and noise powers at offset frequencies. When we define the power at a carrier frequency in dBm, we measure noise power within a 1 Hz bandwidth at a specific offset frequency [in units of dBm/Hz]. Then, once we subtract the carrier power from the noise power, it is possible to measure the phase noise at the offset frequency, where it should have a negative sign, and the phase noise, the gap between the two measure quantities, can be expressed in units of dBc/Hz where "c" stands for relative to carrier.

When we generally look at the single sideband spectrum, a flicker shape is initially observed at low offset frequencies. However, as the offset frequency increases, the system eventually manifests spurious peaks, primarily due to the FSR of the delay spool [35, 63]. The phenomenon will be thoroughly explored in Chapter 5. In many instances, noise levels are compared at 10 kHz offset frequency, as it provides insight into the Doppler echo typically encountered at typical flight speeds.

The simple setup has achieved remarkable performance in the X-band (8 to 12 GHz), C-band (4 to 8 GHz), and lower frequency ranges, boasting phase noise levels even lower than -140 dBc/Hz at 10 kHz offset frequency [35–40]. However, a notable challenge of the basic setup lies in achieving similar levels of phase noise performance in higher frequency bands. This difficulty primarily stems from the degradation in performance of electronic components at higher frequencies. To address these concerns, numerous new techniques have been proposed. In the upcoming chapter, we introduce a frequency-multiplicative approach. This method enables us to generate an output that is a multiple of the oscillation frequency, thereby alleviating the strain on electronic components.

Chapter 3: The Frequency-Multiplicative OEOs

3.1 Introduction of the Chapter

Despite the impressive phase noise performance of the basic setup outlined in Chapter 2, one limitation lies in the challenge of achieving high microwave frequencies, particularly accessing the millimeter-wave range. This difficulty arises because the oscillation frequency is determined by the filter, and it means that to generate higher frequencies, a corresponding filter is required. However, this approach becomes impractical when considering costs of filters in the millimeter-wave range and significant degradation in performance of electronic components with increased frequency range. To address this concern, a frequently employed method is frequency multiplication.

Frequency multiplication is a widely employed technique for easily accessing the millimeter-wave frequency range [41–51]. The OEOs for the frequency multiplication feature multipath structures to tune the oscillation frequency in their closed-loops, akin to the basic architecture of OEOs, while generating harmonics of the oscillation frequency at separate output ports by controlling the state of polarization or phase of optical fields. Consequently, they alleviate the burden on electronic components while enabling access to high frequency ranges.

This chapter delves into the dynamics of the four frequency-multiplicative OEOs, as developed in the following references [47–50]. We respectively name the four models as the frequency-doubled OEO, the frequency-doubled OEO using a chirped fiber bragg grating (CFBG), the

Sagnac-loop OEO, and the OEO based on cascaded modulators, with their names derived from their constructional or dynamical characteristics. Section 3.2 describes the dynamics of the frequency-doubled OEO, which achieves doubled-frequency generation by controlling the state of polarization of optical fields. Section 3.3 depicts the dynamics of the frequency-doubled OEO using a CFBG, which achieves doubled-frequency generation by controlling the phase of optical fields through a CFBG. Section 3.4 elucidates the dynamics of another frequency-doubled OEO that utilizes a Sagnac-loop to control phase and polarization of optical fields. This section also incorporates a tunable electronic filter to achieve fine tunability. Section 3.5 demonstrates the dynamics of an OEO featuring a tunable frequency-multiplication factor capable of generating up to octupled-frequency. The analysis of the four models is summarized and concluded in Section 3.6.

3.2 The Frequency-Doubled OEO

3.2.1 System

Figure 3.1 illustrates the frequency-doubled OEO that outputs the second harmonic of the loop frequency by controlling the polarization state of various optical signals [47]. The PC plays a crucial role in performing polarization multiplexing via a polarization shift α. In the lithium niobate crystal, the modulation efficiency of the principal axis (y-pol) is greater than the one of the x-pol because of the difference in corresponding half-wave voltages [69]. Consequently, one can ignore the x-pol modulation, and only odd-ordered sidemodes exists in the x-pol owing to the MITP operation of the MZM. This phenomenon results in the double-frequency signal generation at the output [see Fig. 3.1 (a)] while the fundamental frequency is resonant with the closed-loop

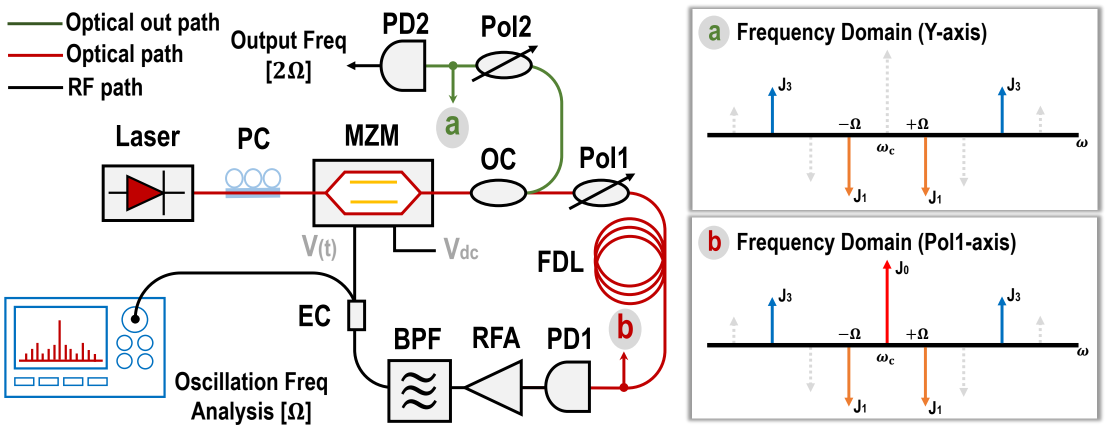

Figure 3.1: Schematic representation of the frequency-doubled OEO that consists of a continuous wave laser, a polarization controller (PC), a Mach-Zehnder modulator (MZM), an optical coupler (OC), two polarizers (Pols), a fiber delay line (FDL), two photodetectors (PDs), a radiofrequency amplifier (RFA), a bandpass filter (BPF), and an electric coupler (EC). Due to a property of the MZM, only the y-pol carrier is modulated while the x-pol is not. (a) As Pol2 filters out the x-pol carrier, there are only odd-ordered modes and their beatnotes are frequency-doubled. (b) As Pol1 ensures that all modes are back to the same polarization state, so that the system oscillates in the fundamental frequency.

resonator [see Fig. 3.1 (b)].

3.2.2 The Oscillation Frequency Generation

When we define $V(t)$ as the RF signal feeding of the MZM, the two orthogonal waves can be expressed as

$$\mathcal{E}_x = \sqrt{P_0}\sin(\alpha) \tag{3.1}$$

$$\mathcal{E}_y(t) = \sqrt{P_0}\cos(\alpha)\cos\left\{\frac{\pi V(t)}{2V_{\pi_{\mathrm{RF}}}} + \frac{\pi}{2}\right\}. \tag{3.2}$$

Pol1 has 45° state of polarization with respect to the principal axis and permits polarization alignment. After the direct detection, the input of the BPF can be explicitly obtained as

$$V_{\text{in}}(t) = \frac{\kappa S_1 G}{2} |\mathcal{E}_x + \mathcal{E}_y(t-T)|^2 \tag{3.3}$$

where S_1 is the responsivity of PD1. Using Eq. (2.3) and Eq. (3.3), the integro-differential equation of the model becomes identical to Eq. (2.18) with $x(t) = \pi V(t)/(4V_{\pi_{\text{RF}}})$, and $\gamma = \pi\kappa S_1 G P_0 \sin(2\alpha)/(4V_{\pi_{\text{RF}}})$. Here we define $x(t)$ with a factor 4 in the denominator instead of 2 (as defined in Section. 2.3) in order to have the same argument $2|\mathcal{A}_T|$ for the Bessel functions. This adjustment ensures that the envelope equation of the model can be written exactly as Eq. (2.19).

3.2.3 The Doubled Frequency Generation

In contrast with the basic OEO, we need to consider the output separately. The direction of Pol2 corresponds to the y-pol and the optical carrier is removed. Then, the output voltage is

$$\begin{aligned} V_{\text{o}}(t) &= S_2 P_0 \cos^2(\alpha) \cos^2 \left\{ 2|\mathcal{A}| \cos[\Omega_0 t + \psi(t)] + \frac{\pi}{2} \right\} \\ &= S_2 P_0 \cos^2(\alpha) \mathrm{J}_2[4|\mathcal{A}|] \cos[2\Omega_0 t + 2\psi(t)] \end{aligned} \tag{3.4}$$

by assuming the higher even-ordered terms can be neglected from the small signal oscillation. We also omit the time-domain expression of the envelope for simplicity, $\mathcal{A}(t) \to \mathcal{A}$. In order to explicitly compare the output voltage $V_{\text{o}}(t)$ with the oscillating signal $V(t)$, we define a dimensionless voltage $v_{\mathrm{o}}(t) = \pi V_{\mathrm{o}}(t)/(4V_{\pi\mathrm{RF}})$, also equal to

$$v_{\mathrm{o}}(t) = \frac{1}{2}\mathcal{C}(t)e^{i2\Omega_0 t} + \frac{1}{2}\mathcal{C}^*(t)e^{-i2\Omega_0 t} \tag{3.5}$$

where the dimensionless output envelope is equal to

$$\mathcal{C} = G_{\mathrm{o}}\mathrm{J}_2[4|\mathcal{A}|]e^{i\varphi(t)}. \tag{3.6}$$

We also omit the time-domain expression of the output envelope. And, the output gain is

$$G_{\mathrm{o}} = \frac{\pi S_2 P_0 \cos^2(\alpha)}{4V_{\pi\mathrm{RF}}}. \tag{3.7}$$

Due to the fact that $\varphi(t) = 2\psi(t)$, the phase noise of the doubled-frequency should at least be $20\log_{10} 2 = 6$ dB worse than the one of the fundamental frequency.

3.3 The Frequency-Doubled OEO Using a CFBG

3.3.1 System

The schematic representation of the frequency-doubled OEO employing a CFBG is illustrated in Fig. 3.2 [48]. A notable aspect of this configuration is its polarization insensitivity, as the frequency-doubling is a result of phase control. The DP-MZM, comprising two parallel MZMs, serves as a third Mach-Zehnder interferometer, generating the two outputs in phase quadrature. The output of the DP-MZM demonstrates orthogonality between the carrier and sidemodes due to the shorted upper MZM and the MITP biased lower MZM [refer to Fig. 3.2(a)]. Without

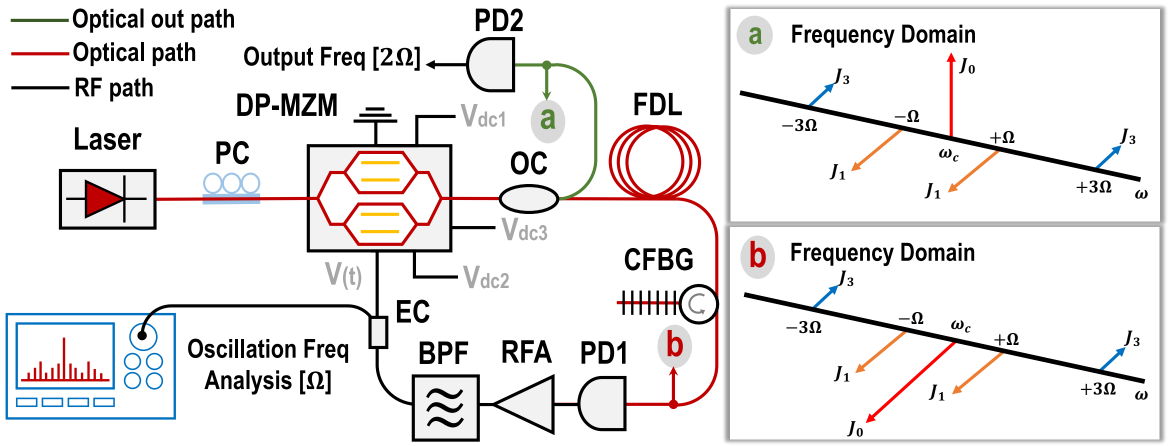

Figure 3.2: Schematic representation of the frequency-doubled OEO using a CFBG that consists of a laser, a polarization controller (PC), a dual-parallel Mach-Zehnder modulator (DP-MZM), an optical coupler (OC), a fiber delay line (FDL), a circulator (Circ), a chirped fiber bragg grating (CFBG), two photodetectors (PDs), an radiofrequency amplifier (RFA), a bandpass filter (BPF), and an electric coupler (EC). a) the DP-MZM implements a carrier phase shifted double sideband modulation and the fundamental (oscillation) frequency is highly suppressed at the output. b) the CFBG drags all modes to recover the fundamental frequency in the oscillation loop. Note that comparing a) and b) expresses phase differences, not states of polarizations.

proper phase alignment, the fundamental frequency experiences significant suppression in direct detection, which results in the second harmonic becomes the dominant output frequency. To ensure the oscillation of the fundamental frequency, a dispersion-compensating fiber is integrated before PD1, functioning akin to a CFBG by aligning the carrier with the first sidemodes in phase [refer to Fig. 3.2(b)].

3.3.2 The Oscillation Frequency Generation

If we define the output envelopes of the lower and upper MZMs respectively as $\mathcal{E}_1(t)$ and $\mathcal{E}_2(t)$, the output of the DP-MZM can be written as follows

$$\mathcal{E}(t) = \mathcal{E}_1(t) + i\mathcal{E}_2(t) = \frac{\sqrt{P_0}}{2}\left[\cos\left\{\frac{\pi V(t)}{2V_{\pi_{\mathrm{RF}}}} + \frac{\pi}{2}\right\} + i\cos\phi\right]. \tag{3.8}$$

ϕ represents the offset phase of the upper MZM. Subsequently, the field is coupled into the CFBG via a delay line, facilitating phase alignment. Assuming that the zeroth and first sidemodes are dominant compared to higher-ordered modes due to the small-signal modulation index, the output of the CFBG is then shaped as

$$\begin{aligned}\mathcal{E}_{\mathrm{CFBG}}(t) = \frac{\sqrt{P_0}}{2}\Bigg\{ & ie^{i\theta_0}\cos\phi - \mathrm{J}_1\left[\frac{\pi|\mathcal{V}_T|}{2V_{\pi_{\mathrm{RF}}}}\right]e^{i\{\Omega_0(t-T)+\psi_T+\theta_1\}} \\ & - \mathrm{J}_1\left[\frac{\pi|\mathcal{V}_T|}{2V_{\pi_{\mathrm{RF}}}}\right]e^{-i\{\Omega_0(t-T)+\psi_T-\theta_2\}}\Bigg\} \end{aligned} \tag{3.9}$$

where the three phase shifts, denoted as θ_0, θ_1, and θ_2, are the results of the CFBG. Each of them undergoes distinct phase shift, which can be individually identified as

$$\begin{aligned}\theta_0 &= L_{\mathrm{bg}}\beta_p(\omega_c) \\ \theta_1 &= L_{\mathrm{bg}}\beta_p(\omega_c) + L_{\mathrm{bg}}\dot{\beta}_p(\omega_c)\Omega_0 + L_{\mathrm{bg}}\ddot{\beta}_p(\omega_c)\Omega_0^2/2 \\ &\approx L_{\mathrm{bg}}\beta_p(\omega_c) + L_{\mathrm{bg}}n_{\mathrm{bg}}\Omega_0/c - L_{\mathrm{bg}}D_{\mathrm{bg}}\lambda_c^2\Omega_0^2/(4\pi c) \\ \theta_2 &= L_{\mathrm{bg}}\beta_p(\omega_c) - L_{\mathrm{bg}}\dot{\beta}_p(\omega_c)\Omega_0 + L_{\mathrm{bg}}\ddot{\beta}_p(\omega_c)\Omega_0^2/2 \\ &\approx L_{\mathrm{bg}}\beta_p(\omega_c) - L_{\mathrm{bg}}n_{\mathrm{bg}}\Omega_0/c - L_{\mathrm{bg}}D_{\mathrm{bg}}\lambda_c^2\Omega_0^2/(4\pi c). \end{aligned} \tag{3.10}$$

$\beta_p(\omega_c)$, $\dot{\beta}_p(\omega_c)$, and $\ddot{\beta}_p(\omega_c)$ are the zeroth, first, and second order derivatives of the propagation constant at the optical carrier, λ_c is the wavelength of the incident light, c is the speed of light, D_{bg} is the dispersion constant of the fiber, n_{bg} is the refractive index of the CFBG, and L_{bg} is length of the CFBG [46].

By plugging Eq. (3.10) into (3.9), it is possible to express the output of PD1, as follows

$$V_{\text{in}}(t) = -\beta \mathrm{J}_1\left[\frac{\pi|\mathcal{V}_T|}{2V_{\pi_{\text{RF}}}}\right]\cos\left[\Omega_0(t-T)+\psi_T+\frac{L_{bg}n_{bg}\Omega_0}{c}\right]. \tag{3.11}$$

It indeed presents that the CFBG recovers the fundamental frequency oscillation, and the generalized loop gain is equivalent to

$$\beta = -\kappa S_1 G P_0 \cos\phi \sin\left(\frac{L_{\text{bg}}D_{\text{bg}}\lambda_c^2\Omega_0^2}{4\pi c}\right). \tag{3.12}$$

Given the results, the BPF equation of the model can be explicitly written as

$$\begin{aligned} x(t)+&\frac{1}{\Delta\Omega}\frac{d}{dt}x(t)+\frac{\Omega^2}{\Delta\Omega}\int_{t_0}^{t}x(s)ds = \\ &-\gamma \mathrm{J}_1[2|\mathcal{A}_T|]\cos[\Omega(t-T)+\psi_T+L_{\text{bg}}n_{\text{bg}}\Omega/c] \end{aligned} \tag{3.13}$$

where

$$x(t)=\frac{\pi V(t)}{4V_{\pi_{\text{RF}}}},\ \ \mathcal{A}=\frac{\pi\mathcal{V}(t)}{4V_{\pi_{\text{RF}}}},\ \ \gamma=\frac{\pi\beta}{4V_{\pi_{\text{RF}}}}. \tag{3.14}$$

In contrast with the preceding models, Eq. (3.13) incorporates an extra constant phase term, $L_{\text{bg}}n_{\text{bg}}\Omega_0/c$. However, it is still possible to write the envelope equation of the current setup as Eq. (2.19). We can simply integrate the constant phase into the cumulative gain by setting $\sigma = \Omega_0 T + L_{\text{bg}}n_{\text{bg}}\Omega_0/c$.

3.3.3 The Doubled Frequency Generation

In the absence of additional phase control, the carrier phase-shifted double sideband modulation scheme prominently suppresses the fundamental frequency, which results in the second harmonic generation as the output, as illustrated by

$$V_{\mathrm{o}}(t) = \frac{S_2 P_0}{4} \mathrm{J}_2[4|\mathcal{A}|] \cos\left[2\Omega_0 t + 2\psi(t)\right], \tag{3.15}$$

If we define a dimensionless output voltage as $v_{\mathrm{o}}(t) = \pi V_{\mathrm{o}}(t)/(4V_{\pi\mathrm{RF}})$, the output envelope is easily obtained as

$$\mathcal{C} = G_{\mathrm{o}} \mathrm{J}_2[4|\mathcal{A}|] e^{i\varphi(t)} \tag{3.16}$$

where the output gain is

$$G_{\mathrm{o}} = \frac{\pi S_2 P_0}{16 V_{\pi_{\mathrm{RF}}}}. \tag{3.17}$$

The expression of the output signal is equivalent to Eq. (3.6).

3.4 The Sagnac-Loop OEO

3.4.1 System

As depicted in Fig. 3.3, the frequency-tunable OEO utilizing a Sagnac-loop executes phase and intensity modulation separately [49]. At the polarization beam splitter level, the optical

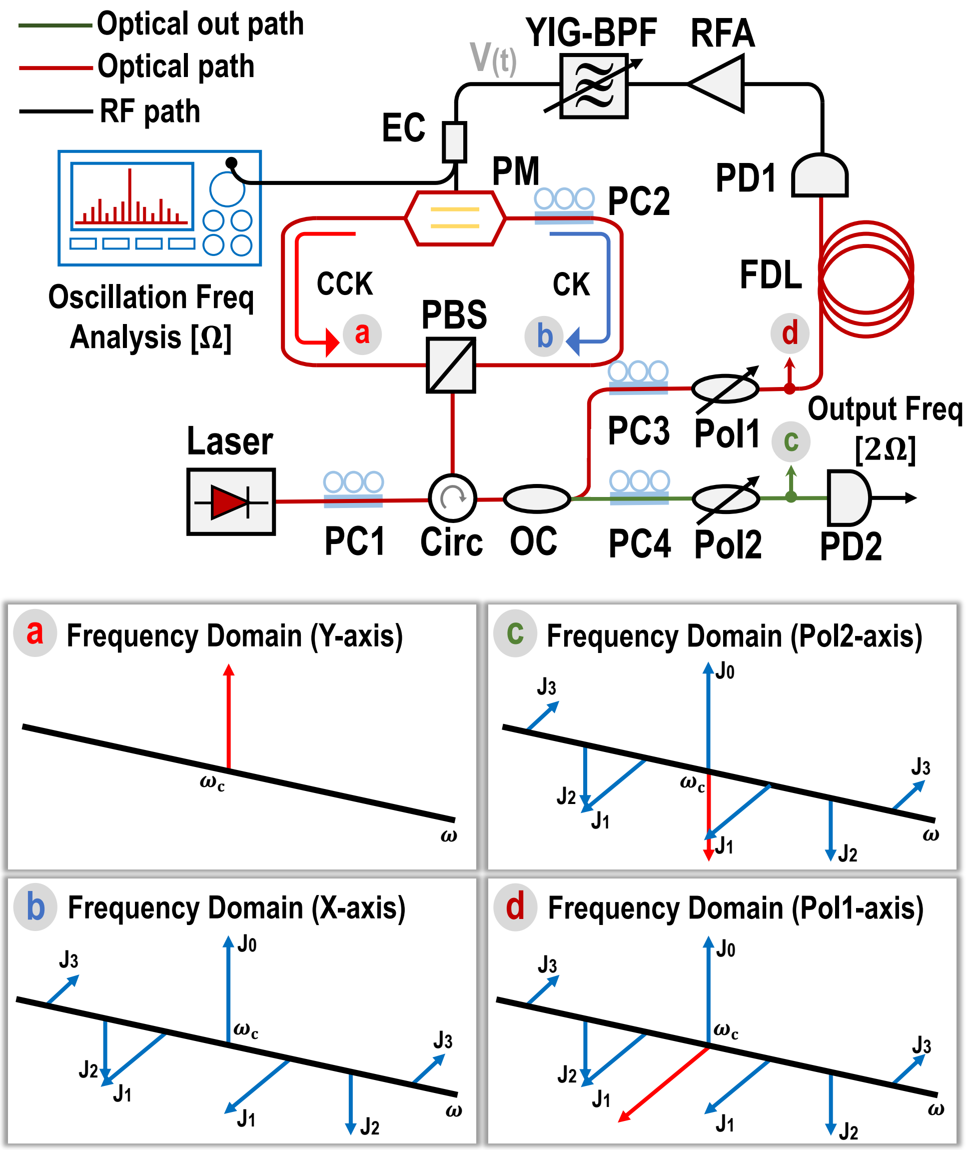

Figure 3.3: Schematic representation of the frequency-tunable OEO using a Sagnac-loop that consists of a continuous wave laser, four polarization controllers (PCs), a polarization beam splitter (PBS), a phase modulator (PM), a circulator (Circ), an optical coupler (OC), two polarizers (Pols), two photodetectors (PDs), a fiber delay line (FDL), a radiofrequency amplifier (RFA), a Yttrium-iron-garnet bandpass filter (YIG-BPF), and an electric coupler (EC). (a) and (b) indicate modulated waves where red and blue colors respectively result from the counter clockwise (CCK) and clockwise (CK) wave circulations. In addition, the arrow-direction indicates phases and their states of polarization are separately written next to labels. (c) and (d) illustrate the frequency domain modal distribution ahead of photodetection.

carrier is evenly and orthogonally distributed into clockwise (CK) and counterclockwise (CCK) direction. Due to velocity mismatch, the CCK wave is not phase-modulated as efficiently as the CK wave [see Fig. 3.3 (a) and (b)] [70]. PC2 is introduced to switch the state of polarization of the waves to ensure effective exit from the beam splitter. Intensity modulation is accomplished by integrating of a PC and a Pol. Consequently, the joint use of a PM, a PC, and a Pol is actually equivalent to a MZM (we call it simply equivalent-MZM) [71]. The configuration has two equivalent-MZMs and they are differently biased [see Fig. 3.3(c) and (d)].

3.4.2 The Oscillation Frequency Generation

The phase-modulated CCK and CK waves in the Sagnac-loop can be written as

$$\mathcal{E}_{\mathrm{CK}}(t) = \sqrt{\frac{P_0}{2}} \exp\left\{ i\frac{\pi V(t)}{V_{\pi_{\mathrm{RF}}}} \right\} \text{ and } \mathcal{E}_{\mathrm{CCK}} = \sqrt{\frac{P_0}{2}} \tag{3.18}$$

where $V(t)$ is the RF input of the PM. If either PC3 or PC4 induces a phase difference of α, the output of the two Pols can be written as

$$\mathcal{E}_{\mathrm{Pol}}(t) = \frac{1}{\sqrt{2}}[\mathcal{E}_{\mathrm{CK}}(t) + \mathcal{E}_{\mathrm{CCK}} e^{-i\alpha}]. \tag{3.19}$$

The purpose of both Pols is to combine two lightwaves on a polarization space. Starting from this point, we do not need to consider states of polarization, but instead, the parameter that matters is the phase difference. For the oscillation loop, we set $\alpha = \pi/2$, and the input voltage of the filter can be written as

$$V_{\text{in}}(t) = -\kappa S_1 G P_0 \mathrm{J}_1\left[\frac{\pi|\mathcal{V}_T|}{V_{\pi_{\text{RF}}}}\right]\cos[\Omega_0(t-T)+\psi_T]. \tag{3.20}$$

The BPF dynamics becomes identical to Eq. (2.3) and if we define $x(t) = \pi V(t)/(2V_{\pi_{\text{RF}}})$ and $\gamma = \pi\kappa S_1 G P_0/(2V_{\pi_{\text{RF}}})$, the OEO will have an envelope equation that is identical to Eq. (2.19).

3.4.3 The Doubled Frequency Generation

PC4 induces $\alpha = \pi$ to lead the optical carrier of the CCK wave to be orthogonal to adjacent sidemodes. It causes the suppression of the fundamental frequency at photodetection level, following

$$V_{\text{o}}(t) = S_2 P_0 \mathrm{J}_2[2|\mathcal{A}|]\cos[2\Omega_0 t + 2\psi(t)]. \tag{3.21}$$

By defining the output voltage $v_{\text{o}}(t) = \pi V_{\text{o}}(t)/(2V_{\pi_{\text{RF}}})$, the output envelope can be written as

$$\mathcal{C} = G_{\text{o}}\mathrm{J}_2[2|\mathcal{A}|]e^{i\varphi(t)} \tag{3.22}$$

with the output gain $G_{\text{o}} = \pi S_2 P_0/(2V_{\pi\text{RF}})$. The expression for this output signal is equivalent to Eq. (3.6).

3.5 The OEO based on Cascaded Modulators

3.5.1 System

The graphical representation of the frequency tunable OEO using cascaded modulators is found in Fig. 3.4 [50]. A polarization modulator is a specific kind of PM supporting both transverse electric and transverse magnetic modes with opposite phase modulation indices [51]. The configuration has two equivalent-MZMs (see the previous section to understand the concept of equivalent-MZM). We define the equivalent-MZM1 as a joint use of the modulator, PC3, and Pol2, and it is operated at the QTP. The equivalent-MZM2 consists of the modulator, PC2, and Pol1 while it is modulated again to achieve tunable multiplication by a factor up to 8. We define beforehand the following parameters: *(i)* $V_{\pi_{\mathrm{RF1}}}$ is the half-wave voltage of the polarization modulator; *(ii)* $V_{\pi_{\mathrm{RF2}}}$ is the half-wave voltage of the MZM; *(iii)* θ_1 is a tunable phase of the phase shifter; *(iv)* θ_2 is the offset phase of the MZM.

3.5.2 The Oscillation Frequency Generation

Let us define $V(t)$ as the RF driving voltage of the polarization modulator or input of the shifter. PC1 has a 45° polarization angle with respect to the principal axis of the polarization modulator. Therefore, the orthogonal output of the modulator can be expressed as

$$\begin{aligned}
&\mathcal{E}_x(t) = \sqrt{\frac{P_0}{2}} \exp\left\{ i\frac{\pi V(t)}{V_{\pi_{\mathrm{RF1}}}} \right\} \\
&\mathcal{E}_y(t) = \mathcal{E}_x^*(t).
\end{aligned} \tag{3.23}$$

Since the purpose of the Pols is polarization alignment, the output of any equivalent-MZM can be written as

$$\mathcal{E}(t) = \frac{1}{\sqrt{2}}[\mathcal{E}_x(t) + \mathcal{E}_y(t)e^{-i\alpha}], \tag{3.24}$$

where it is biased at the QTP if $\alpha = \pi/2$, the MATP if $\alpha = 0$, and the MITP if $\alpha = \pi$. Once the equivalent-MZM1 is operated at the quadrature point, the BPF relation is established as identical to Eq. (2.18) with $x(t) = \pi V(t)/V_{\pi_{\mathrm{RF1}}}$ $\gamma = \pi\kappa S_1 G P_0/V_{\pi_{\mathrm{RF1}}}$. The envelope equation will be the same as Eq. (2.19).

Equation (3.24) is modulated again by the MZM, and the output can be written as

$$\mathcal{E}_{\mathrm{o}}(t) = \mathcal{E}(t)\cos\left\{|\mathcal{B}(t)|\cos[\Omega_0 t + \psi(t) + \theta_1] + \theta_2\right\} \tag{3.25}$$

where the normalized voltage is defined as $|\mathcal{B}(t)| = \pi|\mathcal{V}(t)|/(2V_{\pi_{\mathrm{RF2}}})$. We also omit the time domain expression of $\mathcal{B}(t)$, thereby $\mathcal{B}(t) \to \mathcal{B}$. By tuning the parameters of Eq. (3.25), it is possible to have an adjustable multiplicative factor, as discussed below.

3.5.3 The Quadrupled Frequency Generation

We operate both the two MZMs (equivalent-MZM2 and the MZM) at the MITP while the shifter induces a phase shift $\theta_1 = \pi/2$. One can approximate the output of the MZM to $\mathcal{E}_o(t) \simeq i2\sqrt{P_0}\mathrm{J}_1[|\mathcal{A}|]\mathrm{J}_1[|\mathcal{B}|]\sin[2\Omega_0 t + 2\psi(t)]$ where the modulation indices are set to obey $\mathrm{J}_1[|\mathcal{A}|]\mathrm{J}_1[|\mathcal{B}|] \gg \mathrm{J}_1[|\mathcal{A}|]\mathrm{J}_3[|\mathcal{B}|] > \mathrm{J}_3[|\mathcal{A}|]\mathrm{J}_1[|\mathcal{B}|] > \cdots$. Finally, the direct detection of $\mathcal{E}_o(t)$ is the quadrupled frequency. If we define a dimensionless voltage $v_{\mathrm{o}}(t) = \pi V_{\mathrm{o}}(t)/V_{\pi\mathrm{RF1}}$, the

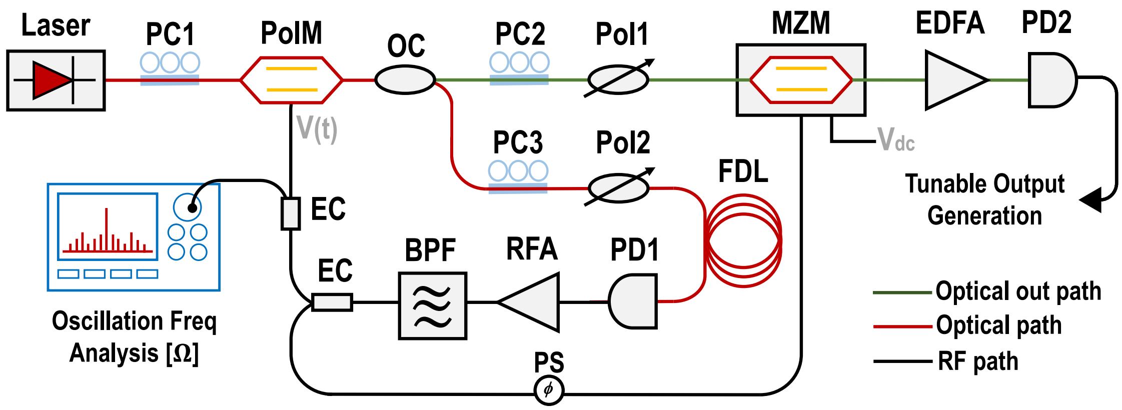

Figure 3.4: Schematic representation of the tunable frequency multiplicative OEO that consists of a continuous wave laser, three polarization controllers (PCs), a polarization modulator (PolM), an optical coupler (OC), two polarizers (Pols), a fiber delay line (FDL), two photodetectors (PDs), a radiofrequency amplifier (RFA), a bandpass filter (BPF), two electric couplers (ECs), a phase shifter (PS), a Mach-Zehnder modulator (MZM), and an Erbium-doped fiber amplifier (EDFA). A joint use of a PolM, a PC, and a Pol is equivalent to a MZM, so we label that as equivalent-MZM. The equivalent-MZM1 consists of the PolM, the PC3, and the Pol2, and the equivalent-MZM2 consists of the PolM, the PC2, and the Pol1. The cascaded use of the equivalent-MZM2 and the MZM achieves an adjustable frequency multiplicative factor.

output envelope $\mathcal{C}$ can be written as $\mathcal{C} = G_o \mathrm{J}_1^2[|\mathcal{A}|]\mathrm{J}_1^2[|\mathcal{B}|]e^{i(\varphi(t)+\pi)}$ where the phase satisfies $\varphi(t) = 4\psi(t)$, and the output gain is $G_o = 2\pi S_2 P_0/(V_{\pi\mathrm{RF1}})$.

3.5.4 The Sextupled Frequency Generation

In this configuration, we need to bias the equivalent-MZM2 at the MATP and the MZM at the MITP while the shifter does not induce shift. One additional setting is $|\mathcal{A}| = |\mathcal{B}|$ which is achieved by adjusting the bias voltages of the modulators. If we set $|\mathcal{A}| \simeq |\mathcal{B}| \simeq 1.91$, the Bessel functions obey $\mathrm{J}_1[|\mathcal{A}|] > \mathrm{J}_2[|\mathcal{A}|] > \mathrm{J}_0[|\mathcal{A}|] > \mathrm{J}_3[|\mathcal{A}|] \gg \cdots$. Under these conditions, the output can be written as $\mathcal{E}_o(t) \simeq 2\sqrt{P_0}\big\{\mathrm{J}_1[|\mathcal{A}|]\mathrm{J}_2[|\mathcal{A}|] + \mathrm{J}_0[|\mathcal{A}|]\mathrm{J}_3[|\mathcal{A}|]\big\}\cos[3\Omega_0 t + 3\psi(t)]$ where the amplitude of the fundamental frequency term is close to 0. This procedure achieves the sextupled-frequency generation.

3.5.5 The Octupled Frequency Generation

We bias the MZMs at the MATP while tuning the phase shifting to $\pi/2$. Also, we set $|\mathcal{A}| \simeq |\mathcal{B}| \simeq 1.70$, so that $\mathrm{J}_0[|\mathcal{A}|] > \mathrm{J}_2[|\mathcal{A}|] \gg \cdots$. The maximum point does not generate odd-ordered term and we can only consider the zeroth and second order Bessel functions which lead to $\mathcal{E}_o(t) \simeq -2\sqrt{P_0}\mathrm{J}_2^2[|\mathcal{A}|]\cos[4\Omega_0 t + 4\psi(t)]$. The beating of the fourth sidemodes generates the octupled-frequency as the output of PD2.

3.6 Conclusion of the Chapter

We have studied the dynamics of the four frequency multiplicative OEOs, which successfully manipulate the state of polarization and phase of optical fields to generate harmonics of the oscillation frequency at the output ports. The models streamline the loads of electronic components thanks to the harmonic generations and achieve frequency-tunability through the utilization of the RF tunable filter or by regulating the transmission points of the cascaded modulators. Notably, the envelope equations of these models are equivalent to that of the basic architecture shown in Eq. (2.19), which implies the dynamical similarities between the OEOs [63].

However, several concerns remain unresolved. The first issue is the limited frequency-tunability of the systems. The Sagnac-loop OEO can achieve fine tunability by using the tunable RF filter, but the component is bulky and expensive to be commercialized. The OEO based on cascaded modulators has demonstrated that the potential for achieving a tunable multiplication factor by controlling the transmission points of the cascaded modulators. However, the resolution of frequency tuning is limited, given that it operates on a multiplication factor. More importantly, a well-known challenge arises from the fact that this technique inevitably entails a 6 dB decrease in phase noise for every octave increase in frequency. Considering additional noise contributions from other components within the multi-loop structure, the resulting degree of phase noise may prove unacceptable. The aforementioned issues have prompted researchers to explore frequency selection in the optical domain, thereby achieving MPFs.

Chapter 4: The OEO based on Stimulated Brillouin Scattering

4.1 Introduction of the Chapter

The models shown in Chapters 2 and 3 have already presented great performances in terms of high frequency generation and low phase noise, but a critical drawback is that since the filtering still occurs in the RF domain, the resulting oscillators are generally not tunable in frequency. Another drawback is narrowband RF filtering in the millimeter-wave range becomes progressively less effective as the frequency increases.

Both these problems are addressed by OEOs based on SBS. Using Brillouin scattering to improve the functionalities of OEOs is a widespread strategy that has been implemented in various platforms [52–55]. In the configuration of interest in this chapter, a pump laser is launched in a highly nonlinear fiber spool in order to generate a Brillouin gain profile at an adjacent redshifted frequency. This process permits the selective amplification of a phase-modulated and contra-propagating laser signal. Most importantly, the RF oscillation frequency solely depends on the spectral gap between the pump and signal lasers and is thereby easily tunable. From that regard, a main characteristic of this approach is that frequency selection is achieved by the means of a MPF instead of an RF filter [56–58]. Once the RF beatnote is generated after photodetection, it is filtered, amplified, and fed back to the PM to close the optoelectronic loop. It has been demonstrated by several research groups that these SBS-based

OEOs feature frequency tunability from DC to more than 60 GHz and an ultra-low phase noise figure [59–61]. In fact, the km-long fiber spool can be replaced by a sub-cm-long highly nonlinear waveguide, and in that case, the system has the potential to be reduced to a chipscale size [62].

Despite the potential and many distinctive advantages of SBS-based OEOs, no dynamical model has ever been proposed to describe their nonlinear behavior. Indeed, Chapters 2 and 3 have shown that it is in general possible to obtain an equation for the envelope of the microwave generated by these OEOs. In this chapter, we undertake a theoretical analysis showing that an delay-differential envelope equation for SBS-OEOs can be derived, analogously to what had been done earlier for the conventional architectures of OEOs. In agreement is shown that as the gain is increased, the system undergoes a primary Hopf bifurcation and then a secondary Neimark-Sacker bifurcation before being driven to fully developed chaos, presenting dynamical similarities with the basic OEO shown in Chapter. 2.

The outline of this chapter is following. In Section 4.2, the SBS-based OEO is presented, and its principle of operation is described. Section 4.3 is devoted to the analysis of the SBS dynamics, and an input-output relationship is derived for the selectively amplified signal wave. The dynamical characterization of the SBS-based MPF enables us to obtain a time-domain differential equation for the OEO in Section 4.4. Sections 4.5 and 4.6 are focused on evaluating the stability of the stationary dynamical states predicted by the model in the cases where the frequency-selective amplification is mediated by a km-long fiber delay line ($T \neq 0$) or by a sub-cm-long waveguide ($T \simeq 0$), respectively. The last section concludes the article.

4.2 System and Operation Principle

The schematic representation of the SBS-based OEO is presented in Fig. 4.1. The dynamics of this system can be described by two key variables. The first one relates to electric field $E(t)$ at the input of the PM, while the second relates to the voltage $V(t)$ feeding the modulator. Instead of working directly with the real-valued variables $E(t)$ and $V(t)$, we use instead their complex slowly-varying amplitudes $\mathcal{E}(t) = E(t)e^{i\varphi(t)}$ and $\mathcal{V}(t) = V(t)e^{i\psi(t)}$ defined through

$$E(t) = \frac{1}{2}\mathcal{E}(t)e^{i\omega_0 t} + \frac{1}{2}\mathcal{E}^*(t)e^{-i\omega_0 t} \tag{4.1}$$

$$V(t) = \frac{1}{2}\mathcal{V}(t)e^{i\Omega_0 t} + \frac{1}{2}\mathcal{V}^*(t)e^{-i\Omega_0 t}\,, \tag{4.2}$$

where ω_0 and Ω_0 are the angular frequencies associated with the signal infrared laser beam (around 1550 nm) and to the microwave signal (multi-GHz frequency to be defined later), respectively.

The pump optical path is also called high-order frequency selection branch, and it is where the RF frequency Ω_0 is determined. The *pump* field is $E_{\rm p}(t)$ while $E_{\rm s}(t)$ and $E_{\rm s}(t)$ is the phase-modulated *signal* field that is launched at the input of the highly nonlinear fiber. The two waves counter-propagate in the nonlinear fiber spool, and the pump wave stimulates Brillouin backscattering. The frequencies of the fields involved in this process are related as $\omega_{\rm p} = \omega_0 + \Omega_0 + \Omega_{\rm B}$, so that the RF output frequency can be obtained as

$$\Omega_0 = \omega_{\rm p} - \omega_0 - \Omega_{\rm B} \tag{4.3}$$

where $\Omega_{\rm B}$ is the Brillouin shift in the fiber (typically $2\pi \times$ 10–20 GHz). In the oscillator, the first

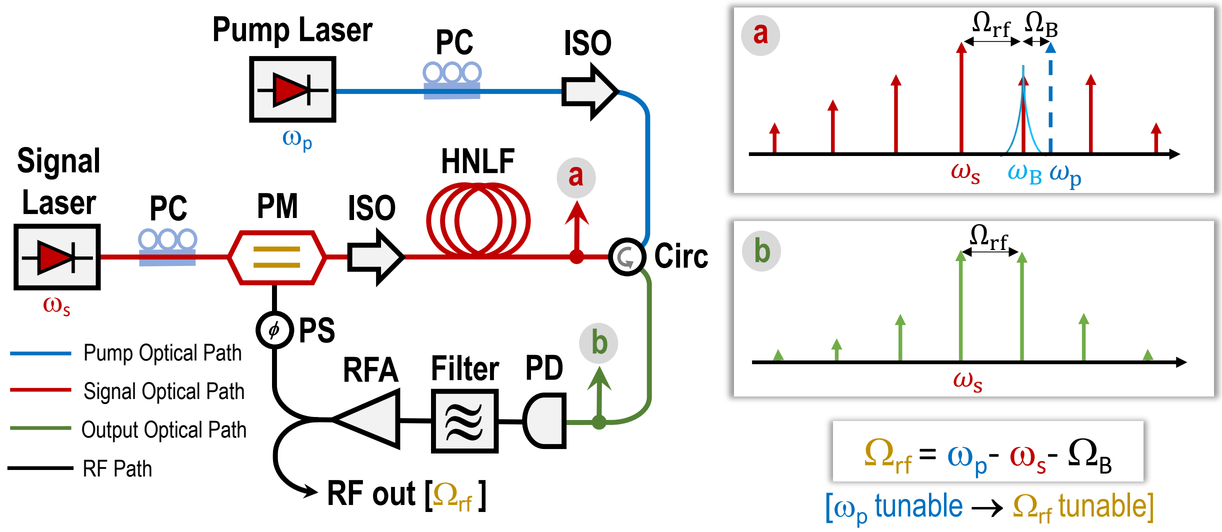

Figure 4.1: The schematic representation of the OEO based on SBS, for the generic case where $T \neq 0$ that consists of a pump laser, a signal laser, two polarization controllers (PCs), a phase modulator (PM), two isolators (ISOs), a high nonlinear fiber delay line (HNLF), a circulator (Circ), a photodetector (PD), a filter, a radiofrequency amplifier (RFA), and a phase shifter (PS).

blue-sidemode is chosen for the SBS amplification. The peak of the Brillouin gain is such that $\omega_B = \omega_p - \Omega_B$, and the MPF amplifies this mode while narrowing its linewidth [see Fig. 4.1(a)]. In Eq. (4.3), the frequencies ω_0 and Ω_B are fixed: however, the tunability of ω_p allows the RF output frequency to be tunable as well. As a result of the frequency-selective amplification, the zeroth (central) and first-order (blue-side) modes of the phase-modulated signal beam become dominant [see Fig. 4.1(b)], and their spectral spacing defines the RF beatnote frequency after photodetection.

It is important to note that one of the most outstanding challenge in OEO technology is the generation of millimeter-wave [72–75]. In general, achieving such high frequencies ($>$ 30 GHz) is achieved via frequency multiplication. Additionally, the other outstanding challenge for OEOs is tunability, which has been addressed using several different techniques [49, 76–84]. From that perspective, a key advantage of SBS-based OEOs is that they address both challenges simultaneously and the only limitation for the maximal frequency of the RF signal

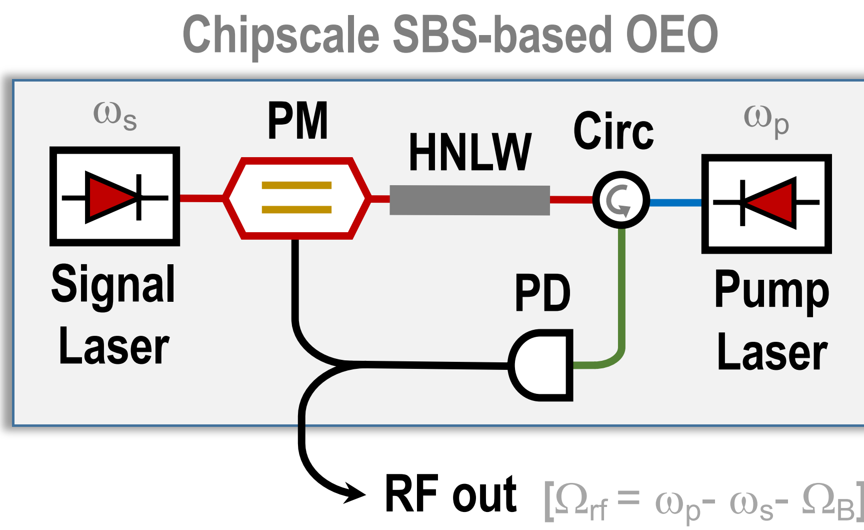

Figure 4.2: The schematic representation of the chipscale SBS-based OEO. This system corresponds to zero-delay case by containing only essential components which are a pump laser, a signal laser, a phase modulator (PM), a high nonlinear waveguide (HNLW), a circulator (Circ), and a photodetector (PD).

is the bandwidth of the PD and PM.

4.3 Frequency-Selective Amplification Based on SBS

4.3.1 Brillouin Amplification

The phenomenology of frequency-selective Brillouin amplification is the following. We consider that the highly nonlinear fiber of length L and aligned along an axis z such that the fiber is located at $0 \leq z \leq L$. The pump laser wave

$$E_{\mathrm{p}}(t) = \frac{1}{2}\mathcal{E}_{\mathrm{p}} e^{i\omega_{\mathrm{p}} t} + \frac{1}{2}\mathcal{E}_{\mathrm{p}}^{*} e^{-i\omega_{\mathrm{p}} t} \tag{4.4}$$

is launched on the right end (at $z = L$), with power $P_{\mathrm{p}} = |\mathcal{E}_{\mathrm{p}}|^2$ and optical frequency $\omega_{\mathrm{p}} \simeq 2\pi \times 193$ THz (i. e. $\lambda_{\mathrm{p}} \simeq 1550$ nm). As it propagates in the $-z$ direction, it creates a Lorentzian

Brillouin gain profile

$$g_{\mathrm{B}}(\omega) = g_{\mathrm{B0}} \frac{(\Delta\Omega_{\mathrm{B}}/2)^2}{(\Delta\Omega_{\mathrm{B}}/2)^2 + (\omega - \omega_{\mathrm{B}})^2} \tag{4.5}$$

around the red-shifted frequency $\omega_{\mathrm{B}} = \omega_{\mathrm{p}} - \Omega_{\mathrm{B}}$, where Ω_{B} is the Brillouin shift in the fiber (typically $2\pi \times 10$–20 GHz), $\Delta\Omega_{\mathrm{B}}$ being the full width at half-maximum of the gain profile (typically $2\pi \times 10$–50 MHz) and g_{B0} being the peak value of the Brillouin gain (in m/W).

Consider now a contra-propagating signal laser beam $E_{\mathrm{s}}(t)$ defined as

$$E_{\mathrm{s}}(t) = \frac{1}{2}\mathcal{E}_{\mathrm{s}} e^{i\omega_0 t} + \frac{1}{2}\mathcal{E}_{\mathrm{s}}^* e^{-i\omega_0 t}\,, \tag{4.6}$$

that is launched on the left end (at $z = 0$), with power $P_{\mathrm{s}} = |\mathcal{E}_{\mathrm{s}}|^2$ and a frequency that falls within the bandwidth of the Brillouin gain, that is $\omega_0 \simeq \omega_{\mathrm{B}}$ [note that this simplified situation does *not* correspond to the one described in Fig. 4.1(a), where it is a sidemode of the phase-modulated signal that is amplified, so that we have instead $\omega_0 \simeq \omega_{\mathrm{B}} + \Omega_{\mathrm{rf}}$; equivalently, one can say that both configurations are equivalent is $\Omega_{\mathrm{rf}} \equiv 0$]. The signal wave would undergo frequency-selective amplification, i.e., the spectral components of the signal falling within the bandwidth will be amplified, while those that are outside would remain unchanged (provided we ignore all other effects in the fiber, such as losses, cross- and self-phase modulation, etc.). Since the fiber has a length L, it takes a time $T = L/v_{\mathrm{g}}$ for the signal E_{s} to exit the fiber amplifier, with v_{g} being the group velocity of light in the fiber. The output signal would therefore a *selectively amplified* and *time-delayed* counterpart of the input signal, and the purpose of this section is to find the dynamical relationship between both.

4.3.2 Equations of Traveling Waves

The time-domain slowly-varying envelope of the input and output signals are written as $\mathcal{E}_{\rm s}^{\rm in}(t)$ and $\tilde{\rm E}_{\rm s}^{\rm out}(t)$, respectively (in units of $\sqrt{\rm W}$). We can introduce their corresponding intensities as $I_{\rm s}^{\rm in,out}(t) = |\mathcal{E}_{\rm s}^{\rm in,out}(t)|^2/A_{\rm eff}$ (in units of W/m^2), with $A_{\rm eff}$ being the effective area of the fiber.

If we neglect dispersion and cross/self-phase modulation in the fiber, the pump and signal intensities $I_{\rm p}(z,t)$ and $I_{\rm s}(z,t)$ at any point of the Brillouin amplifier obey the well-known equations [85, 86]

$$\frac{\partial I_{\rm p}}{\partial z} - \frac{1}{v_{\rm g}}\frac{\partial I_{\rm p}}{\partial t} = g_{\rm B0} I_{\rm s} I_{\rm p} + \alpha I_{\rm p} \tag{4.7}$$

$$\frac{\partial I_{\rm s}}{\partial z} + \frac{1}{v_{\rm g}}\frac{\partial I_{\rm s}}{\partial t} = g_{\rm B0} I_{\rm p} I_{\rm s} - \alpha I_{\rm s}\,, \tag{4.8}$$

where α stands for the linear losses in the fiber (in units of m^{-1}). Note unlike in ref. [86], the z-coordinate is here oriented along the propagation direction of the *signal* laser wave (instead of the pump wave), for being the variable of interest in our study.

We furthermore make the following two assumptions: *(i)* The pump laser power is assumed undepleted (i. e. $I_{\rm p}$ is assumed approximately constant, and such that $I_{\rm p} \gg I_{\rm s}$); *(ii)* and the losses in the fiber are negligible in comparison to the Brillouin amplification (i. e., $\alpha \simeq 0$). As a consequence, the above equations are reduced to the single equation

$$\frac{\partial I_{\rm s}}{\partial z} + \frac{1}{v_{\rm g}}\frac{\partial I_{\rm s}}{\partial t} = g_{\rm B0} I_{\rm p} I_{\rm s} \;\; \text{with} \;\; I_{\rm p} = \text{Const.}\,, \tag{4.9}$$

which has a generic solution of the form

$$I_{\mathrm{s}}(z,t) = e^{g_{\mathrm{B0}} I_{\mathrm{p}} z}\, I\left(t - \frac{z}{v_{\mathrm{g}}}\right) \tag{4.10}$$

where I is at this point an arbitrary waveform propagating along the fiber in the z direction. Indeed, the input and output signals in the fiber can be defined as

$$I_{\mathrm{s}}^{\mathrm{in}}(t) \equiv I_{\mathrm{s}}(0,t) = I\left(t\right) \tag{4.11}$$

$$I_{\mathrm{s}}^{\mathrm{out}}(t) \equiv I_{\mathrm{s}}(L,t) = e^{g_{\mathrm{B0}} I_{\mathrm{p}} L}\, I(t-T)\,, \tag{4.12}$$

where $L = v_{\mathrm{g}} T$ is the length of the Brillouin-active fiber yielding a time-delay T when light travels at the group velocity v_{g}. We therefore deduce

$$\frac{I_{\mathrm{s}}^{\mathrm{out}}(t)}{I_{\mathrm{s}}^{\mathrm{in}}(t-T)} = e^{g_{\mathrm{B0}} I_{\mathrm{p}} L} \tag{4.13}$$

and since $e^{g_{\mathrm{B0}} I_{\mathrm{p}} L} > 1$, it results as expected that owing to SBS, the output signal is an amplified version of the delayed input signal.

4.3.3 Accounting for Frequency Selection

Equation (4.13) does not account for frequency selection in the amplification process; more precisely, it assumes that the pump and the input/output signals are perfectly monochromatic signals with center frequencies ω_{p} and $\omega_0 = \omega_{\mathrm{B}}$, respectively.

Accounting for the effect of the Brillouin gain *bandwidth* on the amplification process requires rewrite Eq. (4.13) in the Fourier domain and to replace the gain parameter $g_{_{\rm B0}}$ by the Brillouin gain profile $g_{_{\rm B}}(\Omega)$, following

$$\frac{\tilde{I}_{\rm s}^{\rm out}(\Omega)}{\tilde{I}_{\rm s}^{\rm in}(\Omega)} = \frac{|\tilde{\mathcal{E}}_{\rm s}^{\rm out}(\Omega)|^2}{|\tilde{\mathcal{E}}_{\rm s}^{\rm in}(\Omega)e^{-i\Omega T}|^2} = e^{g_{\rm B}(\Omega)I_{\rm P}L} \,, \tag{4.14}$$

where $\Omega = \omega - \omega_{\rm B}$ is the frequency detuning from the center frequency of the Brillouin gain. It is important to note here that according to Eq. (4.14), the Brillouin gain viewed by the incoming signal $\tilde{I}_{\rm s}^{\rm in}(\omega)$ is *not* a Lorentzian; Instead, it is the *exponential* of a Lorentzian. This gain profile, which is can prosaically be described as a hump on top of a flat background equal to 1, provides a sound intuitive description of the Brillouin selective amplification. On the one hand, frequency components ω far outside the gain profile are not amplified [$g_{_{\rm B}}(\omega) \simeq 0$, i.e. $e^{g_{\rm B}(\omega)I_{\rm P}L} \simeq 1$] and the input signals are unaltered; On the other hand, frequency components ω inside the gain profile amplified [$g_{_{\rm B}}(\omega \simeq \omega_{\rm B}) > 0$, i.e. $e^{g_{\rm B}(\omega)I_{\rm P}L} > 1$].

We need now to rewrite Eq. (4.14) in terms of fields in the Fourier domain, so that the phase information of all the signals involved can be retrieved. We first express the Brillouin gain as

$$g_{_{\rm B}}(\Omega) = g_{_{\rm B0}} \left|\mathcal{L}_{\rm B}(\Omega)\right|^2 \,, \tag{4.15}$$

where

$$\mathcal{L}_{\rm B}(\Omega) = \frac{(\Delta\Omega_{\rm B}/2)}{(\Delta\Omega_{\rm B}/2) + i\Omega} \tag{4.16}$$

is the complex-valued Lorentzian profile as viewed by the signal field. Using the equality

$$e^{g_{\mathrm{B}}(\Omega) I_{\mathrm{p}} L} \equiv \left| e^{\frac{1}{2} g_{\mathrm{B}0} I_{\mathrm{p}} L\, \mathcal{L}_{\mathrm{B}}(\Omega)} \right|^2 \tag{4.17}$$

we can now rewrite Eq. (4.14) as

$$\frac{\tilde{\mathcal{E}}_{\mathrm{s}}^{\mathrm{out}}(\Omega)}{\tilde{\mathcal{E}}_{\mathrm{s}}^{\mathrm{in}}(\Omega) e^{-i\Omega T}} = e^{\frac{1}{2} g_{\mathrm{B}0} I_{\mathrm{p}} L\, \mathcal{L}_{\mathrm{B}}(\Omega)} \,. \tag{4.18}$$

It is not possible to perform rigorously an inverse Fourier transform for the fields $\tilde{\mathcal{E}}_{\mathrm{s}}^{\mathrm{in,out}}(\Omega)$ in Eq. (4.18). The main reason is that there is no closed-form relationship giving the inverse Fourier transform for the exponential of Lorentzian. However, one can note that for small gain (i. e. $g_{\mathrm{B}0} I_{\mathrm{p}} L \ll 1$), the exponential of a Lorentzian can be approximated to a Lorentzian superimposed to a flat background, following

$$e^{\frac{1}{2} g_{\mathrm{B}0} I_{\mathrm{p}} L\, \mathcal{L}_{\mathrm{B}}(\Omega)} \simeq 1 + \frac{1}{2} g_{\mathrm{B}0} I_{\mathrm{p}} L\, \mathcal{L}_{\mathrm{B}}(\Omega) \,. \tag{4.19}$$

which allows to perform a closed-form inverse Fourier transform for the fields $\tilde{\mathcal{E}}_{\mathrm{s}}^{\mathrm{in,out}}(\Omega)$ in Eq. (4.18).

Because of this useful mathematical property (the possibility to perform an inverse Fourier transform), we propose to generalize the small-gain expansion of Eq. (4.19) to the case of large gain. We therefore consider that gain is the sum of a flat background ($= 1$) and a Lorentzian, even in the case of large gain, that is

$$e^{\frac{1}{2}g_{\mathrm{B0}}I_{\mathrm{P}}L\,\mathcal{L}_{\mathrm{B}}(\Omega)} \simeq 1 + G_{\mathrm{o}}\mathcal{L}_{\mathrm{eq}}(\Omega) \quad \text{with} \quad \mathcal{L}_{\mathrm{eq}}(\Omega) = \frac{\mu}{\mu + i\Omega}\,, \tag{4.20}$$

where $\mathcal{L}_{\mathrm{eq}}(\Omega)$ is an equivalent Lorentzian with full width half maximum bandwidth 2μ, while G_{o} is the equivalent peak gain. The rationale behind the approximation of Eq. (4.20) is twofold. The first reason is that as explained earlier, we can find a closed-form analytical formula for the inverse Fourier transform for a Lorentzian gain, while we cannot do so for the exponential of a Lorentzian. The second reason is related to the experimental features if Brillouin grain: Indeed, in practice, the gain profile $g_{\mathrm{B}}(\Omega)$ of the Brillouin gain is only *approximated* by a Lorentzian, so that strictly speaking, expressing our gain as the exponential of the Brillouin Lorentzian in Eq. (4.14) is also an approximation, and *not* an exact result; therefore, the choice of the fitting function for the Brillouin amplification is not critical as long as that function displays the main features of frequency-selective amplification (input signal is unaltered outside of bandwidth, while it is amplified when within bandwidth; see for example [87, 88]).

For the approximation of Eq. (4.20) to be physically valid, we have to make sure that the peak value and half-linewidth values of the equivalent Lorentzian gain $1+G_{\mathrm{o}}\mathcal{L}_{\mathrm{eq}}(\Omega)$ match those of the *exact* profile $e^{\frac{1}{2}g_{\mathrm{B0}}I_{\mathrm{P}}L\,\mathcal{L}_{\mathrm{B}}(\Omega)}$. We therefore have the equalities

$$\textit{Gain peak condition:} \quad \left| e^{\frac{1}{2}g_{\mathrm{B0}}I_{\mathrm{P}}L\,\mathcal{L}_{\mathrm{B}}(0)} \right| = |1 + G_{\mathrm{o}}\mathcal{L}_{\mathrm{eq}}(0)| \tag{4.21}$$

$$\textit{Gain bandwidth condition:} \quad \left| e^{\frac{1}{2}g_{\mathrm{B0}}I_{\mathrm{P}}L\,\mathcal{L}_{\mathrm{B}}(\pm\mu)} \right| = |1 + G_{\mathrm{o}}\mathcal{L}_{\mathrm{eq}}(\pm\mu)| \tag{4.22}$$

that lead to

$$G_{\mathrm{o}} = e^{\frac{1}{2}g_{\mathrm{B0}}I_{\mathrm{p}}L} - 1 \tag{4.23}$$

$$\mu = \frac{\Delta\Omega_{\mathrm{B}}}{2}\sqrt{\frac{g_{\mathrm{B0}}I_{\mathrm{p}}L}{\ln\left[\frac{1}{2}\left(e^{g_{\mathrm{B0}}I_{\mathrm{p}}L}+1\right)\right]} - 1}\,. \tag{4.24}$$

Note that unlike Brillouin scattering that has a peak gain and bandwidth independent of the pump intensity I_{p}, frequency-selective Brillouin amplification has a pump dependent peak gain and bandwidth.

4.3.4 Time-Domain Equations for Brillouin Amplification

We now have all the elements needed to perform the inverse Fourier transform that will give the us the equations ruling the field dynamics in the time domain. Let us first rewrite the output signal as

$$\mathcal{E}_{\mathrm{s}}^{\mathrm{out}}(t) = \mathcal{E}_{\mathrm{s}}^{\mathrm{amp}}(t) + \mathcal{E}_{\mathrm{s}}^{\mathrm{in}}(t-T) \tag{4.25}$$

where $\mathcal{E}_{\mathrm{s}}^{\mathrm{amp}}(t)$ is the amplified portion of the output signal. Then, we can use Eqs. (4.18) and (4.20) to express the Fourier transform of this amplified portion as

$$\tilde{\mathcal{E}}_{\mathrm{s}}^{\mathrm{amp}}(\Omega) = \tilde{\mathcal{E}}_{\mathrm{s}}^{\mathrm{out}}(\Omega) - \tilde{\mathcal{E}}_{\mathrm{s}}^{\mathrm{in}}(\Omega)e^{-i\Omega T} = G_{\mathrm{o}}\frac{\mu}{\mu + i\Omega}\,\tilde{\mathcal{E}}_{\mathrm{s}}^{\mathrm{in}}(\Omega)e^{-i\Omega T}\,. \tag{4.26}$$

After multiplying both sides of this equation by $\mu + i\Omega$, we can perform an inverse Fourier transform and finally obtain the desired equation

$$\dot{\mathcal{E}}_{\mathrm{s}}^{\mathrm{amp}}(t) = -\mu\mathcal{E}_{\mathrm{s}}^{\mathrm{amp}}(t) + \mu G_{\mathrm{o}}\,\mathcal{E}_{\mathrm{s}}^{\mathrm{in}}(t - T) \tag{4.27}$$

where the overdot stands for time derivative. Equation (4.27) rules the frequency-selective amplification in the time domain, and the output signal $\mathcal{E}_{\mathrm{s}}^{\mathrm{out}}(t)$ is recovered via Eq. (4.25). It is interesting to note that we have mapped the partial differential Eq. (4.9) into a time-delayed equation, while adding the narrowband filtering property of the amplifier.

It is interesting to note that: *(i)* We do not need to add a detuning σ; *(ii)* We adopt an input-output convention such that the excitation term is not multiplied by i; *(iii)* By definition, the initial condition for $\mathcal{E}_{\mathrm{s}}^{\mathrm{amp}}$ is 0, which corresponds to $\mathcal{E}_{\mathrm{s}}^{\mathrm{amp}}(0) = 0$.

4.4 Model

4.4.1 Phase Modulation

The signal laser emits a monochromatic wave, that can be written as

$$\mathcal{E}_{\mathrm{L}} = \sqrt{P_0}\,, \tag{4.28}$$

where P_0 is the optical power of this continuous-wave laser (i.e., $\mathcal{E}_\mathrm{L}$ is in units of $\sqrt{\mathrm{W}}$). We assume that this PM has an RF modulation signal $V(t)$, so that its output optical field is

$$\mathcal{E}_\mathrm{PM}(t) = \mathcal{E}_\mathrm{L} \exp\left\{ i\pi \frac{V(t)}{V_{\pi_p}} \right\} = \sqrt{P_0} \exp\left\{ i\pi \frac{|\mathcal{V}(t)|}{V_{\pi_p}} \cos[\Omega_0 t + \psi(t)] \right\}. \tag{4.29}$$

Using Jacobi-Anger expansion given in Eq. (2.9), we have the expansion

$$\mathcal{E}_\mathrm{PM}(t) = \sqrt{P_0}\, \mathcal{E}(t) = \sqrt{P_0} \sum_{n=-\infty}^{+\infty} \mathcal{E}_n(t) e^{in\Omega_0 t}. \tag{4.30}$$

with the modal fields

$$\mathcal{E}_n(t) = i^n \mathrm{J}_n \left[\pi \frac{|\mathcal{V}(t)|}{V_{\pi_p}} \right] e^{in\psi(t)}. \tag{4.31}$$

Note that the complex envelope field $\mathcal{E}$ and its modal components $\mathcal{E}_n$ are *dimensionless*.

The first sidemode $\mathcal{E}_1(t)$ is now injected into the Brillouin amplifier. Following the analysis led in the preceding section, the amplified portion of the signal in the fiber obeys the equation

$$\dot{\mathcal{B}}(t) = -\mu \mathcal{B}(t) + \mu G_\mathrm{o} \mathcal{E}_1(t - T) \tag{4.32}$$

with initial condition $\mathcal{B}(0) = 0$ [also note that $\mathcal{B}(t)$ is a dimensionless variable]. The total output optical field after Brillouin amplification is now

$$\mathcal{F}(t) = \sum_{n=-\infty}^{+\infty} \mathcal{F}_n(t) e^{in\Omega_0 t}, \tag{4.33}$$

with $\mathcal{F}_n(t)$ being defined as

$$\mathcal{F}_n(t) = \mathcal{E}_n(t-T) + \delta(n-1)\mathcal{B}(t) \equiv \begin{cases} \mathcal{E}_1(t-T) + \mathcal{B}(t) & \text{for } n = 1 \\ \mathcal{E}_n(t-T) & \text{otherwise} \end{cases}, \tag{4.34}$$

where $\delta(x)$ is the Kronecker function (equal to 1 for $x = 0$ and to 0 otherwise), while all the modal fields $\mathcal{E}_n(t)$ are defined as in Eq. (4.31).

4.4.2 Accounting for the Brillouin Amplification

Now that we have the equation ruling the Brillouin amplification, we can proceed with calculating the voltage generated by the photodetection of this optical signal, which can be expressed as (in units of V):

$$\begin{aligned} V_{\mathrm{pd}}(t) &= SP_0|\mathcal{F}(t)|^2 = SP_0 \left| \sum_{n=-\infty}^{+\infty} \mathcal{F}_n(t) e^{in\Omega_0 t} \right|^2 \\ &= \frac{1}{2}\mathcal{M}_0(t) + \sum_{k=1}^{+\infty} \left\{ \frac{1}{2}\mathcal{M}_k(t) e^{ik\Omega_0 t} + \text{c.c.} \right\}, \end{aligned}$$

where $\mathrm{c.c.}$ stands for the complex conjugate of the preceding terms, and

$$\mathcal{M}_n(t) = 2SP_0 \sum_m \mathcal{F}_m^*(t)\mathcal{F}_{m+n}(t) \tag{4.35}$$

is the complex slowly-varying envelope corresponding to the microwave spectral component of frequency $n \times \Omega_0$ (in volts), while S stands for the PD sensitivity (in units of V/W). This photodetected signal is then bandpass filtered, so that it rejects the DC component $\mathcal{M}_0$ and the harmonics $\mathcal{M}_k$ with $k \geq 2$. Hence, only the spectral component at frequency Ω_0 is allowed to pass through (note that this filter is *not* narrow, so that it does not specifically induce dynamical effects other than fundamental mode selection). The slowly-varying amplitude of the voltage at the output of the PD is therefore $\mathcal{M}_1(t)$ (still in units of V). This signal is then amplified in the electrical branch with a gain G_e (dimensionless). We can also account for all the loop losses through a single loss coefficient κ (dimensionless). Therefore, the slowly-varying envelope $\mathcal{V}(t)$ of the microwave signal fed back to the RF input of the PM is

$$\mathcal{V}(t) = \kappa G_\mathrm{e} e^{i\Phi} \mathcal{M}_1(t) = 2\kappa G_\mathrm{e} S P_0 e^{i\Phi} \sum_{n=-\infty}^{+\infty} \mathcal{F}_n^*(t)\mathcal{F}_{n+1}(t)\,, \tag{4.36}$$

where the phase factor $e^{i\Phi}$ accounts for the effect of the microwave round-trip phase shift Φ. If necessary, this phase be tuned to any desired value (modulo 2π) using a RF phase shifter.

We now need to put all these elements together in order to obtain our final model. Let us introduce the dimensionless microwave envelope

$$\mathcal{A}(t) = \frac{\pi}{V_{\pi_p}} \mathcal{V}(t)\,. \tag{4.37}$$

and the optoelectronic gain as

$$\beta = \frac{\pi \kappa G_\mathrm{e} S P_0}{V_{\pi_p}}\,. \tag{4.38}$$

Note that β is *not* a loop-gain parameter as it is the case for conventional fiber-based OEOs, since it explicitly excludes the Brillouin amplification.

We therefore have the following four-step model for our tunable OEO based on Brillouin amplification:

$$\mathcal{E}_n(t) = i^n \, \mathrm{Jc}_n[|\mathcal{A}(t)|]\mathcal{A}^n(t) \tag{4.39}$$

$$\dot{\mathcal{B}}(t) = -\mu\mathcal{B}(t) + \mu G_{\mathrm{o}}\mathcal{E}_1(t-T) \tag{4.40}$$

$$\mathcal{F}_n(t) = \mathcal{E}_n(t-T) + \delta(n-1)\mathcal{B}(t) \tag{4.41}$$

$$\mathcal{A}(t) = 2\beta e^{i\Phi} \sum_{n=-\infty}^{+\infty} \mathcal{F}_n^*(t)\mathcal{F}_{n+1}(t) \tag{4.42}$$

where

$$\mathrm{Jc}_n(x) = \frac{\mathrm{J}_n(x)}{x^n} \ \text{ with } \ x \in \mathbb{R} \ \text{ and } \ n \in \mathbb{Z}\,, \tag{4.43}$$

is the Bessel-cardinal function of order n.

Note that the gain of this OEO can be tuned in this system following two different ways: either via the optical gain G_{o} (controlled by the power of the pump laser), or via the optoelectronic gain β (controlled via the gain G_{e} of the RF amplifier of the electronic branch). In this study, we will consider without loss of generality that the optical gain G_{o} is fixed, while the optoelectronic gain β is tunable via G_{e}.

4.4.3 Envelope Equation for the Generic Case $T \neq 0$

The four-step model presented in the preceding subsection can be simplified. We have indeed

$$\mathcal{A}(t) = 2\beta e^{i\Phi} \sum_{n=-\infty}^{+\infty} \mathcal{F}_n^*(t)\mathcal{F}_{n+1}(t) \tag{4.44}$$

$$= 2\beta e^{i\Phi}\Big\{\mathcal{B}(t)\mathrm{J}_0[|\mathcal{A}(t-T)|] - \mathcal{B}^*(t)\mathrm{Jc}_2[|\mathcal{A}(t-T)|]\mathcal{A}^2(t-T)\Big\} \tag{4.45}$$

$$+ 2i\beta e^{i\Phi} e^{i\psi(t-T)} \sum_{n=-\infty}^{+\infty} \mathrm{J}_n[|\mathcal{A}(t-T)|]\mathrm{J}_{n+1}[|\mathcal{A}(t-T)|]\,, \tag{4.46}$$

but however, Bessel functions of the first kind obeys

$$\sum_{n=-\infty}^{+\infty} \mathrm{J}_n(x)\mathrm{J}_{n+m}(x) \equiv 0 \tag{4.47}$$

for all $x \in \mathbb{R}$ and all $m \in \mathbb{Z}$. Knowing that $\mathcal{E}_1 = i\,\mathrm{Jc}_1[|\mathcal{A}|]\mathcal{A}$, we can now rewrite the four-step model under the simpler form

$$\dot{\mathcal{B}}(t) = -\mu\mathcal{B}(t) + i\mu G_o \mathrm{Jc}_1[|\mathcal{A}_T|]\mathcal{A}_T \tag{4.48}$$

$$\mathcal{A}(t) = 2\beta e^{i\Phi}\Big\{\mathcal{B}(t)\mathrm{J}_0[|\mathcal{A}_T|] - \mathcal{B}^*\mathrm{Jc}_2[|\mathcal{A}_T|]\mathcal{A}_T^2\Big\} \tag{4.49}$$

where we omit the time-domain expressions of the envelopes for simplicity, such as $\mathcal{A}(t) \to \mathcal{A}$. Equation (4.49) can be furthermore simplified. Indeed, an analysis of the above equations shows that the phases $\psi(t)$ and $\varphi(t)$ of $\mathcal{A}$ and $\mathcal{B}$ are such that

$$\varphi(t) = \frac{\pi}{2} + \psi(t-T) \quad \text{and} \quad \psi(t) = \Phi + \varphi(t) \tag{4.50}$$

which leads to the solution

$$\Phi = -\frac{\pi}{2} \quad \text{and} \quad \psi(t) = \varphi(t) - \frac{\pi}{2} = \text{Constant}\,. \tag{4.51}$$

Note that a direct consequence of this solution is that we now have $e^{i\Phi} = -i$, so that a phase shifter has to be introduced in the loop to implement this phase condition. A phase rotation therefore allows to obtain

$$\mathcal{A} = -2i\beta\mathcal{B}\Big\{\mathrm{J}_0[|\mathcal{A}_T|] + \mathrm{J}_2[|\mathcal{A}_T|]\Big\} = -4i\beta\mathcal{B}\,\mathrm{Jc}_1[|\mathcal{A}_T|]\,, \tag{4.52}$$

where we have used the recurrence relationship

$$\mathrm{J}_{n-1}(x) + \mathrm{J}_{n+1}(x) = \frac{2n\mathrm{J}_n(x)}{x}\,. \tag{4.53}$$

Note that Eq. (4.52) preserves the phase relationship of Eq. (4.51).

Let us now rewrite Eq. (4.52) and Eq. (4.48) as

$$\mathcal{B} = -\frac{\mathcal{A}}{4i\beta\,\mathrm{Jc}_1[|\mathcal{A}_T|]} \tag{4.54}$$

$$\dot{\mathcal{B}} = \frac{\mu\mathcal{A}}{4i\beta\,\mathrm{Jc}_1[|\mathcal{A}_T|]} + i\mu G_{\mathrm{o}}\,\mathrm{Jc}_1[|\mathcal{A}_T|]\mathcal{A}_T \tag{4.55}$$

meaning that both $\mathcal{B}$ and $\dot{\mathcal{B}}$ are expressed completely as a function of $\mathcal{A}$ and $\mathcal{A}_T$.

We can now determine $\dot{\mathcal{A}}$ as

$$\dot{\mathcal{A}} = \frac{\partial \mathcal{A}}{\partial \mathcal{B}} \frac{\partial \mathcal{B}}{\partial t} + \frac{\partial \mathcal{A}}{\partial |\mathcal{A}_T|} \frac{\partial |\mathcal{A}_T|}{\partial t} = \frac{\partial \mathcal{A}}{\partial \mathcal{B}} \dot{\mathcal{B}} + \frac{\partial \mathcal{A}}{\partial |\mathcal{A}_T|} \partial_t |\mathcal{A}_T| \,, \tag{4.56}$$

where

$$\partial_t |\mathcal{A}_T| = \partial_t [\mathcal{A}_T \mathcal{A}_T^*]^{\frac{1}{2}} = \frac{\dot{\mathcal{A}}_T \mathcal{A}_T^* + \mathcal{A}_T \dot{\mathcal{A}}_T^*}{2|\mathcal{A}_T|} \,. \tag{4.57}$$

is the derivative of $|\mathcal{A}_T|$ with regard to time. It is important to note that $\partial_t|\mathcal{A}_T| \neq |\partial_t \mathcal{A}_T| = [\dot{\mathcal{A}}_T \dot{\mathcal{A}}_T^*]^{\frac{1}{2}}$. From Eq. (4.52), we obtain

$$\frac{\partial \mathcal{A}}{\partial \mathcal{B}} = -4i\beta \, \mathrm{Jc}_1[|\mathcal{A}_T|] \tag{4.58}$$

$$\frac{\partial \mathcal{A}}{\partial |\mathcal{A}_T|} = -4i\beta \mathcal{B} \mathrm{Jc}_1'[|\mathcal{A}_T|] \,. \tag{4.59}$$

We now use the results from Eqs. (4.55), (4.54), (4.58), and (4.59) to rewrite Eq. (4.56) as

$$\begin{aligned} \dot{\mathcal{A}} = &-4i\beta \, \mathrm{Jc}_1[|\mathcal{A}_T|] \left\{ \frac{\mu \mathcal{A}}{4i\beta \, \mathrm{Jc}_1[|\mathcal{A}_T|]} + i\mu G_{\mathrm{o}} \, \mathrm{Jc}_1[|\mathcal{A}_T|] \mathcal{A}_T \right\} \\ &- 4i\beta \mathrm{Jc}_1'[|\mathcal{A}_T|] \, \partial_t |\mathcal{A}_T| \left\{ -\frac{\mathcal{A}}{4i\beta \, \mathrm{Jc}_1[|\mathcal{A}_T|]} \right\}, \end{aligned} \tag{4.60}$$

and using $\mathrm{Jc}_1'(x) = -\mathrm{J}_2(x)/x$, this can be finally be written as

$$\dot{\mathcal{A}} = -\mu \mathcal{A} + 4\mu\gamma \, \mathrm{Jc}_1^2[|\mathcal{A}_T|] \mathcal{A}_T - \left\{ \frac{\mathrm{J}_2[|\mathcal{A}_T|]}{\mathrm{J}_1[|\mathcal{A}_T|]} \partial_t |\mathcal{A}_T| \right\} \mathcal{A} \tag{4.61}$$

with $\gamma = \beta G_{\rm o}$ being the loop gain.

Equation (4.61) is well-defined, and in particular, the time-delayed terms in the brackets in the right-hand side are well-defined at any time. The term $\partial_t|\mathcal{A}_T|$ is indeed unusual, but is not problematic from the mathematical viewpoint because at any time t, the variable $\mathcal{A}_T$ and any variable that univocally depends on it can be determined unambiguously, even at the numerical level. One can also note that in the steady state, we have $\dot{\mathcal{A}} = 0$, $\partial_t|\mathcal{A}_T| = 0$. Note that unlike the conventional envelope equations for OEOs, Eq. (4.61) involves coupling between the delayed and non-delayed variables. Also note that the phase dynamics is irrelevant in the deterministic case, and can be disregarded but will become key at the time to investigate the noise performance of the system [35, 89–92].

4.4.4 Envelope Equation for the Practical Case $T = 0$

Using Eq. (4.61), we can obtain an envelope equation for the case $T = 0$, which corresponds to the physical configuration where the system is chipscale. We first note that the phase ψ of the microwave envelope $\mathcal{A}$ is a constant of motion [see Eq. (4.51)]. It results that $[\partial_t|\mathcal{A}|]\,\mathcal{A} = \dot{\mathcal{A}}|\mathcal{A}|$ and consequently, Eq. (4.61) can be written as

$$\dot{\mathcal{A}} = -\mu\mathcal{A} + 4\mu\gamma\,\mathrm{Jc}_1^2[|\mathcal{A}|]\mathcal{A} - \left\{\frac{\mathrm{J}_2[|\mathcal{A}|]}{\mathrm{J}_1[|\mathcal{A}|]}\,|\mathcal{A}|\right\}\dot{\mathcal{A}}\,, \tag{4.62}$$

from which we directly obtain

$$\dot{\mathcal{A}} = -\mu\mathcal{A}\,\frac{1 - 4\gamma\,\mathrm{Jc}_1^2[|\mathcal{A}|]}{1 + \mathrm{J}_2[|\mathcal{A}|]/\mathrm{Jc}_1[|\mathcal{A}|]}\,. \tag{4.63}$$

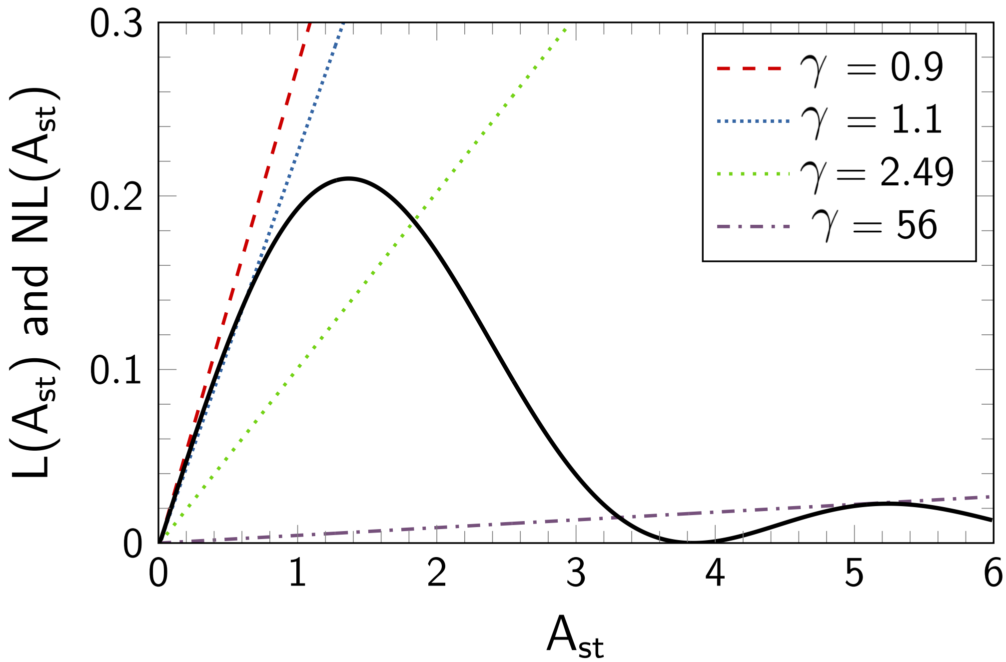

Figure 4.3: The graphical representation of (4.65) where $\mathrm{L}(A_{\rm st}) = A_{\rm st}/4\gamma$ and $\mathrm{NL}(A_{\rm st}) = \mathrm{J}_1^2[A_{\rm st}]/A_{\rm st}$ are expressed as discontinuous colored and continuous black lines respectively.

This equation is the one that has to be considered to track the temporal dynamics of the microwave envelope in the case where $T = 0$.

4.5 Stationary States and Their Stability for $T = 0$

We already know that the phase of $\mathcal{A}$ is an arbitrary constant, which can be set without loss of generality to zero. In that case, $\mathcal{A}$ becomes real-valued and we can remove the calligraphic fonts following $\mathcal{A} \equiv A \geq 0$, so that the amplitude equation reads

$$\dot{A} = -\mu A \, \frac{1 - 4\gamma \, \mathrm{Jc}_1^2[A]}{1 + \mathrm{J}_2[A]/\mathrm{Jc}_1[A]} \,. \tag{4.64}$$

The stationary state of Eq. (4.64) can be obtained as

$$\frac{A_{\mathrm{st}}}{4\gamma} = \frac{\mathrm{J}_1^2[A_{\mathrm{st}}]}{A_{\mathrm{st}}}\,. \tag{4.65}$$

and two possible solutions are

$$A_{\mathrm{st}} = \begin{cases} A_{\mathrm{tr}} = 0 \\ A_{\mathrm{osc}} = \mathrm{Jc}_1^{-1}\left[\pm\dfrac{1}{2\sqrt{\gamma}}\right] \end{cases} \tag{4.66}$$

where $A_{\mathrm{tr}} = 0$ is the trivial solution, $A_{\mathrm{osc}} \neq 0$ is the oscillatory (nontrivial) solution, and Jc_1^{-1} is the inverse function of Jc_1 (whenever single-valued). The above solutions are valid regardless of there is a time-delay or not. Equations (4.65) and (4.66) are graphically shown in Fig. 4.3. The trivial solution exists for the all gains while the oscillatory solution is valid for $\gamma > 1$.

Equation (4.66) shows two possible oscillatory solutions, but we can reduce to one by confirming the limit of the Bessel-Cardinal function. The function oscillates between $-0.066 < \mathrm{Jc}_1(x) < 0.5$. If we consider γ is a positive value, the two solutions should cover the positive and negative range separately, and thus

$$\mathrm{Jc}_1[A_{\mathrm{osc}}] = \begin{cases} +\dfrac{1}{2\sqrt{\gamma}} & \text{for} \qquad 0 < \mathrm{Jc}_1[A_{\mathrm{osc}}] < 0.5 \\ -\dfrac{1}{2\sqrt{\gamma}} & \text{for} \quad -0.066 < \mathrm{Jc}_1[A_{\mathrm{osc}}] < 0 \end{cases} \tag{4.67}$$

The only requirement for the validity of the positive solution is $\gamma > 1$ while the negative solution needs $\gamma > 56.0$ practically very difficult to achieve. We can only consider the positive solution, and therefore, the oscillatory solution $A_{\rm osc}$ we will consider is

$$A_{\rm osc} = \mathrm{Jc}_1^{-1}\left[\frac{1}{2\sqrt{\gamma}}\right] \;\; \text{where} \;\; 1 < \gamma < 56.0. \tag{4.68}$$

Now, we need to determine the stability of the two solutions. However, since the upper limit $\gamma \simeq 56$ is already far beyond physically achievable, we are going to restrict our analysis to the range $0 \leq \gamma < 56$ for the gain values.

4.5.1 Stability of the Trivial Solution

To evaluate the stability of the trivial solution $A_{\rm tr} = 0$, we can perturb the fixed point and check if it decays or grows by depending on the loop gain γ. Considering a very small perturbation δA around the fixed point, thereby applying $A \to A_{\rm tr} + \delta\mathcal{A}$, leads Eq. (4.64) to be written as

$$\delta\dot{\mathcal{A}} = -\mu(1-\gamma)\,\delta\mathcal{A} \tag{4.69}$$

where higher order nonlinear terms are neglected. It is trivial to show that $\delta\mathcal{A}$ decays to zero for $\gamma < 1$, while it diverges for $\gamma < 1$. Therefore, feedback gain $\gamma_{\rm th} \equiv 1$ defines the threshold below which the trivial fixed point $A_{\rm tr} = 0$ remains stable (no oscillations), and above which microwave oscillations are triggered (microwave oscillation of frequency Ω_0 and constant amplitude). It can be shown that this bifurcation corresponds to a Hopf bifurcation for the microwave signal, and a pitchfork bifurcation for its amplitude [3, 32–34].

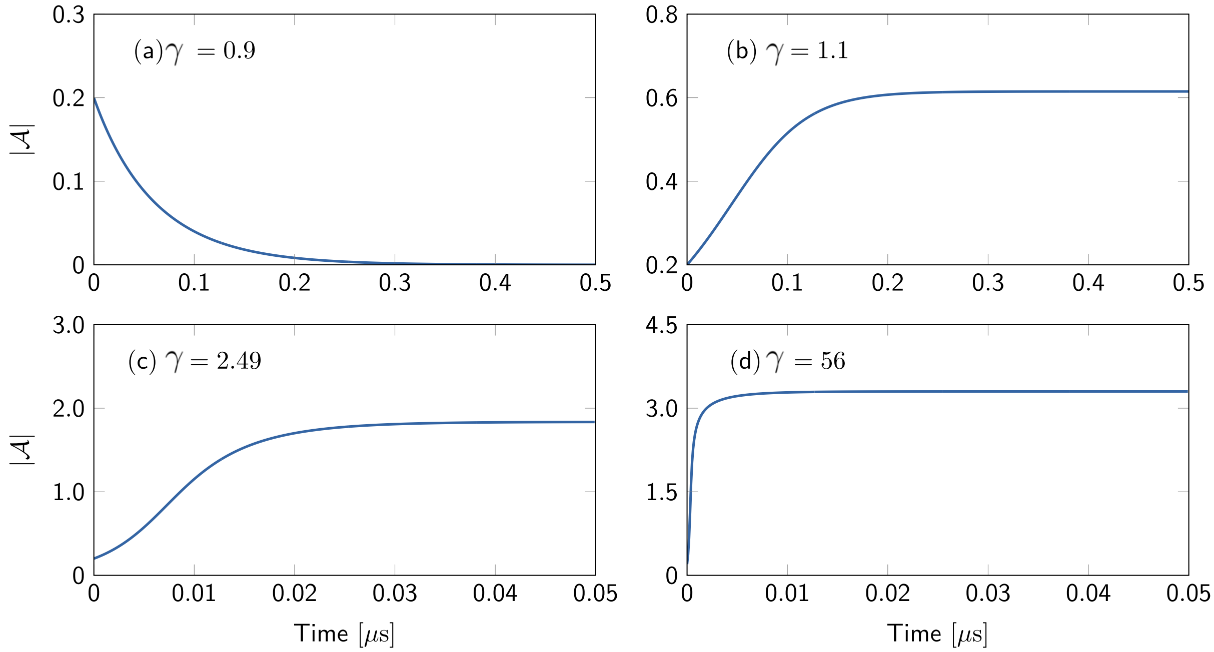

Figure 4.4: Numerical simulation of the SBS-based OEO with null delay [Equation (4.63)] for various values of the gain γ. The value of the Brillouin gain bandwidth is set to $\mu = 2\pi \times 25$ MHz.

4.5.2 Stability of the Oscillatory Solution

We now perturb the oscillating solution A_{osc} (which only exists for $\gamma > 1$), so that the linearized counterpart of Eq. (4.64) can be written as

$$\delta\dot{\mathcal{A}} = -\mu\gamma R_1 \delta\mathcal{A} \tag{4.70}$$

where we define

$$R_1 = \frac{8\mathrm{Jc}_1[A_{\text{osc}}]\mathrm{J}_2[A_{\text{osc}}]}{1 + \mathrm{J}_2[A_{\text{osc}}]/\mathrm{Jc}_1[A_{\text{osc}}]}\,. \tag{4.71}$$

Since the constant coefficient R_1 of is always positive, it appears that we always have $\delta A \to 0$ for $1 < \gamma < 56$, so that the oscillatory solution A_{osc} is always stable for that range of gain values.

4.5.3 Numerical Simulation for the Case $T = 0$

Figures 4.4(a) and (b) display the transient dynamics of the SBS-based OEO with null delay for $\gamma = 0.9$ and $\gamma = 1.1$, that is, just below and above the threshold value $\gamma_{\rm th} = 1$. On the other hand, Figs. 4.4(c) and (d) show the dynamics of the oscillator at $\gamma = 2.49$ and $\gamma = 56$, thereby showing that oscillating solution is indeed stable in the gain range of interest in for that solution ($1 < \gamma < 56$). The amplitudes of the oscillating solutions also correspond to the intersections points in Fig. 4.3.

4.6 Stationary States and Their Stability for $T \neq 0$

We now consider the generic case where the delay is not null. Here also we can take advantage of the fact that that the phase ψ of the microwave is a constant. Once again it is convenient to arbitrarily set $\psi = 0$, so that the envelope $\mathcal{A}$ becomes real-valued, with $\mathcal{A} \equiv A > 0$ and $\mathcal{A}_T \equiv A_T > 0$. The microwave dynamics is now ruled by

$$\dot{A} = -\mu A + 4\mu\gamma \, \mathrm{Jc}_1^2[A_T] A_T - \frac{\mathrm{J}_2[A_T]}{\mathrm{J}_1[A_T]} \, A \dot{A}_T \, , \tag{4.72}$$

It first appears that the stationary states of Eq. (4.72) are exactly the same as those obtained for the case $T = 0$. We have trivial and oscillatory solutions given by Eq. (4.66), and the restriction discussed in Eq. (4.68) also apply in the present case. We can determine the stability of the two solutions in the same way as $T = 0$ case.

4.6.1 Stability of the Trivial Solution

When we perturb the trivial solution with $\delta\mathcal{A} = \delta A_0 \exp[(\lambda_{\rm tr} + i\xi_{\rm tr})t]$, Eq. (4.72) can be written as

$$\delta\dot{\mathcal{A}} \simeq -\mu\delta\mathcal{A} + \mu\gamma\delta A_T \tag{4.73}$$

From the eigenvalue expression, the coefficients $\lambda_{\rm tr}$ and the $\xi_{\rm tr}$ will obey

$$\lambda_{\rm tr} = -\mu + \mu\gamma e^{-\lambda_{\rm tr}T}\cos\xi_{\rm tr}T \tag{4.74}$$

$$\xi_{\rm tr} = -\mu\gamma e^{-\lambda_{\rm tr}T}\sin\xi_{\rm tr}T \tag{4.75}$$

We can only consider near $\lambda_{\rm tr} = 0$ where the sign change of the $\lambda_{\rm tr}$ occurs. Equation (4.75) generates two possible solutions $\xi_{\rm tr} = 0$ and $\xi_{\rm tr} = \pi/T$ but the later one cannot satisfy Eq. (4.74). Therefore, the unique solution is

$$\lambda_{\rm tr} \simeq \frac{\gamma - 1}{T\gamma} \tag{4.76}$$

$$\xi_{\rm tr} = 0 \tag{4.77}$$

where we have assumed the condition $\mu T \gg 1$. This solution generates the same result as for the case $T = 0$, i.e. the trivial solution is stable for $\gamma < \gamma_{\rm th}$ and unstable otherwise.

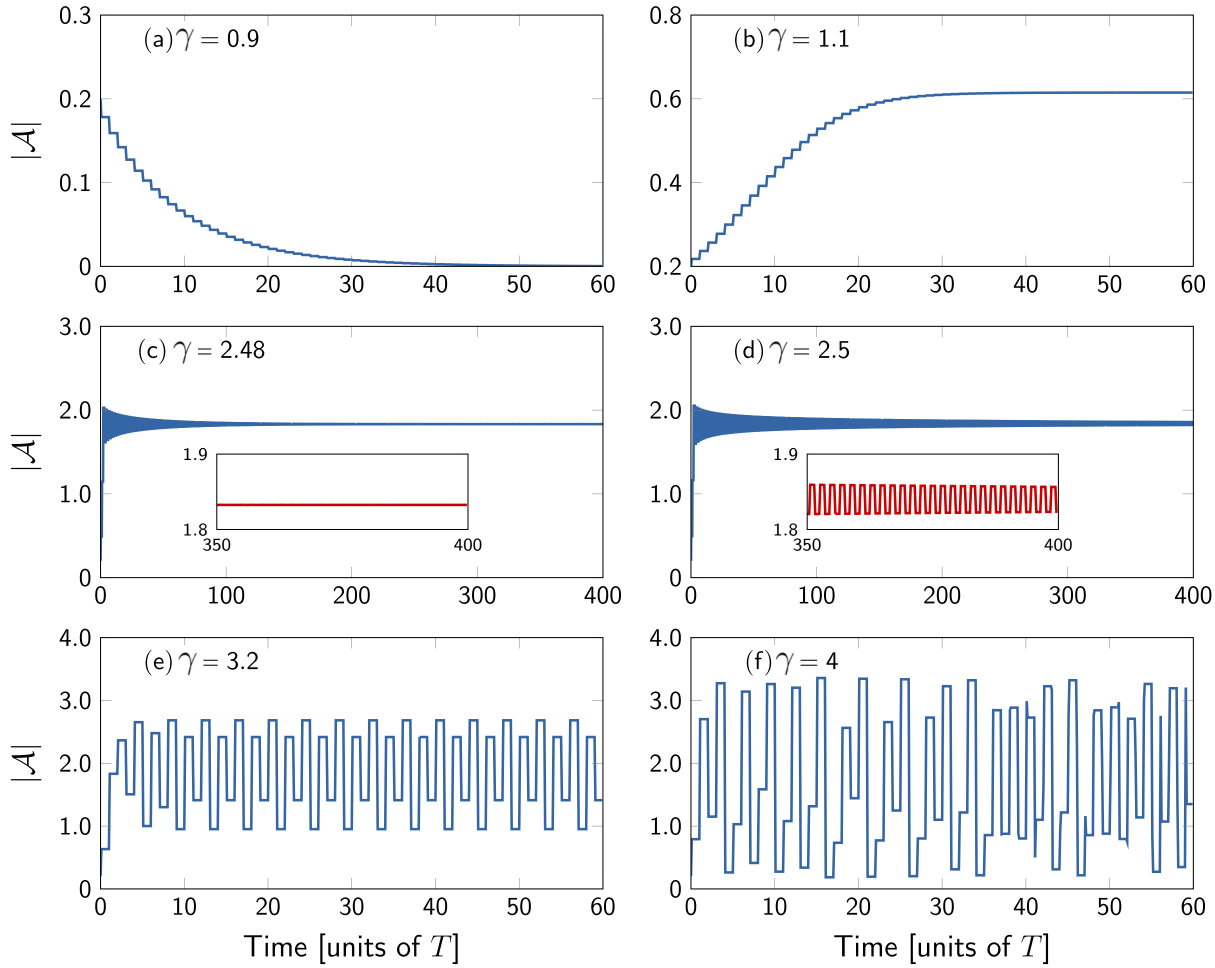

Figure 4.5: Numerical simulation of the SBS-based OEO when $T \neq 0$ [Equation (4.72)] for various values of the gain γ. The insets of (c) and (d) show the asymptotic dynamical behavior of the system, evidencing the qualitative difference induced by the Neimark-Sacker bifurcation at $\gamma_{\rm cr}$ = 2.49. The parameters of the system are $\mu = 2\pi \times 25$ MHz and $T = 5\ \mu$s.

4.6.2 Stability of the Oscillatory solution

When we perturbing the oscillatory solution $A_{\rm osc}$, the linearization of Eq. (4.72) can be yields

$$\delta\dot{\mathcal{A}} = -\mu\delta\mathcal{A} + \mu R_2\, \delta\mathcal{A}_T - R_3\, \delta\dot{\mathcal{A}}_T \tag{4.78}$$

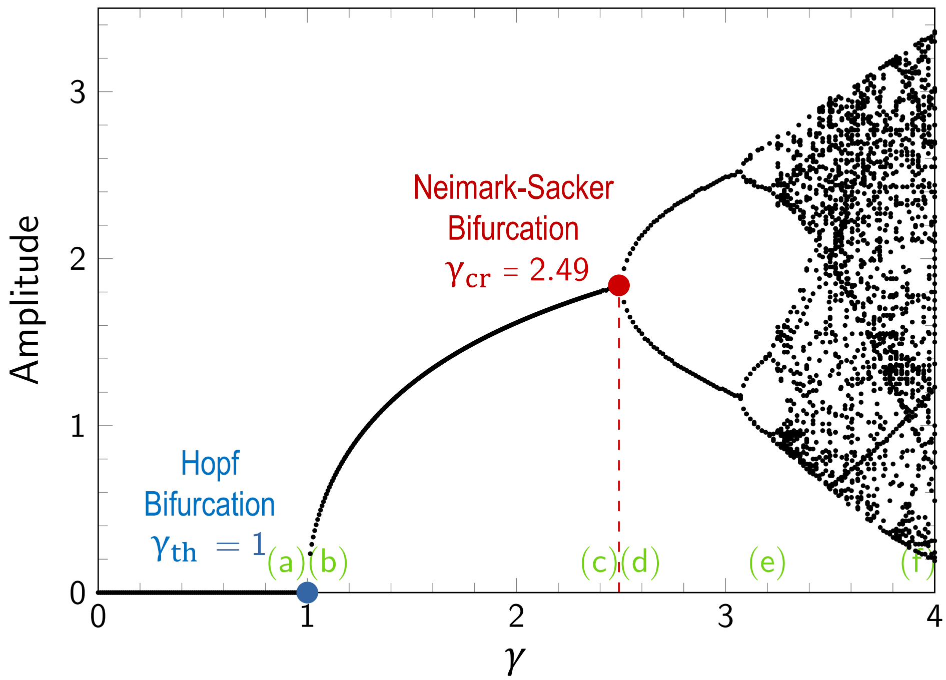

Figure 4.6: Bifurcation diagram for the SBS-based OEO. The labels (a)–(f) indicate the values of the gain γ used for the time-domain simulations in Fig.4.5. The Hopf and Neimark-Sacker bifurcations numerically emerge at the gain values γ_{th} = 1 and γ_{cr} = 2.49 (resp.), as predicted by the theory. The parameters of the system are $\mu = 2\pi \times 25$ MHz and $T = 5\ \mu$s.

where we use a Bessel-Cardinal function property $\mathrm{Jc}_1'(x) = \mathrm{J}_0(x)/x - 2\mathrm{Jc}_1(x)/x$ and define

$$R_2 = 8\gamma \mathrm{Jc}_1[A_{\text{osc}}]\mathrm{J}_0[A_{\text{osc}}] - 3 \ \text{ and } \ R_3 = \mathrm{J}_2[A_{\text{osc}}]/\mathrm{Jc}_1[A_{\text{osc}}] \tag{4.79}$$

If we define $\delta A = \delta A_0 \exp{(\lambda_{\text{osc}} + i\xi_{\text{osc}})t}$, the real part will be ruled by

$$\lambda_{\text{osc}} = \frac{-\mu + \mu R_2 e^{-\lambda_{\text{osc}}T} \cos \xi_{\text{osc}}T - R_3 e^{-\lambda_{\text{osc}}T} \xi_{\text{osc}} \sin \xi_{\text{osc}}T}{1 + R_3 e^{-\lambda_{\text{osc}}T} \cos \xi_{\text{osc}}T} \tag{4.80}$$

and the imaginary part can be written as

$$\xi_{\text{osc}} = \frac{-(\mu R_2 - R_3\lambda_{\text{osc}}) e^{-\lambda_{\text{osc}}T} \sin \xi_{\text{osc}}T}{1 + R_3 e^{-\lambda_{\text{osc}}T} \cos \xi_{\text{osc}}T} \tag{4.81}$$

The two results lead to two possible solutions

$$\lambda_{\text{osc}} \simeq \begin{cases} \dfrac{R_2 - 1}{R_2 T} & \text{if } R_2 > 0 \\ \dfrac{R_2 + 1}{R_2 T} & \text{if } R_2 < 0 \end{cases} \tag{4.82}$$

where we are still assuming $\mu T \gg 1$. Equation (4.82) shows that λ_{osc} is negative for $|R_2| < 1$, and that condition corresponds to the gain range $1 < \gamma < 2.49$. Therefore, if we define $\gamma_{\text{cr}} \equiv 2.49$ as the critical value for which the microwave is destabilized, then the oscillatory solution is stable for $\gamma_{\text{th}} < \gamma < \gamma_{\text{cr}}$.

The secondary bifurcation occurring at $\gamma_{\text{cr}} = 2.49$ is a Neimark-Sacker or *torus* bifurcation [3, 32, 33, 93, 94]. It should be noted that in the case of a short (but non-null) delay with $\mu T \sim 1$, the formalism developed above is not valid anymore and a more involved calculation would be needed to determine γ_{cr}. Please refer to [95].

4.6.3 Numerical Simulation for the Case $T \neq 0$

Figures 4.5(a) and (b) display the transient dynamics of $\gamma = 0.9$ and $\gamma = 1.1$ the just below and above the threshold value γ_{th}. On the other hand, Figs. 4.5(c) and (d) show the dynamics of the oscillator at $\gamma = 2.48$ and $\gamma = 2.5$, that is, just before and just after the torus bifurcation. The amplitude of the output microwave is stable below the critical value (γ_{cr}) and unstable above, as predicted by the bifurcation analysis. When the gain is further increased, the oscillator displays $4T$-periodic behavior [Fig. 4.5(e)] while further increase of γ leads to a chaotic behavior. [Fig. 4.5(f)]. The overall dynamics of the oscillator can be described via a bifurcation diagram as displayed in Fig. 4.6, where the Hopf and Neimark-Sacker bifurcations are shown to occur exactly where they were analytically predicted.

4.7 Conclusion of the Chapter

In this chapter, we have studied the nonlinear dynamics of the SBS-based OEOs. We have first analyzed the SBS effect in the nonlinear fiber acting as a MPF, and we have derived as well an explicit input-output relationship ruling the frequency-selective amplification. The modeling of the SBS process has enabled us to obtain a delay-differential equation for governing the microwave envelope of the OEO output microwave signal. Then, a stationary state analysis was conducted to find and evaluate the stability of the fixed points (trivial and oscillatory solutions), leading to the analytical determination of the threshold gain value triggering the onset of microwave oscillations, as well as the critical value leading to their destabilization. Numerical simulations confirmed the stability analysis.

The proposed setup addresses the proposed concerns raised by the models presented in Chapters 2 and 3. The key idea of this setup lies in achieving microwave photonic filtering through SBS, thereby enabling frequency selection in the optical domain and alleviating the reliance on electronic components. Furthermore, the model offers easy frequency tunability, with the pump frequency serving as the tuning parameter. An additional noteworthy aspect is that the dynamics exhibit strikingly similarities to the previous models, depending on electronic components for frequency selection. Therefore, another significant realization from this section is that OEOs demonstrate consistent dynamical similarities irrespective of the methods employed for frequency selection.

Chapter 5: The Universal Microwave Envelope Equation

5.1 Introduction of the Chapter

Throughout Chapters 2, 3, and 4, we explored the dynamics of the various OEOs by deriving their respective microwave envelope equations. These equations effectively describe the nonlinear behaviors of the systems and offer crucial insights into their magnitude and phase dynamics. Interestingly, based on the obtained results, we could observe noteworthy dynamical similarities among the different OEO setups. Upon comparing the analyses conducted for the basic OEO in Chapter 2 and the SBS-based OEO in Chapter 4, we observed striking similarities in their numerical simulation results and bifurcation diagrams. Notably, the only point of differentiation appears to be the critical gain value. Furthermore, analogies were found between their dynamic equations. In Chapter 3, we demonstrated that the dynamic equations governing the oscillation loops of the frequency-multiplicative models can be described using Eq. (2.19), which represents the envelope equation of the basic OEO proposed in Chapter 2. However, the envelope equation of the SBS-based OEO, Eq. (4.61), is more intricate due to the additional complexities introduced by the microwave photonics filtering. Nevertheless, both equations share common elements, which consist of a damping and a nonlinear pumping term.

Therefore, comparing the envelope equations of the models reveal similarities between the dynamic equations, suggesting that their dynamics can be governed by an envelope equation that can be reformulated under a generalized *universal* form [63]. In this chapter, we introduce the universal equation, which we refer to as the universal microwave envelope equation, and conduct analytical investigations. Furthermore, we perform stability analysis of the universal equation and suggest models that can be used to find solutions and assess their stablilities. We also provide a description of the envelope dynamics of the frequency-multiplied output in a universal form. This chapter consists of the following sections: In Section 5.2, we present the universal microwave envelope equation and perform stability analysis. We also apply the universal models to the basic OEO and the SBS-based OEO to verify their validity. In Section 5.3, the universal equation for the frequency-multiplied output is presented. Finally, the chapter is summarized in Chapter 5.4.

5.2 The Universal Microwave Envelope Equation

Comparing the envelope equations presented in the preceding chapters, we can express the universal microwave envelope equation in terms of a damping and nonlinear pumping terms, as follows:

$$\dot{\mathcal{A}} = -\mu e^{i\vartheta}\mathcal{A} - \mu\gamma e^{i\vartheta} e^{-i\sigma} f_{\text{NL}}[\mathcal{A}, \mathcal{A}_T, \dot{\mathcal{A}}_T] \tag{5.1}$$

where $f_{\text{NL}}[\mathcal{A}, \mathcal{A}_T, \dot{\mathcal{A}}_T]$ is an arbitrary nonlinear function fulfilling the following condition $f_{\text{NL}}[0, 0, 0] = 0$. Chapter 3 demonstrated that the nonlinear functions of most RF-filtering based OEOs depend on $\mathcal{A}$ and $\mathcal{A}_T$, while Chapter 4 illustrated that the microwave photonic filtering process can give rise to a more complicated form by involving higher-order terms, such as $\dot{\mathcal{A}}_T$.

5.2.1 Stationary States and Their Stabilities

The first task in analyzing the universal equation is stability analysis, akin to what was conducted in Chapters 2 and 4. Please refer to Chapter 2 to see more detailed analysis process. Even though this chapter explains important steps required for stability analysis. In order to find the stationary states of the universal envelope equation, we can set the time-derivative terms as zero, which allows one to express Eq. (5.1) in terms of a stationary solution $\mathcal{A}_{\text{st}} = \mathcal{A} = \mathcal{A}_T$ as follows:

$$\mathcal{A}_{\text{st}} - \gamma e^{-i\sigma} f_{\text{NL}}[\mathcal{A}_{\text{st}}, \mathcal{A}_{\text{st}}, 0] = 0. \tag{5.2}$$

We approximate $\vartheta = 0$ as this parameter is naturally very small and has minimal effect on the amplitude dynamics. Here, we utilize two phase matching conditions. First, as shown in Eq. (5.2), we require $\sigma = \pm\pi$ and this fact can generate two solution sets. However, since the nonlinear function given in Eq. (5.1) should have a proper pumping term, we select a specific solution set $\sigma = \pi \mathrm{mod}[2\pi]$ and $\gamma > 0$. Secondly, if we plug the aforementioned conditions back into Eq. (5.1), it can be found that we need to have the following condition $\psi(t) = \psi(t-T)$ due to a phase-matching requirement. This implies that the phase terms can be canceled out on both sides of Eq. (5.1), allowing us to rewrite the universal equation solely in terms of the magnitude, as follows:

$$\dot{A} = -\mu A + \mu\gamma f_{\text{NL}}[A, A_T, \dot{A}_T] \tag{5.3}$$

where the calligraphic fonts out represent they are real-valued now. We already used the above mentioned analyses in Chapter 2.

From Eq. (5.2), we find two solutions for $\mathcal{A}_{\text{tr}}$: a trivial solution $A_{\text{tr}} = 0$ and an oscillatory solution satisfying $A_{\text{osc}} = \gamma f_{\text{NL}}[A_{\text{osc}}, A_{\text{osc}}, 0]$. We first analyze the stability of the trivial solution by directly replacing $A \to A_{\text{st}} + \delta\mathcal{A}$, where the small perturbation is complex-valued and defined as $\delta\mathcal{A} = \delta\mathcal{A}_0 e^{(\lambda_{\text{st}} + i\xi_{\text{st}})t}$. Then, we could observe whether the real part of the perturbation grows or decays depending the loop gain in order to asses stability. Considering the small perturbation expression, Eq. (5.3) can be rewritten as:

$$\delta\dot{\mathcal{A}} = -\mu\delta\mathcal{A} - \mu A_{\text{st}} + \mu\gamma f_{\text{NL}}[A_{\text{st}} + \delta\mathcal{A}, A_{\text{st}} + \delta\mathcal{A}_T, \delta\dot{\mathcal{A}}_T]. \tag{5.4}$$

In the next, we apply a Taylor expansion to the nonlinear function, which leads the nonlinear function to be expanded as follows:

$$\begin{aligned} &f_{\text{NL}}[A_{\text{st}} + \delta\mathcal{A}, A_{\text{st}} + \delta\mathcal{A}_T, \delta\dot{\mathcal{A}}_T] \simeq f_{\text{NL}}[A_{\text{st}}, A_{\text{st}}, 0] + \\ &\left[\delta\mathcal{A}\frac{\partial}{\partial A} + \delta\mathcal{A}_T\frac{\partial}{\partial A_T} + \delta\dot{\mathcal{A}}_T\frac{\partial}{\partial \dot{A}_T}\right] f_{\text{NL}}[A, A_T, 0]\bigg|_{A, A_T = A_{\text{st}}} \end{aligned} \tag{5.5}$$

where we consider up to the first-ordered terms. By applying Eq. (5.5) into Eq. (5.4), we can express the perturbation equation as

$$\delta\dot{\mathcal{A}} = -\mu\delta\mathcal{A} + \mu\gamma\left[\delta\mathcal{A}\frac{\partial f}{\partial A} + \delta\mathcal{A}_T\frac{\partial f}{\partial A_T} + \delta\dot{\mathcal{A}}_T\frac{\partial f}{\partial \dot{A}_T}\right] \tag{5.6}$$

where each partial differential term is evaluated at $A = A_T = A_{\text{st}}$, and we denote $f \equiv f_{\text{NL}}[A, A_T, 0]$

for notational simplicity. This means, for example, that the first differential term is equivalent to:

$$\delta\mathcal{A}\frac{\partial f}{\partial A} = \delta\mathcal{A}\frac{\partial}{\partial A} f_{\text{NL}}[A, A_T, 0]\bigg|_{A,A_T=A_{\text{st}}}. \tag{5.7}$$

In Eq. (5.6), the terms $-\mu A_{\text{st}}$ and $f_{\text{NL}}[A_{\text{st}}, A_{\text{st}}, 0]$ are removed, as they are both zero in the case of the trivial solution and cancel each other out in the case of the oscillatory solution. Now, we look into the two solution cases separately using the eigenvalue expression. A given solution will be stable if $\lambda_{\text{st}} < 0$, as instability decays exponentially, and unstable if $\lambda_{\text{st}} > 0$, as instability grows exponentially on the other hand.

5.2.1.1 Stability Analysis of the Imaginary Part

By plugging the expression of the eigenvalue expression in Eq. (5.6), we can express the imaginary part ξ_{st}, as follows

$$\xi_{\text{st}} = \mu\gamma e^{-\lambda_{\text{st}}T}\left\{\left(\xi_{\text{st}}\cos\xi_{\text{st}}T - \lambda_{\text{st}}\sin\xi_{\text{st}}T\right)\frac{\partial f}{\partial \dot{A}_T} - \sin\xi_{\text{st}}T\frac{\partial f}{\partial A_T}\right\}. \tag{5.8}$$

For the imaginary part analysis, we can simply plug $\lambda_{\text{st}} = 0$ into the above expression, which results in the following expression:

$$\xi_{\text{st}} = \frac{-\mu\gamma\sin\xi_{\text{st}}T\frac{\partial f}{\partial A_T}}{1 - \mu\gamma\cos\xi_{\text{st}}T\frac{\partial f}{\partial \dot{A}_T}}. \tag{5.9}$$

Interestingly, both sides of Eq. (5.9) exhibit a significant scale difference when considering the typical magnitude of μ. Hence, in a sinusoidal cycle, the only possible solutions could be 0 or

π/T, where the choice depends on the evaluation of the real part of the eigenvalue.

5.2.1.2 Stability Analysis of the Real Part

By applying the eigenvalue expression to Eq. (5.6), we can express the real part λ_{st}, as follows

$$\begin{aligned}\lambda_{\text{st}} = &-\mu + \mu\gamma\bigg\{\frac{\partial f}{\partial A} + e^{-\lambda_{\text{st}}T}\cos\xi_{\text{st}}T\frac{\partial f}{\partial A_T}\\ &+ e^{-\lambda_{\text{st}}T}(\lambda_{\text{st}}\cos\xi_{\text{st}}T + \xi_{\text{st}}\sin\xi_{\text{st}}T)\frac{\partial f}{\partial \dot{A}_T}\bigg\}.\end{aligned} \tag{5.10}$$

It is possible to further simplify Eq. (5.10) by using Taylor-expansion on the exponential term, thereby rewriting it as $e^{-\lambda_{\text{tr}}T} \simeq 1 - \lambda_{\text{st}}T$. Next, we can linearize it near $\lambda_{\text{st}} = 0$, which finally generates:

$$\lambda_{\text{st}} = \frac{-\mu + \mu\gamma\big(\frac{\partial f}{\partial A} + \cos\xi_{\text{st}}T\frac{\partial f}{\partial A_T}\big)}{1 + \mu\gamma\cos\xi_{\text{st}}T\big(T\frac{\partial f}{\partial A_T} - \frac{\partial f}{\partial \dot{A}_T}\big)}. \tag{5.11}$$

Finally, Eq. (5.11) suggests a universal criterion for evaluating the stability of OEOs.

5.2.2 Apply the Universal Stability Analysis into the Basic OEO

Now, we apply the universal stability analysis to the basic OEO proposed in Chapter 2 to evaluate its effectiveness by comparing the stability results from the universal models with the results obtained in Chapter 2. First, we need to identify the nonlinear function, which can be written as:

$$f_{\text{NL}}[A_T] = 2\text{Jc}_1[2A_T]A_T. \tag{5.12}$$

Since the function only depends on A_T, we can only calculate the derivative with respect to A_T, which can be obtained as

$$\frac{\partial f}{\partial A_T} = -2\text{Jc}_1[2A_{\text{st}}] + 2\text{J}_0[2A_{\text{st}}]. \tag{5.13}$$

For the trivial solution, $A_{\text{tr}} = 0$, the nonlinear function corresponds to 1. Applying this into Eqs. (5.9) and (5.11) results in Eqs. (2.29) and (2.30) respectively. Therefore, through the universal models, it is possible to obtain the same results as those obtained in Chapter 2. For the oscillatory solution, Eq. (5.13) is equivalent to $2\text{J}_0[2A_{\text{osc}}] - 1/\gamma$. Applying this into Eqs. (5.9) and (5.11) yields Eqs. (2.35) and (2.36), which also verify the validity of the universal expressions.

5.2.3 Apply the Universal Stability Analysis into the SBS-based OEO

Now, we apply the universal analysis into the SBS-based OEO proposed in Chapter 5 to observe their validity. We first need to identify the nonlinear function, which can be written as:

$$f_{\text{NL}}[A, A_T, \dot{A}_T] = 4\text{Jc}_1^2[A_T]A_T - \frac{A\dot{A}_T\text{J}_2[A_T]}{\mu\gamma\text{J}_1[A_T]}. \tag{5.14}$$

Due to the more complicated dynamics of the microwave photonic filtering compared to the basic setup, the nonlinear function of the SBS-based OEO depends on A, A_T, and $\dot{A}_T$. Therefore, we need to define the three differentials, which can be expressed as:

$$\frac{\partial f}{\partial A} = 0 \tag{5.15}$$

$$\frac{\partial f}{\partial A_T} = 4\mathrm{Jc}_1^2[2A_{\mathrm{st}}] + 8A_{\mathrm{st}}\mathrm{Jc}_1[2A_{\mathrm{st}}]\mathrm{Jc}_1'[2A_{\mathrm{st}}] \tag{5.16}$$

$$\frac{\partial f}{\partial \dot{A}_T} = -\frac{A_{\mathrm{st}}\mathrm{J}_2[A_{\mathrm{st}}]}{\mu\gamma\mathrm{J}_1[A_{\mathrm{st}}]}. \tag{5.17}$$

Equating the three differential results into Eqs. (5.9) and (5.11) results in Eqs. (4.75) and (4.74) for the trivial solution case and Eqs. (4.81) and (4.80) for the oscillatory solution case as expected.

5.2.4 Universal Stability Analysis

Through studying various models and the universal equation, it is possible to conclude that the stability analysis generally yields two bifurcation values γ_{th} and γ_{cr}. For the gains, the trivial fixed point is stable when $0 \leq \gamma < \gamma_{\mathrm{th}}$, while the oscillatory solution is stable whenever $\gamma_{\mathrm{th}} < \gamma < \gamma_{\mathrm{cr}}$. As long as BPFs are narrow enough, OEOs generally display similar behavior, with different critical gains and oscillation magnitudes, thereby different oscillatory solutions. Comparing Figs. (2.5) and (4.5) or Figs. (2.6) and (4.6) further verifies their similarities.

Below the threshold gain, the trivial solution is stable, but the system soon experiences a primary Hopf bifurcation at the threshold [3, 33]. When the gain is further increased, the system undergoes a secondary Hopf bifurcation, also known as a Neimark-Sacker (or *torus*) bifurcation, beyond which the oscillatory solution is unstable [3, 93, 94]. The amplitude shows $2T$ periodic behavior right after the Neimark-Sacker bifurcation and $4T$ periodic behavior by further increasing the gain. At very high gains, the behaviors finally become chaotic. Note that the square-wave behavior is due to the fact that the delay is substantially larger than $1/\mu$ [67].

5.3 The Frequency-Doubled Output

By manipulating phase or polarization of optical fields, a frequency-multiplicative model generates a subsequent harmonic at a separate output port and keeps tuning the fundamental (oscillation) frequency in the closed-loop [41–45,50,51]. We can describe the doubled-frequency generations using the following variable [63]:

$$\mathcal{C} = G_0 \mathrm{J}_2[d|\mathcal{A}|]e^{i\varphi(t)} \tag{5.18}$$

where G_0 is the output gain and d is an integer determined by modulators. Taking the time-derivative of the above expression, we obtain dynamics in a similar form as Eq. (5.1), which results in:

$$\dot{\mathcal{C}} = -2\frac{\dot{\mathcal{A}}}{\mathcal{A}}\mathcal{C} + dG_o \mathrm{J}_1[d|\mathcal{A}|]\dot{\mathcal{A}}e^{i\frac{\varphi(t)}{2}}. \tag{5.19}$$

The output is expressed as a coupled equation with the dynamic equation, and thus, the expression can also open possibilities of researching the oscillating loop and separate output ports simultaneously [96].

5.4 Conclusion of the Chapter

In this chapter, we derived the universal microwave envelope equation based on the findings from the preceding sections and developed the models suitable for stability analysis. Utilizing these universal models, we conducted stability analyses of the OEOs, which yielded the results consistent with those presented in Chapters 2 and 4, affirming the validity of the universal

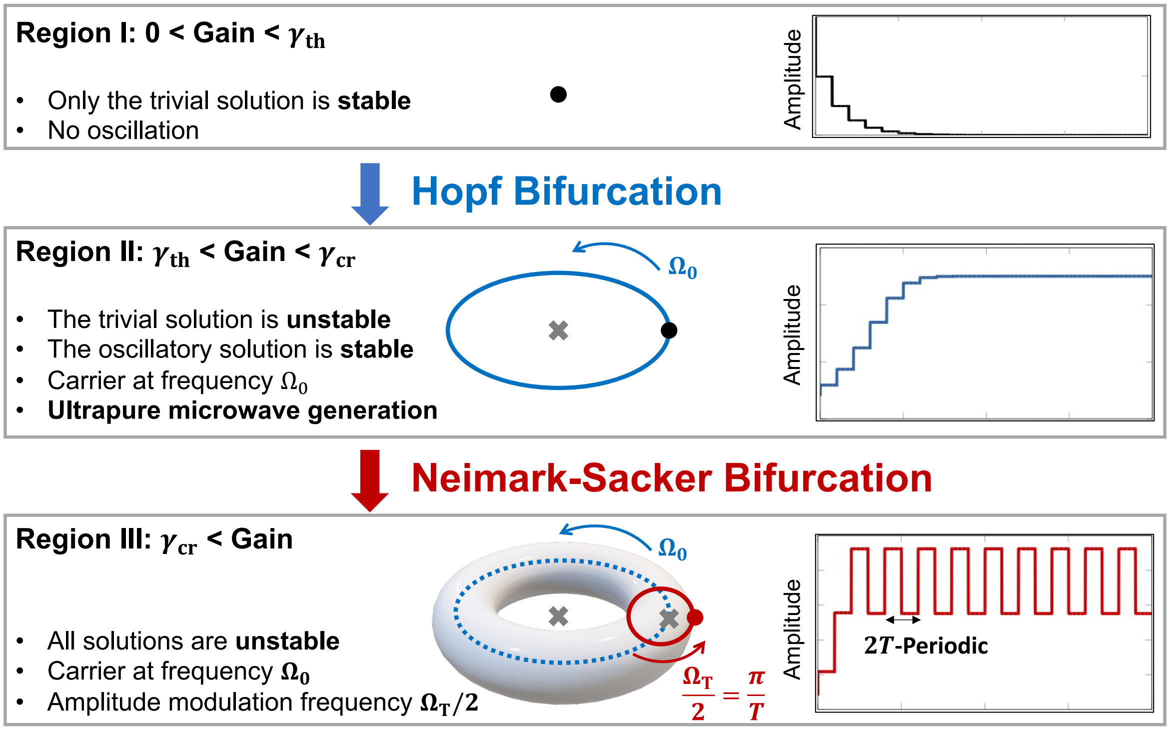

Figure 5.1: The illustration of the bifurcation sequence of the OEOs. The dynamics of OEOs can be segmented into three regimes. In the first regime, where the gain is below the threshold level, there is no oscillation occurs because the trivial solution is stable. When the loop gain parameter exceeds the threshold value, a Hopf bifurcation occurs, stabilizing the oscillatory solution while rendering the trivial solution unstable. Consequently, OEOs operate as limit-cycle oscillators in this regime, ensuring stable oscillation regardless of the initial conditions. This is dedicated for pure microwave generation. With further gain increases, the systems encounter a Neimark-Sacker bifurcation, causing the oscillatory solution to become unstable. Initially, the systems exhibit regular amplitude modulation, but with continued gain increase, the oscillators behave akin to a torus, as depicted.

envelope equation. Importantly, the universal equation suggests that the dynamics of OEOs remain highly similar irrespective of their dynamical complexities. We also derived the universal envelope equation of the frequency-doubled setups so that it is also possible to open possibilities of researching the oscillating loop and separate output ports simultaneously.

The analysis is encapsulated in Fig. 5.1, illustrating the system dynamics across varying loop gains. The behavior of OEOs can be segmented into three regimes. In the first regime, where the gain is below the threshold level, there is no oscillation occurs because the trivial solution is stable. When the loop gain parameter exceeds the threshold value, a Hopf bifurcation occurs, stabilizing the oscillatory solution while rendering the trivial solution unstable. Consequently, OEOs operate as limit-cycle oscillators in this regime, ensuring stable oscillation regardless of the initial conditions. This is dedicated for pure microwave generation. With further gain increases, the systems encounter a Neimark-Sacker bifurcation, causing the oscillatory solution to become unstable. Initially, the systems exhibit regular amplitude modulation, but with continued gain increase, the oscillators behave akin to a torus, as depicted.

The significance of this chapter lies in the revelation that the universal envelope equation highlights the dynamic similarities among OEOs regardless of their complexities. This suggests that dynamical behavior observed in one setup may be mirrored in others, enabling interpretations or analyses applicable across different setups. For instance, results of a detailed examination of the fundamental setup can be applicable to other OEOs while the universal equation can provide a path for the transferring.

Chapter 6: The Stochastic Delay Differential Equation of the Phase

6.1 Introduction of the Chapter

In Chapter 5, we examined the dynamical similarities among different OEOs and derived the universal microwave envelope equation, expressed in the first order delay differential deterministic form. Our focus primarily centered on comprehending the dynamics of the magnitude, while the phase dynamics left unaddressed. Here, our focus shifts to investigating phase dynamics through the utilization of a stochastic approach, which enables us to optimize and comprehend phase noise performance effectively.

We first transform the universal deterministic envelope equation into a stochastic delay differential equation (SDDE), effectively describing the phase dynamics. To analyze the oscillators, we categorize noise sources into two types: an *additive* noise contribution, stemming from random environmental and internal fluctuations, and a *multiplicative* noise contribution, arising from noisy loop gain. The existence of the additive noise is independent of oscillation existence, while the multiplicative noise is intertwined with the noisy loop gain, thereby nonlinearly mixed with signals above the threshold [35, 64–66]. Since our focus is on investigating the phase noise spectrum, we delve into the above-threshold regime in this chapter.

By employing the Langevin approach, we can directly incorporate the noise contributions into the envelop equations. Subsequently, we can convert the stochastic envelope equation into the SDDE of the phase using stochastic calculus. Later, through Fourier transform of the model, we can obtain the power spectral density (PSD) of the phase term, enabling theoretical investigation of phase noise. Thus, the SDDE serves as a tool for predicting phase noise of setups and optimizing phase noise performance. We delve into a thorough analysis of the noise spectrum and compare it with experimental results.

This chapter comprises the following sections. In Section 6.2, we employ the Langevin approach to transform the deterministic universal envelope equation presented in Eq. (5.1) into a stochastic form. In Section 6.3, we convert the noisy envelope model into the SDDE of the phase, where we conduct a thorough investigation of the model. We derive the phase noise spectrum from the stochastic model and deeply explore its characteristics, presenting an experimental result for comparison. Finally, the chapter is summarized and concluded in Section 6.4.

6.2 Derivation of the Stochastic Delay Differential Equation

To consider noise in the oscillators, we can account for two main noise contributions of the systems. The first contribution is the additive noise which accounts for thermal noise, shot noise, and laser relative intensity noise (RIN) at high frequencies. This contribution can be assumed to be spectrally white and is not related to existence of an oscillating signal. Since we are interested in noise *near* the oscillation frequency, it is possible to express the noise in terms of its complex conjugate envelopes, similar to how we defined the oscillation voltages and optical fields in terms of their complex conjugate envelopes. This results in the following expression:

$$\xi_{\mathrm{a}}(t) = \frac{1}{2}\zeta_{\mathrm{a}}(t)e^{i\Omega_0 t} + \frac{1}{2}\zeta_{\mathrm{a}}^*(t)e^{-i\Omega_0 t} \tag{6.1}$$

where $\zeta_{\rm a}(t)$ represents the complex envelope, with the subscript "a" denoting the additive noise. The real and complex noise variables are in units of $1/s^{1/2}$, and their auto-correlations respectively obey $\langle \xi_{\rm a}(t)\xi_{\rm a}^*(t')\rangle = \delta(t-t')$ and $\langle \zeta_{\rm a}(t)\zeta_{\rm a}^*(t')\rangle = 2\delta(t-t')$, leading to their PSDs being $|\tilde{\xi}_{\rm a}(i\omega)|^2 = 1$ and $|\tilde{\zeta}_{\rm a}(i\omega)|^2 = 2$. The effect of this contribution can be accounted for as a Langevin forcing term, and it can be directly added to the dynamic equation of the OEO. However, it should be noted that since we have not considered the diffusion constants in the auto-correlations defined above, we should include the scale factor in the ultimate expression, which will be shown in Eq. (6.4) later.

The next noise contribution that we consider is the multiplicative noise due to the noisy loop gain which depends on a lot of factors that can be noisy as shown in Eq. (2.7). The multiplicative noise considers colored noise of amplifiers, laser RIN at low frequencies, and optical frequency noise due to dispersion. Given the noisy parameters such as the noisy conversion gain $S \to S + \delta S(t)$ and noisy amplifier gain $G \to G + \delta G(t)$, there will be overall noisy fluctuation near the gain, which can be mathematically expressed as $\gamma \to \delta\gamma(t)$. In order to express the noise differently, we introduce a dimensionless multiplicative noise as

$$\eta_{\rm m}(t) = \frac{\delta\gamma(t)}{\gamma} \tag{6.2}$$

where it is in units of $1/s^{1/2}$ and represents the relative gain fluctuation and obeys $\eta_{\rm m}(t) \ll 1$ [35]. When considering that the main causes of the noise are generally RFAs and PDs, we can approximate the multiplicative noise as flicker at low offset frequencies and white above a certain knee value [35, 64–66]. Under these conditions, we can justify the following expression:

$$|\tilde{\eta}_{\mathrm{m}}(i\omega)|^2 = \left[1 + \frac{\Omega_{\mathrm{H}}}{\omega + \Omega_{\mathrm{L}}}\right] \tag{6.3}$$

where Ω_{L} and Ω_{H} are respectively the low and high corner frequencies of the flicker noise. The noise remains flicker in between the two corner frequencies and white elsewhere. Based on the given definitions and Langevin approach, we can directly include the additive and multiplicative noise contributions into Eq. (5.1) to describe the universal envelope dynamics with noise, resulting in

$$\dot{\mathcal{A}} = -\mu e^{i\vartheta}\mathcal{A} + \mu\gamma\left[1 + \frac{\sigma_{\mathrm{m}}}{\sqrt{2\mu}}\eta_{\mathrm{m}}(t)\right]e^{i\vartheta} f_{\mathrm{NL}}[\mathcal{A}, \mathcal{A}_T, \dot{\mathcal{A}}_T] + \mu e^{i\vartheta}\frac{\sigma_{\mathrm{a}}}{\sqrt{2\mu}}\zeta_{\mathrm{a}}(t) \tag{6.4}$$

where we omit the time-domain expression for the complex envelope $\mathcal{A}(t) \rightarrow \mathcal{A}$ and adapt $\sigma = \pi$ (Please refer to Chapter 2), while $\sigma_{\mathrm{a,m}}$ respectively describe the magnitudes of the two noise sources and generate their diffusion constants, which can be written as $D_{\mathrm{a,m}} = \sigma_{\mathrm{a,m}}^2/2$. We intentionally subtract $1/\sqrt{2\mu}$ from $\sigma_{\mathrm{a,m}}$ to make the diffusion constants as dimensionless.

In the sub-threshold regime where the loop gain is less than unity, we can linearize Eq. (6.4) around the trivial solution, yielding:

$$\dot{\mathcal{A}} = -\mu(1 - a\gamma)e^{i\vartheta}\mathcal{A} + \mu\gamma b e^{i\vartheta}\mathcal{A}_T + \mu e^{i\vartheta}\frac{\sigma_{\mathrm{a}}}{\sqrt{2\mu}}\zeta_{\mathrm{a}}(t) \tag{6.5}$$

where we take into account that in the sub-threshold regime, we could linearize the nonlinear function as $f_{\mathrm{NL}}[\mathcal{A}, \mathcal{A}_T, \dot{\mathcal{A}}_T] = a\mathcal{A} + b\mathcal{A}_T$ around the trivial fixed point. Here, we do not consider a dependence on $\dot{\mathcal{A}}_T$ because it either does not appear in most OEO equations or results in higher-order terms as shown in the previous chapters. In Eq. (6.5), it is noteworthy that the multiplicative noise contribution is neglected in this regime as it generates higher-order terms. This is indeed acceptable considering that the multiplicative noise is attributed to the noisy loop gain, but the loop is not closed in the sub-threshold regime. By Fourier transforming Eq. (6.5), it is possible to obtain the PSD of this regime as:

$$|\tilde{\mathcal{A}}(i\omega)|^2 = \frac{2\mu D_{\mathrm{a}}}{|\mu[(1-a\gamma) - b\gamma e^{-i\omega T}] + i\omega e^{-i\vartheta}|^2} \,. \tag{6.6}$$

The dynamics described by Eq. (6.6) is illustrated in Fig. 6.2. For the simulation, we consider the basic OEO setup case ($a = 0$ and $b = 1$) and neglected ϑ by assuming the filter has a high enough Q-factor. The PSD follows the spectral shape of the RF filter, considering a single-side band. However, it is noteworthy that unlike classic filters, it exhibits a quasi-flat shape inside the bandwidth, where the spurious peaks are generated due to the FSR from the fiber delay line. If we further increase the loop gain, the roll-off becomes steeper.

6.3 Phase Dynamics Above the Threshold

In the above-threshold regime, we can linearize the nonlinear function near the oscillatory solution by using a property given as $f_{\mathrm{NL}}[\mathcal{A}, \mathcal{A}_T, \dot{\mathcal{A}}_T] = [a\mathcal{A} + b\mathcal{A}_T]/\gamma$, resulting in the following expression:

$$\begin{aligned}\dot{\mathcal{A}} = &-\mu e^{i\vartheta}\left[(1-a) - a\frac{\sigma_{\mathrm{m}}}{\sqrt{2\mu}}\eta_{\mathrm{m}}(t)\right]\mathcal{A} + \mu b e^{i\vartheta}\left[1 + \frac{\sigma_{\mathrm{m}}}{\sqrt{2\mu}}\eta_{\mathrm{m}}(t)\right]\mathcal{A}_T \\ &+ \mu e^{i\vartheta}\frac{\sigma_{\mathrm{a}}}{\sqrt{2\mu}}\zeta_{\mathrm{a}}(t).\end{aligned} \tag{6.7}$$

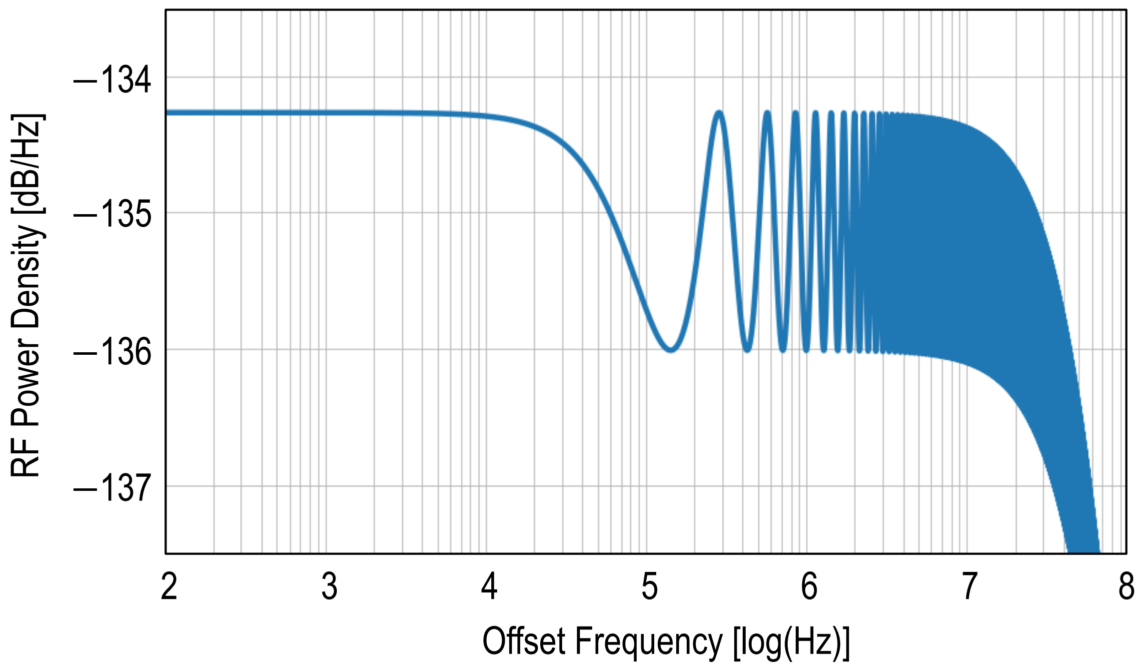

Figure 6.1: The analytical PSD $|\tilde{\mathcal{A}}(i\omega)|^2$ below the threshold shown in Eq. (6.6) with the parameters of $T = 22\ \mu$s, $\mu = 2\pi \times 10.5$ MHz, $D_{\mathrm{a}} = 1 \times 10^{-6}$, $\gamma = 0.1$, $a = 0$, $b = 1$, and $\vartheta = 0$. The PSD follows the spectral shape of the RF filter, considering a single-side band. However, unlike classic filters, it exhibits a quasi-flat shape inside the bandwidth, where the spurious peaks are generated due to the FSR from the fiber delay line. If we further increase the loop gain, the roll-off becomes steeper.

Now, we convert the above stochastic equation that describes the dynamics of the noisy envelope into another stochastic form describing the noisy dynamics of the phase. In [35], it was proposed that we can use Itô chain rules to derive the stochastic differential equation for the phase. Before using the rule, we first write (6.7) under the differential form

$$d\mathcal{A} = -\,\mu e^{i\vartheta}\left[(1-a) - a\frac{\sigma_{\mathrm{m}}}{\sqrt{2\mu}}\eta_{\mathrm{m}}(t)\right]\mathcal{A}dt + \mu b e^{i\vartheta}\left[1 + \frac{\sigma_{\mathrm{m}}}{\sqrt{2\mu}}\eta_{\mathrm{m}}(t)\right]\mathcal{A}_T dt$$
$$+\,\mu e^{i\vartheta}\frac{\sigma_{\mathrm{a}}}{\sqrt{2\mu}}d\mathcal{W}_{\mathrm{a}}(t). \tag{6.8}$$

where $d\mathcal{W}_a(t) = dW_{a,r}(t) + idW_{a,i}(t)$ is the differential Wiener process. $W_{a,r}(t)$ and $W_{a,i}(t)$ are respective the real and imaginary parts of the Wiener process, and they are uncorrelated

$\langle W_{a,r}(t), W_{a,i}(t)\rangle = 0$, while having equal variance $\langle (W_{a,i}(t))^2\rangle = \langle (W_{a,r}(t))^2\rangle = dt$.

Now, from the above expression, we want to extract the information of the phase solely, so as a trick, we define $\mathcal{A} = \sqrt{P(t)}e^{i\psi(t)} = e^{\rho(t)+i\psi(t)}$ where $\rho(t) = (1/2)\ln P(t)$. Plugging this expression into Eq. (6.8) allows us to use Itô lemma, and at order dt, we obtain the new expression as follow:

$$
\begin{aligned}
d\rho(t) + id\psi(t) = d\ln\mathcal{A} = \frac{d\mathcal{A}}{\mathcal{A}(t)} - \frac{1}{2}\left[\frac{d\mathcal{A}}{\mathcal{A}}\right]^2 \simeq \frac{d\mathcal{A}}{\mathcal{A}} \\
= -\,\mu e^{i\vartheta}\left[(1-a) - a\frac{\sigma_{\mathrm{m}}}{\sqrt{2\mu}}\eta_{\mathrm{m}}(t)\right]dt + \mu b e^{i\vartheta}\left[1 + \frac{\sigma_{\mathrm{m}}}{\sqrt{2\mu}}\eta_{\mathrm{m}}(t)\right]\frac{\mathcal{A}_T}{\mathcal{A}}dt \\
+ \mu e^{i\vartheta}\frac{\sigma_{\mathrm{a}}}{\sqrt{2\mu}}\frac{1}{\mathcal{A}}d\mathcal{W}_{\mathrm{a}}(t). \qquad (6.9)
\end{aligned}
$$

The above expression implies that we can only consider the imaginary part to explore the dynamics of the phase solely, and it is possible to write:

$$
\begin{aligned}
d\psi = -\,\mu\sin\vartheta\left[(1-a) - a\frac{\sigma_{\mathrm{m}}}{\sqrt{2\mu}}\eta_{\mathrm{m}}(t)\right]dt + \frac{\mu}{A_{\mathrm{osc}}}\frac{\sigma_{\mathrm{a}}}{\sqrt{2\mu}}dW_{a,\psi}(t) \\
+ \mu b\left[1 + \frac{\sigma_{\mathrm{m}}}{\sqrt{2\mu}}\eta_{\mathrm{m}}(t)\right]\sin(\vartheta + \psi_T - \psi)dt \qquad (6.10)
\end{aligned}
$$

where we consider $|\mathcal{A}| = |\mathcal{A}_T| = A_{\mathrm{osc}}$ and omit the time-domain expression, $\psi(t) \to \psi$. The real Gaussian white noise $\xi_{a,\psi}(t)$ has its differential Wiener process $dW_{a,\psi}(t) = dW_{a,r}(t)\sin\vartheta + dW_{a,i}(t)\cos\vartheta$, satisfying $\langle \xi_{a,\psi}(t)\xi_{a,\psi}(t')\rangle = \delta(t-t')$. For the ultra-stable oscillators, the noise is necessarily very small and we can establish the following approximation: $|\psi - \psi_T| \ll \vartheta \ll 1$, which allows for the linearization $\sin[\vartheta - (\psi - \psi_T)] \simeq \vartheta - (\psi - \psi_T)$. Then, the SDDE describing the dynamics of the phase, can be written as:

$$\dot{\psi} = \frac{\mu(a+b-1)}{2Q_{\mathrm{rf}}} - \mu b(\psi - \psi_T) + \frac{\mu\sigma_{\mathrm{m}}(a+b)}{2Q_{\mathrm{rf}}\sqrt{2\mu}}\eta_m(t) + \frac{\mu\sigma_{\mathrm{a}}}{A_{\mathrm{osc}}\sqrt{2\mu}}\xi_{a,\psi}(t). \tag{6.11}$$

The first term on the right-hand side can be discarded in the frequency domain as it is a Dirac term, which leads to write the PSD of the phase as

$$|\tilde{\Psi}(i\omega)|^2 = \frac{\mu}{2}\left|\frac{(a+b)\sigma_{\mathrm{m}}\tilde{\eta}_m(i\omega)/(2Q_{\mathrm{rf}}) + \sigma_{\mathrm{a}}\tilde{\xi}_{a,\psi}(i\omega)/A_{\mathrm{osc}}}{i\omega + \mu b(1-e^{-i\omega T})}\right|^2. \tag{6.12}$$

The aforementioned expression delineates how specific factors influence the ultimate phase noise. Firstly, σ_{m} and σ_{a} govern the overall noise level, where these parameters are determined by components within the setup, such as RFAs and PDs, and environmental fluctuations. Chapter 7 elaborates on quantifying these parameters, enabling the prediction of noise levels prior to frequency locking. The multiplicative noise contribution can be mitigated by implementing narrow filters.

The PSD of the phase (the phase noise spectrum) is depicted in Fig. 6.2. We now partition the offset frequency into three regimes and analyze each separately, as they exhibit distinct shapes. The regimes are as follows: *(i)* low offset frequencies ($\omega \ll \Omega_{\mathrm{H}}$); *(ii)* the spurious peak region ($\Omega_{\mathrm{H}} \ll \omega \ll \mu$); and *(iii)* beyond the half-bandwidth: $\omega \gg \mu$.

6.3.1 Phase Noise at Low Offset Frequencies: $\omega \ll \Omega_{\mathrm{H}}$

In the regime where offset frequencies are very small, particularly when $\omega \ll \Omega_{\mathrm{H}}$, the flicker noise is dominant over the additive noise, as illustrated in Fig. 6.2. In order to comprehend it mathematically, we can approximate Eq. (6.12) for this specific regime. Throughout the

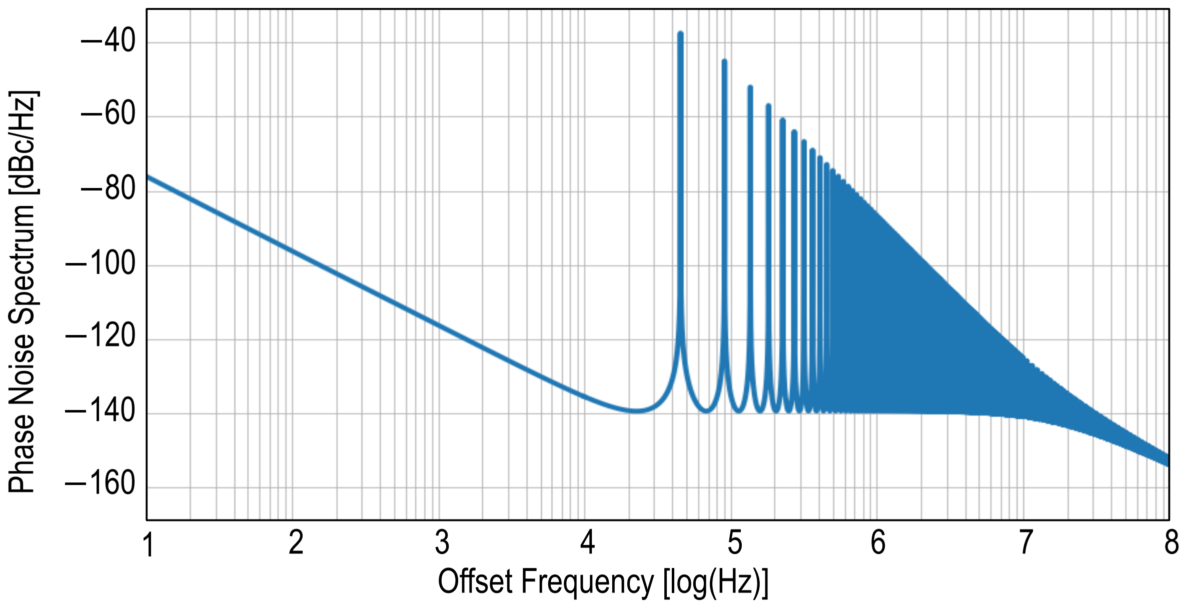

Figure 6.2: The PSD of the phase (phase noise spectrum) above the threshold obtained by using Eq. (6.12) with the parameters of $T = 22\ \mu$s, $\mu = 2\pi \times 10.5$ MHz, $D_{\mathrm{a}} = 1 \times 10^{-6}$, $D_{\mathrm{m}} = 1 \times 10^{-4}$, $\Omega_H = 2\pi \times 100$ kHz, $\Omega_L = 2\pi \times 1$ Hz, $A_{\mathrm{osc}} = 0.58$, and $Q_{\mathrm{RF}} \simeq 500$. In order to obtain the results, sampling frequencies of 100 Hz within the range of 100 Hz to 10 kHz, 0.2 Hz within 10 kHz to 10 MHz, and 9 kHz within 10 MHz to 100 MHz are used. If frequencies near the carrier ($\omega \ll \Omega_{\mathrm{H}}$), the flicker noise is dominant over the additive noise. When frequencies lie between the high corner frequency of the flicker and the half-bandwidth ($\Omega_{\mathrm{H}} \ll \omega \ll \mu$), there are spurious peaks due to the FSR on the quasi-flat baseline and the effect of the multiplicative noise is minimal here. Lastly, if frequencies beyond the half-bandwidth ($\omega \gg \mu$), the FSR term becomes negligible and the noise level decreases.

entire thesis, we have set that $\mu T \gg 1$, which is generally reasonable for most OEOs, and this assumption allows us to further approximate $\omega T \ll 1$ in the current region. Considering that, we can obtain the PSD in the regime by following the below procedure:

$$
\begin{aligned}
|\tilde{\Psi}(i\omega)|^2 &\simeq \frac{\mu}{2}\left|\frac{(a+b)\sigma_{\mathrm{m}}\tilde{\eta}_m(i\omega)/(2Q_{\mathrm{rf}}) + \sigma_{\mathrm{a}}\tilde{\xi}_{a,\psi}(i\omega)/A_{\mathrm{osc}}}{i\omega + i\omega b\mu T}\right|^2 \\
&\simeq \frac{(a+b)^2(2Q_{\mathrm{rf}})^{-2}D_{\mathrm{m}}|\tilde{\eta}_m(i\omega)|^2 + D_{\mathrm{a}}A_{\mathrm{osc}}^{-2}}{b^2\mu T^2\omega^2} \\
&\simeq \frac{(a+b)^2(2Q_{\mathrm{rf}})^{-2}D_{\mathrm{m}}\Omega_{\mathrm{H}}}{b^2\mu T^2\omega^3}
\end{aligned}
\tag{6.13}
$$

where we apply the Taylor expansion for the exponential term and assume that $D_{\mathrm{m}} \gg D_{\mathrm{a}}$. In this regime, the noise becomes nearly inconsequential to the oscillation magnitude, provided that the multiplicative noise dominates over the additive noise. In addition, it is worth to note that the oscillator adheres to Leeson's model, given that the noise spectrum is proportional to f^{-3} for the flicker noise [35, 97].

6.3.2 Phase Noise in the Spurious Peak Region: $\Omega_{\mathrm{H}} \ll \omega \ll \mu$

When frequencies lie between the high corner cutoff frequency of the flicker and the half-bandwidth, we observe an intriguing dynamics, which are the spurious peaks. These peaks are generated due to the FSR from the fiber spool, superimposed on a quasi-flat noise floor. This frequency regime merits exploration, particularly because it is where we typically evaluate the performance of OEOs, most commonly at a 10 kHz offset frequency. In the regime, the impact of the multiplicative noise is less pronounced compared to the preceding regime, owing to the high Q-factor of a filter in the system and the approximate equality of $|\tilde{\eta}(i\omega)|^2$ to 1. Additionally, the effect of the colored noise is minimal here as shown in Fig. 6.2.

In order to define the quasi-flat noise level initially, we need to find the minimum value of Eq. (6.12), which occurs when $T = 0$. Accordingly, from Eq. (6.12), it is possible to find the baseline level by employing the following procedure:

$$\begin{aligned} |\tilde{\Psi}_{\mathrm{floor}}|^2 &= \frac{\mu}{2} \frac{|\sigma_{\mathrm{m}}\tilde{\eta}_m(i\omega)/(2Q_{\mathrm{rf}}) + \sigma_{\mathrm{a}}\tilde{\xi}_{a,\psi}(i\omega)/A_{\mathrm{osc}}|^2}{\omega^2 + 4\mu^2 b^2} \\ &\simeq \frac{1}{8\mu b^2} \left| \frac{\sigma_{\mathrm{m}}\tilde{\eta}_m(i\omega)}{2Q_{\mathrm{rf}}} + \frac{\sigma_{\mathrm{a}}\tilde{\xi}_{a,\psi}(i\omega)}{A_{\mathrm{osc}}} \right|^2 \\ &\simeq \frac{D_{\mathrm{a}}}{4\mu b^2 A_{\mathrm{osc}}^2} \end{aligned} \tag{6.14}$$

where we consider that the two different noise contributions are uncorrelated. The above expression indicates that we can mitigate the phase noise in this regime by increasing the loop gain, consequently increasing the oscillation magnitude. Therefore, one great way for phase noise optimization is increasing the loop gain manually, therefore by fixing the additive noise contribution as a constant factor. In Fig. 6.2, obtained for the case of the fundamental OEO proposed in Chapter 2 meaning $a = 0$ and $b = 1$, we used the following parameters: $D_{\mathrm{a}} = 1 \times 10^{-6}$, $A_{\mathrm{osc}} = 0.58$, and $\mu = 2\pi \times 10.5$ MHz. In that case, the floor level is approximately calculated as -139 dBc/Hz from Eq. (6.14), and it aligns with the displayed result in Fig 6.2.

The above expression indicates that we can mitigate the phase noise in this regime by augmenting the loop gain, consequently amplifying the oscillation magnitude. This is because the presence of oscillations renders the additive noise contribution irrelevant.

Now, we want to more closely look at the spurious peaks. Considering the definition of the FSR, one would anticipate that the positions of the spurious peaks ought to align with $\omega_n = n\Omega_T = 2\pi n/T$, denoting that they are located at integer multiples of the FSRs, where n represents any integer indicating the order. However, for a more precise determination of their locations, we opt to redefine these positions. For the analysis, we first define the denominator of Eq. (6.12) as a new function $k(\omega)$:

$$\begin{aligned} k(\omega) &= |i\omega + \mu b(1 - e^{i\omega T})|^2 \\ &= \omega^2 + i\mu\omega b(e^{-i\omega T} - e^{i\omega T}) + \mu^2 b^2 (2 - e^{-i\omega T} - e^{+1\omega T}). \end{aligned} \tag{6.15}$$

Now, we consider a small perturbation near the frequencies and we look into up to the fourth-order Taylor expansion, as follows:

$$
\begin{aligned}
k(n\Omega_T+\delta\omega) &\simeq k(n\Omega_T)+\delta\omega k'(n\Omega_T)+\frac{\delta\omega^2}{2}k''(n\Omega_T)+\frac{\delta\omega^3}{6}k'''(n\Omega_T)+\frac{\delta\omega^4}{24}k''''(n\Omega_T) \\
&\simeq (n\Omega_T+\delta\omega)^2+i\mu\omega b(-2iT\delta\omega+i\frac{T^3}{3}\delta\omega^3)-\mu^2b^2(T^2\delta\omega^2+\frac{T^4}{12}\delta\omega^4) \\
&\simeq (n\Omega_T+\mu Tb\delta\omega)^2-\frac{1}{3}\mu T^3 n\Omega_T b\delta\omega^3-\frac{1}{12}\mu^2T^4b^2\delta\omega^4
\end{aligned}
\tag{6.16}
$$

where we consider $\mu T \gg 1$ again. Using the new expression of the denominator, the PSD of the phase at the fouth-order Taylor expansion can be newly written as follow:

$$
|\tilde{\Psi}(\omega)|^2=\frac{\mu}{2}\frac{|(a+b)\sigma_{\mathrm{m}}\tilde{\eta}_m(\omega)/(2Q_{\mathrm{rf}})+\sigma_{\mathrm{a}}\tilde{\xi}_{a,\psi}(\omega)/A_{\mathrm{osc}}|^2}{(n\Omega_T+\mu Tb\delta\omega)^2-\frac{1}{3}\mu T^3n\Omega_Tb\delta\omega^3-\frac{1}{12}\mu^2T^4b^2\delta\omega^4}\,. \tag{6.17}
$$

In order to pinpoint the locations of the spurious peaks, we need to identify the perturbation frequencies that minimize the denominator function. In the scenario, the perturbation should fulfill the condition $n\Omega_T+\mu Tb\delta\omega=0$, as outlined in Eq. (6.17). Consequently, the corresponding frequency perturbations can be expressed as $\delta f=-n/(\pi\Delta FT^2b)$, which finally leads to the peak locations being described as:

$$
f_n=\frac{n}{T}-\frac{n}{\pi b\Delta FT^2}. \tag{6.18}
$$

In the above expression, it is possible to observe that there exists a trade-off when selecting the length of the fiber spool. As mentioned frequently, a longer delay can lead to a higher Q-factor of the system. However, according to Eq. (6.18), increasing the delay causes all the spurious peaks to shift to the left side (towards lower offset frequencies). Consequently, augmenting delays may induce unstable oscillations as the peaks move closer to the evaluation offset points. Given the locations, we can define their peaks by directly plugging Eq. (6.18) into Eq. (6.17), and it results in the following expression:

$$\begin{aligned}|\tilde{\Psi}_{\text{spurs}}|_n^2 &= \mu^3 \frac{(a+b)^2 D_{\text{m}}/(2Q_{\text{rf}})^2[1+\Omega_{\text{H}}/(\omega+\Omega_{\text{L}})] + D_{\text{a}}/A_{\text{osc}}^2}{4\pi^4 n^4/(b^2T^4)} \\ &= \mu^3 \frac{(a+b)^2 D_{\text{m}}/(2Q_{\text{rf}})^2 + D_{\text{a}}/A_{\text{osc}}^2}{4\pi^4 n^4/(b^2T^4)} \\ &\simeq \frac{\mu^3 b^2 T^4 D_{\text{a}}}{4A_{\text{osc}}^2 \pi^4 n^4}. \end{aligned} \tag{6.19}$$

The above expression also emphasizes the trade-off of selecting the length of a FDL, because a larger delay can result in greater spurious peaks. Given the narrow linewidth of the peaks, it is essential to determine an appropriate frequency resolution for simulations. In order to comprehend the narrowness, it is worth to look at their 3 dB bandwidths. By definition, we can find $\Delta\omega_n$ that satisfies the following condition: $|\tilde{\Psi}(\omega_n)|^2 = 2|\tilde{\Psi}(\omega_n + \Delta\omega_n/2)|^2$ where $\Delta\omega_n$ stands for the angular bandwidth of the spurious peaks. From Eqs. (6.17) and (6.18), we can establish the following relationship:

$$2 \times \frac{4}{b^2\mu^2}\left[\frac{\pi n}{T}\right]^4 = \left(\frac{1}{2} b\mu T \Delta\omega_n\right)^2 + \frac{4}{b^2\mu^2}\left[\frac{\pi n}{T}\right]^4. \tag{6.20}$$

Then, we can finally define the 3 dB bandwidth of the spurious peaks as

$$\Delta f_n = n^2 \frac{2\pi}{b^2\mu^2 T^3} \tag{6.21}$$

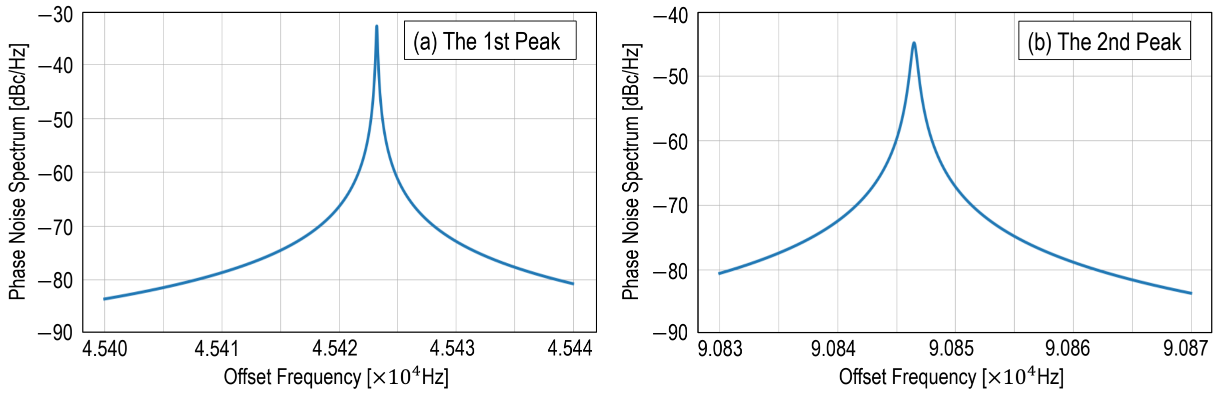

Figure 6.3: The zoomed views of the first two spurious peaks in Fig. 6.2 with the parameters of $T = 22\mu$s, $\mu = 2\pi \times 10.5$ MHz, $D_{\mathrm{a}} = 1 \times 10^{-6}$, $D_{\mathrm{m}} = 1 \times 10^{-4}$, $\Omega_H = 2\pi \times 100$ kHz, $\Omega_L = 2\pi \times 1$ Hz, $A_{\mathrm{osc}} = 0.58$, and $Q_{\mathrm{RF}} \simeq 500$. For the simulation, the sampling frequency of 4 μHz is used. The actual positions and magnitudes of the peaks little differ from the values depicted in Fig. 6.2.

where we assume that $\mu \gg \omega$ in the regime and the Q-factor of the RF filter is high enough.

Given the simulation conditions illustrated in Fig. 6.2, the peak locations can be expressed as $f_n = 50n$ kHz$-50n/\pi$ Hz. Calculating for the first and second peaks yields their positions as $49,984$ Hz and $99,968$ Hz respectively. At these frequencies, utilizing Eq. (6.19), the peak values are determined to be -32.9 and -44.9 dBm respectively. Notably, their bandwidths are computed as 0.16 Hz and 0.54 Hz. These values indicate that the resolution of 0.2 Hz utilized for Fig. 6.2 within the spurious peaks regime is not sufficiently narrow to yield accurate results. Consequently, the discrepancy between the magnitudes of the two spurious peaks shown in Fig. 6.2 and the calculated peak values arises. In Fig. 6.3, a resolution of 4 μHz is employed, aligning the displayed results with the calculated values.

6.3.3 Phase Noise Beyond the Half-Bandwidth: $\mu \ll \omega$

Lastly, beyond outside the bandwidth, the term generated by the FSR becomes negligible as $\omega \gg \mu$ in the denominator of Eq. (6.12). Consequently, the spectrum can be approximated as

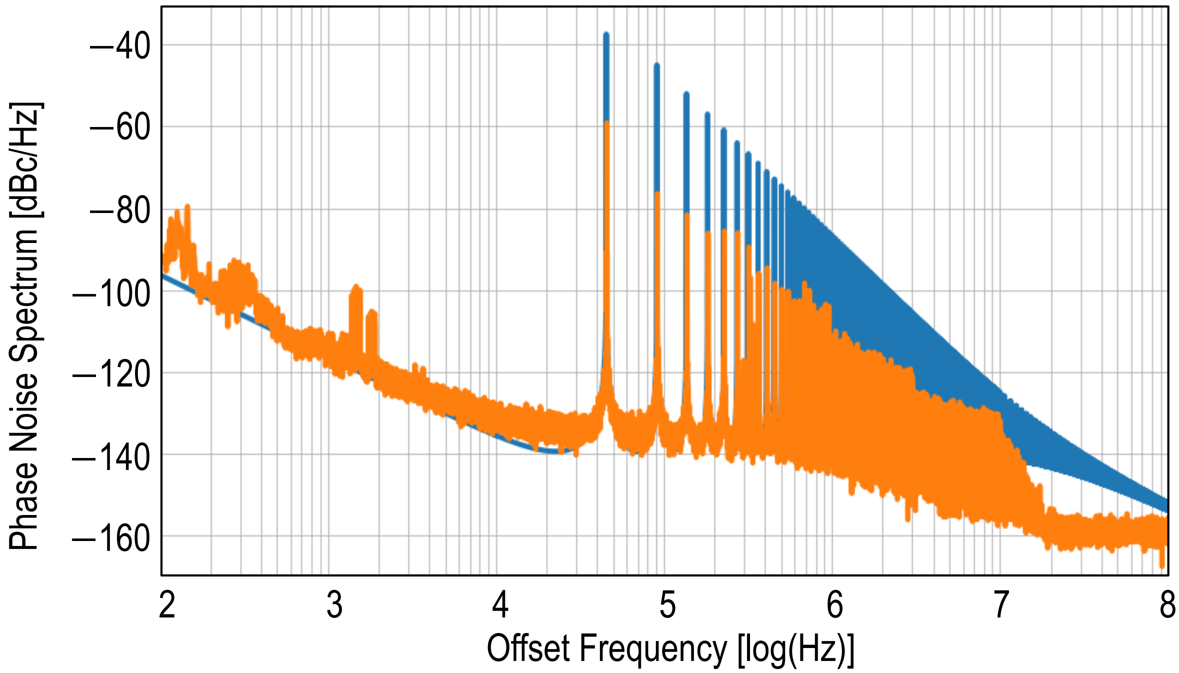

Figure 6.4: The analytical experimental phase noise spectra above threshold. The orange plot is obtained experimentally with a resolution of 0.1 $\%$ across the entire frequency range. Within every frequency decade, the spectrum is divided into two regions: the first 1/3 and the remaining portion. In each region, the resolution is 0.1 $\%$ of the maximum frequency within that region. For example, between 100 Hz and 1 kHz, the resolution is 3 Hz between 100 Hz and 300 Hz, and 10 Hz between 300 Hz and 1 kHz. The analytical plot depicted in blue is generated through numerically simulating Eq. (6.12) with the parameters of $T = 22\mu$s, $\mu = 2\pi \times 10.5$ MHz, $D_{\mathrm{a}} = 1 \times 10^{-6}$, $D_{\mathrm{m}} = 1 \times 10^{-4}$, $\Omega_H = 2\pi \times 100$ kHz, $\Omega_L = 2\pi \times 1$ Hz, $A_{\mathrm{osc}} = 0.58$, and $Q_{\mathrm{RF}} \simeq 500$. In order to obtain the numerical results, sampling frequencies of 100 Hz within the range of 100 Hz to 10 kHz, 0.2 Hz within 10 kHz to 10 MHz, and 9 kHz within 10 MHz to 100 MHz are used.

follows:

$$|\tilde{\Psi}(i\omega)|^2 \simeq \frac{\mu D_{\mathrm{a}}}{\omega^2 A_{\mathrm{osc}}^2} \,. \tag{6.22}$$

The expression present a strong damping obeying the f^{-2} decrease of the phase.

6.3.4 Experimental Phase Noise Spectrum

The phase noise spectrum of the fundamental OEO setup is experimentally obtained and illustrated in Fig. 6.4. The blue plot represents numerical simulations derived from Eq. (6.12), while the orange plot depicts the experimentally acquired phase noise spectrum using the Rhode and Schwarz FSW-43 phase noise spectrum function. The minimum resolution of the measurement device that 0.1 $\%$ of every frequency decade is used. Within every frequency decade, the spectrum is divided into two regions: the first 1/3 and the remaining portion. In each region, the resolution is 0.1 $\%$ of the maximum frequency within that region. For example, between 100 Hz and 1 kHz, the resolution is 3 Hz between 100 Hz and 300 Hz, and 10 Hz between 300 Hz and 1 kHz.

Upon comparison of the two sets of results, it was possible to estimate the diffusion constants of the two contributions as $D_\mathrm{a} = 1 \times 10^{-6}$ and $D_\mathrm{m} = 1 \times 10^{-4}$, respectively. In terms of the spurious peaks observed in the measurement, they exhibit smaller magnitudes compared to those in the simulation, suggesting that the lower amplitudes can be attributed to the limited resolution of the measurement device. We checked that a very tiny frequency resolution is required to correctly plot the spurious peaks. Overall, the close agreement between the two plots indicates that Eq. (6.12) serves as an excellent model for predicting the phase noise of OEOs.

6.4 Conclusion of the Chapter

In this chapter, we converted the deterministic universal microwave envelope equation into the SDDE form that describes the phase dynamics. During the derivation of the stochastic phase equation, we distinguished between two types of noise in the oscillators: the additive and multiplicative noise contributions. The additive noise contribution is attributed to the environmental and random fluctuations while the multiplicative noise is due to the noisy loop gain. Then, we directly included the contributions into the deterministic envelope equation. Given the phase equation, we were able to obtain the PSD of the phase, providing insight into the phase noise spectrum of OEOs. We conducted thorough theoretical and numerical investigations of the spectrum, revealing a significant level of agreement between two results. This alignment serves to validate the theoretical expression for the phase noise spectrum.

Chapter 7: Quantifying Additive and Multiplicative Noise in Optoelectronic Oscillators: An Experimental and Theoretical Analysis

7.1 Introduction of the Chapter

Since the primary goal of OEOs is generation of ultrastable microwave signal, a lot of OEO research interests lie in optimization of phase noise. Achieving this goal requires a comprehensive examination of the various noise sources, with a focus on how these stochastic fluctuations are coupled to the phase dynamics. Most research works along that line are primarily centered on phase noise analysis in the oscillating regime as discussed in Chapter 6, when the oscillator gain is set above the threshold [35, 63]. However, in that case, the noise is nonlinearly coupled to the oscillating signal, and it is not straightforward to characterize it unambiguously.

In this chapter, we propose a novel approach for noise characterization in OEOs based on the fact that from the modeling standpoint, noise sources should be accounted for independently from the fact that the oscillator is under or above the threshold. However, under the threshold, there is no signal and the oscillator is driven by the stochastic noise to be characterized. Since the sub-threshold regime is linear, it becomes possible to reverse-engineer the noise power using a Fourier transform formalism. We therefore aim in this study at presenting a comprehensive framework for quantifying noise contributions in OEOs with that methodology, that is, by operating the oscillator in the sub-threshold regime.

In the previous chapters, it was discussed that for the OEOs, dynamic equations can be derived by establishing relationships between input and output signals for an RF filter in the electric path or a MPF in the optical path of the feedback loop, finally resulting in a first-order integro-differential form. Importantly, in Chapter 5, it was demonstrated that the dynamics of various OEO setups can be *universally* described using a deterministic form applicable across various configurations. Therefore, although the work of this chapter focuses on a fundamental setup, akin to the setup described in Chapter 2, that is only composed of the essential core components, the same approach can be extended to derive noise characteristics for other OEO setups as well. However, it should be noted that noise sources such as flicker noise cannot be characterized using this approach for being consubstantial to the existence of a carrier above the threshold.

The transformation allows us to obtain the expressions of the additive and multiplicative noise contributions as functions of noisy RF output power, as shown in Section 7.2. In particular, the additive noise can be defined by deactivating the laser source or operating the modulator at the MITP, given its independence from loop gain. Conversely, the expression for the multiplicative noise indicates a dependence on gain, but experimental observations suggest that its magnitude may remain relatively constant beyond the threshold. As a result, in Section 7.3, it is shown that we can effectively quantify the noise contributions by measuring the RF noise powers within the RF domain. This methodology suggests valuable insights into noise characteristics and enables us to proactively address noise-related challenges in OEOs. The chapter is concluded in Section 7.4.

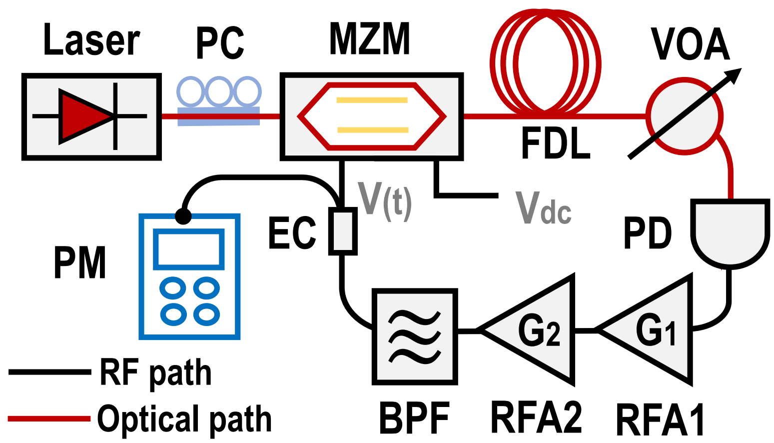

Figure 7.1: Schematic representation of the OEO setup, comprising a laser, a polarization controller (PC) for principal axis alignment, a Mach-Zehnder modulator (MZM) for electro-optic modulation, a fiber delay line (FDL) to store optical energy for RF signal generation, a variable optical attenuator (VOA) for manual gain control, a photodetector (PD) for signal conversion, two radiofrequency amplifiers (RFAs) for loss compensation, a bandpass filter (BPF) for the center frequency selection, and an electric coupler (EC) for measuring purpose. The MZM is driven by $V(t)$, and the RF power is measured using an RF power meter (PM).

7.2 Model

The setup is depicted in Fig. 7.1. The only two distinctions between this configuration and the fundamental setup shown in Fig. 2.2 are as follows: Firstly, there are two RFAs introduced to compensate the loop loss, where we define the total gain from the amplifier as $G = G_1 G_2$. Secondly, we incorporate a variable optical attenuator (VOA) to manually regulate the loop gain. Therefore, without any induced optical loss from the VOA, the loop gain is always greater than unity.

7.2.1 Derivation of the Stochastic Model

The oscillator is driven by a wide variety of noise sources. In this study, we lump them into the two main contributions as mentioned previously in Chapter 6. The first contribution accounts for all the environmental fluctuations that perturb the system. We here consider that this contribution is additive. The second contribution accounts for the fluctuations of the gain in the feedback loop, and it mathematically corresponds to a multiplicative stochastic term. We here consider that both stochastic contributions can be modeled as Gaussian white noise terms. This methodology where noise is directly accounted for as a perturbation in a core deterministic model in the time-domain is known as the Langevin approach.

We can directly incorporate the two noise contributions into Eq. (2.6) to obtain the following Langevin equation:

$$
\begin{aligned}
x + \frac{1}{\Delta\Omega}\frac{dx}{dt} + \frac{\Omega_0^2}{\Delta\Omega}\int_{t_0}^{t} x(s)\,ds = \frac{1}{\sqrt{\Delta\Omega}}\sigma_{\mathrm{a}}\xi_{\mathrm{a}}(t) \\
+\beta\left\{1 + \frac{1}{\sqrt{\Delta\Omega}}\sigma_{\mathrm{m}}\xi_{\mathrm{m}}(t)\right\}\cos^2(x_T+\phi)
\end{aligned}
\tag{7.1}
$$

where σ_{a} and σ_{m} are the dimensionless additive and multiplicative noise amplitudes. The normalized Gaussian white noise terms $\xi_{\mathrm{a}}(t)$ and $\xi_{\mathrm{m}}(t)$ $[1/s^{1/2}]$ have auto-correlations of $\langle\xi_{\mathrm{a,m}}(t)\xi_{\mathrm{a,m}}(t')\rangle = \delta(t-t')$ and a cross-correlation of $\langle\xi_{\mathrm{a}}(t)\xi_{\mathrm{m}}(t')\rangle = 0$. It is important to highlight that we employ the same definitions for the noise sources as in Chapter 6. Consequently, upon deriving the envelope equation from Eq. (7.1), the outcome will align with Eq. (6.4). Again, we have scaled the noise amplitudes to the bandwidth with the prefactor $\sqrt{1/\Delta\Omega}$ so that $\sigma_{\mathrm{a,m}}$ can remain dimensionless.

The difference between the sub- and above-threshold analyses should be highlighted here. The significance of this work lies in the quantification of the noise sources in the sub-threshold regime so that we can comprehend the origins of the noise before the sources are nonlinearly mixed with the signal. Therefore, the multiplicative contribution has been assumed to be white, whereas it exhibits different characteristics in the above-threshold [64–66]. As shown in Chapter 6, in order to define the multiplicative noise in the above-threshold regime, we should consider the colored noise induced by the RFAs, the low-frequency laser RIN generated at the PD due to the conversion of the intensity noise into phase noise, and the optical frequency noise caused by dispersion in the FDL. These are frequency-dependent and approximated as flicker. So, comparing this work with the above-threshold analyses can help us to understand the formation of the frequency-dependent noise at the threshold gain. We can also track the variation of the additive noise by comparing the two analyses. In both regimes, the additive noise can be described as the thermal noise of the electronic path, the laser RIN at the oscillation frequency, and the shot noise at the detector. In the case of the RIN and shot noise, their magnitudes directly depend on currents, and thus, they may fluctuate as the system transits from the small and large-signal regime, which can be identified through the comparison.

Considering that the trivial solution remains stable below the threshold gain, Eq. (7.1) can be further simplified. The square of the cosine term can be expanded through a Taylor series, but we limit our consideration to the first-order terms. This is because higher-order terms have negligible impact on the dynamics. Consequently, the time-delayed term is considered trivial and disregarded in the regime. Taking into account these considerations and defining the integration term as $y(t) = (\Omega_0^2/\Delta\Omega)\int_{t_0}^{t} x(s)\,ds$, the stochastic equation can be reformulated as a set of coupled equations:

$$\frac{dx}{dt} = -\Delta\Omega(x+y) + \sqrt{\Delta\Omega}\sigma_{\mathrm{a}}\xi_{\mathrm{a}}(t) + \sqrt{\Delta\Omega}\frac{\beta}{2}\sigma_{\mathrm{m}}\xi_{\mathrm{m}}(t) \tag{7.2}$$

$$\frac{dy}{dt} = \frac{\Omega_0^2}{\Delta\Omega}x \tag{7.3}$$

where we operate the modulator at the QTP for the loop gain maximization and neglect the DC-related terms as they are filtered out.

To further simplify, we introduce a dimensionless time variable, $\tau = \Delta\Omega \cdot t$, giving rise to $d\tau = \Delta\Omega \cdot dt$. Considering the stochastic terms defined as $\langle \xi_{\mathrm{a,m}}(t)\xi_{\mathrm{a,m}}(t') \rangle = \delta(t - t')$, we express them in terms of τ using the delta-function property $\delta(ax) = \delta(x)/|a|$, yielding $\delta(t-t') = \Delta\Omega\delta(\tau - \tau')$. Defining the Gaussian white noise in the dimensionless time-domain as $\zeta(\tau)$, we establish a relationship between their auto-correlations: $\langle \zeta(\tau)\zeta(\tau') \rangle = \langle \xi(t)\xi(t') \rangle / \Delta\Omega$. This relation ultimately leads to $\zeta(\tau) = (1/\sqrt{\Delta\Omega})\xi(t)$ and consequently, the coupled stochastic equations presented in Eqs. (7.2) and (7.3) can be transformed into

$$\dot{x} = -x - y + \sigma_{\mathrm{a}}\zeta_{\mathrm{a}}(\tau) + \frac{\beta}{2}\sigma_{\mathrm{m}}\zeta_{\mathrm{m}}(\tau) \tag{7.4}$$

$$\dot{y} = Q^2 x \tag{7.5}$$

where the upper dots denote derivative in terms of τ, namely $\dot{x} = dx/d\tau$ and $\dot{y} = dy/d\tau$.

7.2.2 Derivation of the Noise Contributions

We now define the noisy RF output as a function of the two noise contributions. Initially, we can employ Ohm's formula to describe RF powers as follow:

$$\overline{P}(\beta) = \frac{\langle V^2(t) \rangle}{2R_{\mathrm{out}}} = \left(\frac{2V_{\pi\mathrm{RF}}}{\pi}\right)^2 \frac{\langle x^2(\tau) \rangle}{2R_{\mathrm{out}}} \tag{7.6}$$

where the brackets represent the averages of the functions in their domains. Then, it is no longer a function of time, but is a function of β.

In order to express the right-hand side as a function of β, we use Parseval's theorem, given by

$$\langle x^2(\tau) \rangle = \frac{1}{2\pi} \int_{-\infty}^{\infty} |\tilde{X}(i\omega)|^2 d\omega, \tag{7.7}$$

where $\tilde{X}(i\omega)$ is the Fourier transform of $x(\tau)$ which can be obtained from Eqs. (7.4) and (7.5) as

$$\tilde{X}(i\omega) = \frac{\sigma_{\mathrm{a}}\tilde{\zeta}_{\mathrm{a}}(i\omega) + (\beta/2)\sigma_{\mathrm{m}}\tilde{\zeta}_{\mathrm{m}}(i\omega)}{1 + i\omega(1 - Q^2/\omega^2)}. \tag{7.8}$$

In the Fourier domain, $\tilde{\zeta}_{\mathrm{a}}(i\omega)$ and $\tilde{\zeta}_{\mathrm{m}}(i\omega)$ represent the Fourier transform of the additive and multiplicative noise where they are auto-correlated, $|\tilde{\zeta}_{\mathrm{a,m}}(i\omega)|^2 = 1$, and not cross-correlated $\int_{-\infty}^{\infty} \tilde{\zeta}_{\mathrm{a}}^*(i\omega)\tilde{\zeta}_{\mathrm{m}}(i\omega) d\omega = 0$.

The integration obtained from equating Eq. (7.8) into Eq. (7.7) can indeed be simplified by using the property below:

$$I = \int_{-\infty}^{\infty} \frac{\omega^2}{\omega^4 + (1 - 2Q^2)\omega^2 + Q^4} d\omega = \pi \tag{7.9}$$

which indicates that the integration is independent of Q. Consequently, we can convert Eq. (7.6) as follows

$$\overline{P}(\beta) = \left(\frac{2V_{\pi\mathrm{RF}}}{\pi}\right)^2 \frac{(\beta^2\sigma_{\mathrm{m}}^2/4 + \sigma_{\mathrm{a}}^2)}{4R_{\mathrm{out}}}. \tag{7.10}$$

This expression enables one to determine the power of the stochastic output of the OEO under the threshold as an explicit function of the additive and multiplicative noise powers.

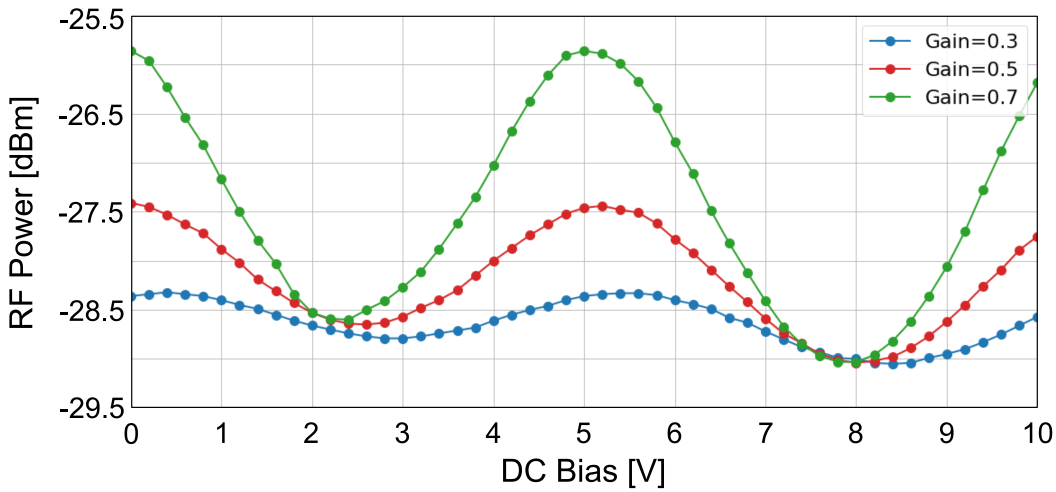

Figure 7.2: Variation in RF noise power for the $Q = 0.52$ filter setup as a function of the DC bias applied to the modulator. The laser power is set at 16 dBm, and three distinct gain parameters, namely $\beta = 0.3$, 0.5, and 0.7, are achieved by adjusting the VOA. For $\beta = 0.3$, the *optical* output power of the modulator is minimized at approximately 8.6 V input, maximized around 2.8 V, with a 5.8 V gap approximately corresponding to the DC halfwave voltage of the modulator $V_{\pi\mathrm{DC}} = 6$ V. Additionally, the output power of the modulator is halved near 5 V, marking the QTP where the *RF power* reaches its maximum.

An important baseline for our analysis is the stochastic power in the open-loop configuration, that is, when $\beta = 0$. The value of $\overline{P}(0)$ can be determined either theoretically and experimentally. One can use theory of quantum electronics to obtain an approximated value following

$$\overline{P}(0) \simeq \frac{1}{4\pi}[FkT_0 + 2eI_{\mathrm{ph}}R_{\mathrm{eq}}]G\Delta\Omega \tag{7.11}$$

where k is the Boltzmann constant, T_0 represents the temperature, e is the electron charge, I_{ph} represents the current to the PD, R_{eq} is the equivalent resistance, and F is the noise figure of the first amplifier [35]. The first and second terms express the thermal and shot noise, and there is no laser RIN as the laser is turned off.

The expression of σ_{a}^2 can be obtained by plugging $\beta = 0$ into Eq. (7.10) as

$$\sigma_{\mathrm{a}}^2 = 4R_{\mathrm{out}}\overline{P}(0)\left(\frac{\pi}{2V_{\pi\mathrm{RF}}}\right)^2. \tag{7.12}$$

Subsequently, it is possible to quantify σ_{a}^2 using $\overline{P}(0)$, which can be either obtained by Eq. (7.11) or measured experimentally.

Once σ_{a}^2 is known, it is possible to quantify σ_{m}^2. Using Eq. (7.10), the multiplicative noise can be obtained as follows:

$$\sigma_{\mathrm{m}}^2 = \left[4R_{\mathrm{out}}\overline{P}(\beta)\left(\frac{\pi}{2V_{\pi\mathrm{RF}}}\right)^2 - \sigma_{\mathrm{a}}^2\right]\frac{4}{\beta^2}. \tag{7.13}$$

This procedure requires to experimentally measure $\overline{P}(\beta)$. In principle, one would mathematically expect σ_{m}^2 to be gain-dependent (i.e., a function of β), but as evidenced below the experimental measurements indicate instead that is constant over a broad range of values.

7.3 Results and Discussion

7.3.1 Workflow

The workflow unfolds as follows: initially, we identify the threshold point at which the oscillatory solution becomes stable, where $\beta = 1$. The gain is varied experimentally using the VOA, while the power of the laser source remains fixed. We measure three optical power cases for respective filter setups, and the feedback gain parameter is tuned by the attenuator. The associated insertion loss of components is calculated as -15.5 dB. Subsequently, we *experimentally* measure

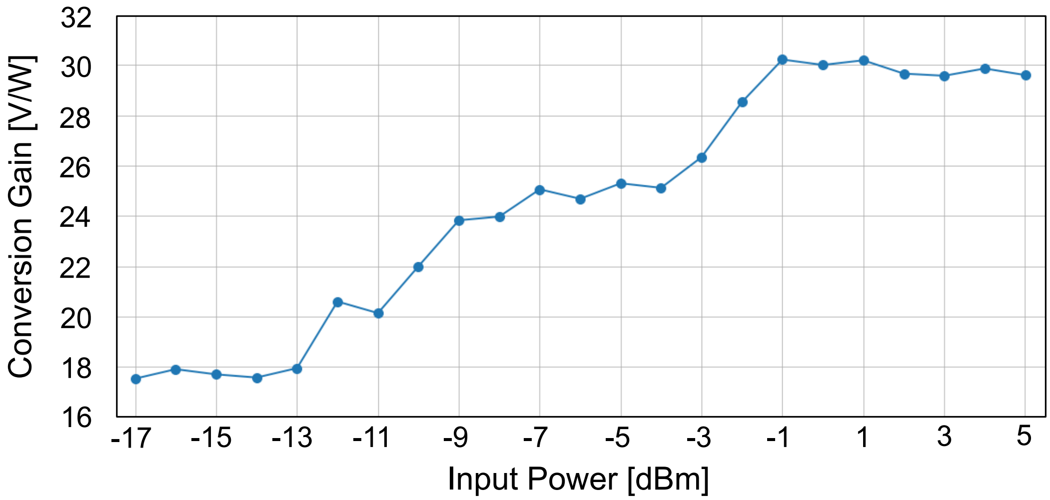

Figure 7.3: Characterization of the PD near the power budget of the setup. The conversion gain is approximately 30 V/W above -1 dBm input power and 18 V/W below -13 dBm input power, with variation within -13 dBm and -1 dBm range, which corresponds to our power budget.

$\overline{P}(0)$ by deactivating the laser source and $\overline{P}(\beta)$ by adjusting the attenuator respectively. Based on the outcomes, we can *analytically* compute the values of σ_{a} and σ_{m} of the setups. To validate these findings, we reintegrate the computed σ_{a} and σ_{m} back into Eq. (7.4), enabling us to *numerically* compute $\overline{P}(0)$ and $\overline{P}(\beta)$. The subsequent comparison of these numerical results with the experimental measurements serves as the final step in verifying the accuracy of our analytical predictions.

7.3.2 Experimental Setup

The laser (IDPhotonics CoBrite-DX2) operates at 1550 nm, and power levels of 14 dBm, 15 dBm, and 16 dBm are employed to demonstrate that this active component does not induce significant noise changes as long as β remains constant. The feedback gain parameter can stay at the same by inducing more attenuation at different optical power levels. The optical signal is introduced into the 10 GHz MZM (IXblue MX-LN-10-PD-P-P-FA-FA) characterized

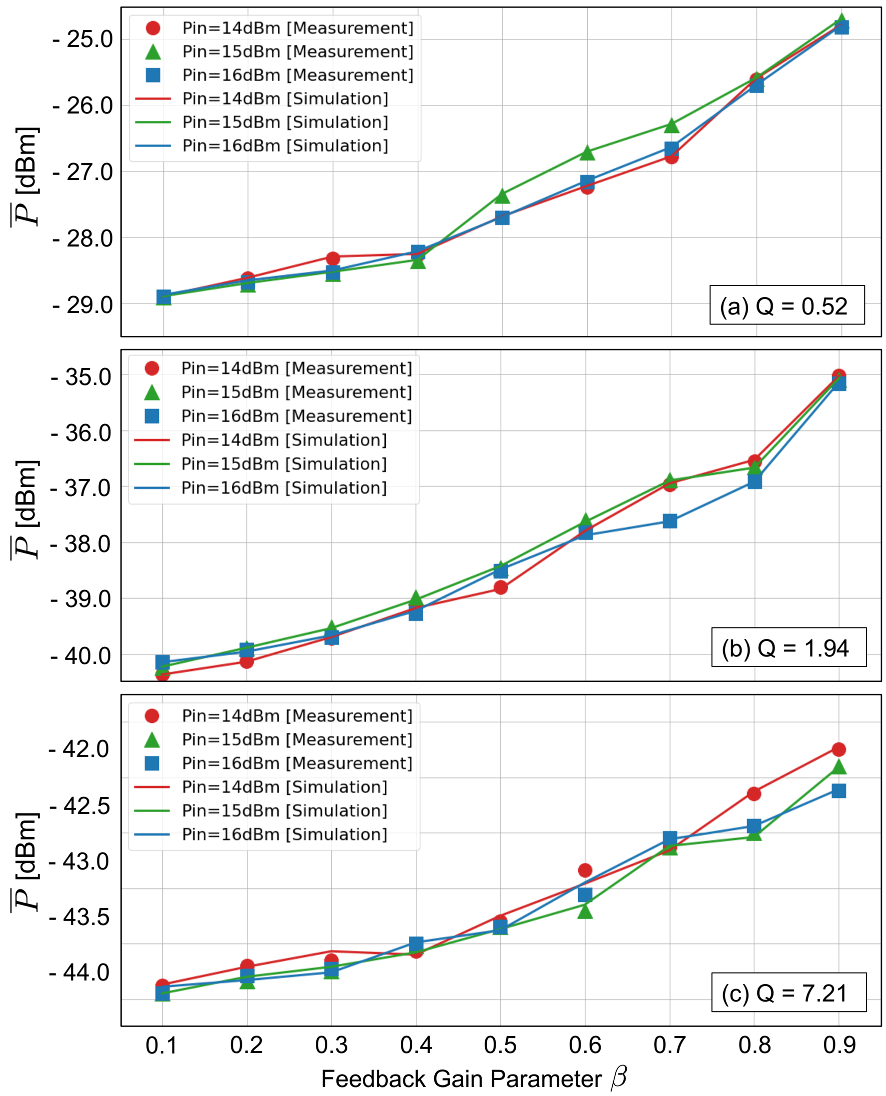

Figure 7.4: Variations in experimental and analytical RF output powers with the feedback gain parameter β below the threshold. In parts (a), (b), and (c), we examine the cases with $Q = 0.52$, 1.94, and 7.21 respectively, considering the three different optical powers: 14 (in red), 15 (in green), and 16 dBm (in blue). The straight lines represent analytical solutions obtained through numerical simulations by using the calculated multiplicative and additive noise contribution magnitudes while the red circles, green triangles and blue squares represent the measured data of the three power level cases. In order to obtain the simulation results, we used the calculated σ values from Eqs. (7.12) and (7.13), obtained as $\sigma_\mathrm{a} = 4.527 \times 10^{-3}$, 1.218×10^{-3}, and $\sigma_\mathrm{a} = 8.068 \times 10^{-4}$ for the broad, intermediate, and narrow cases. The calculated σ_m values for each gain are depicted in Fig. 7.5, and the corresponding values were used for the simulations.

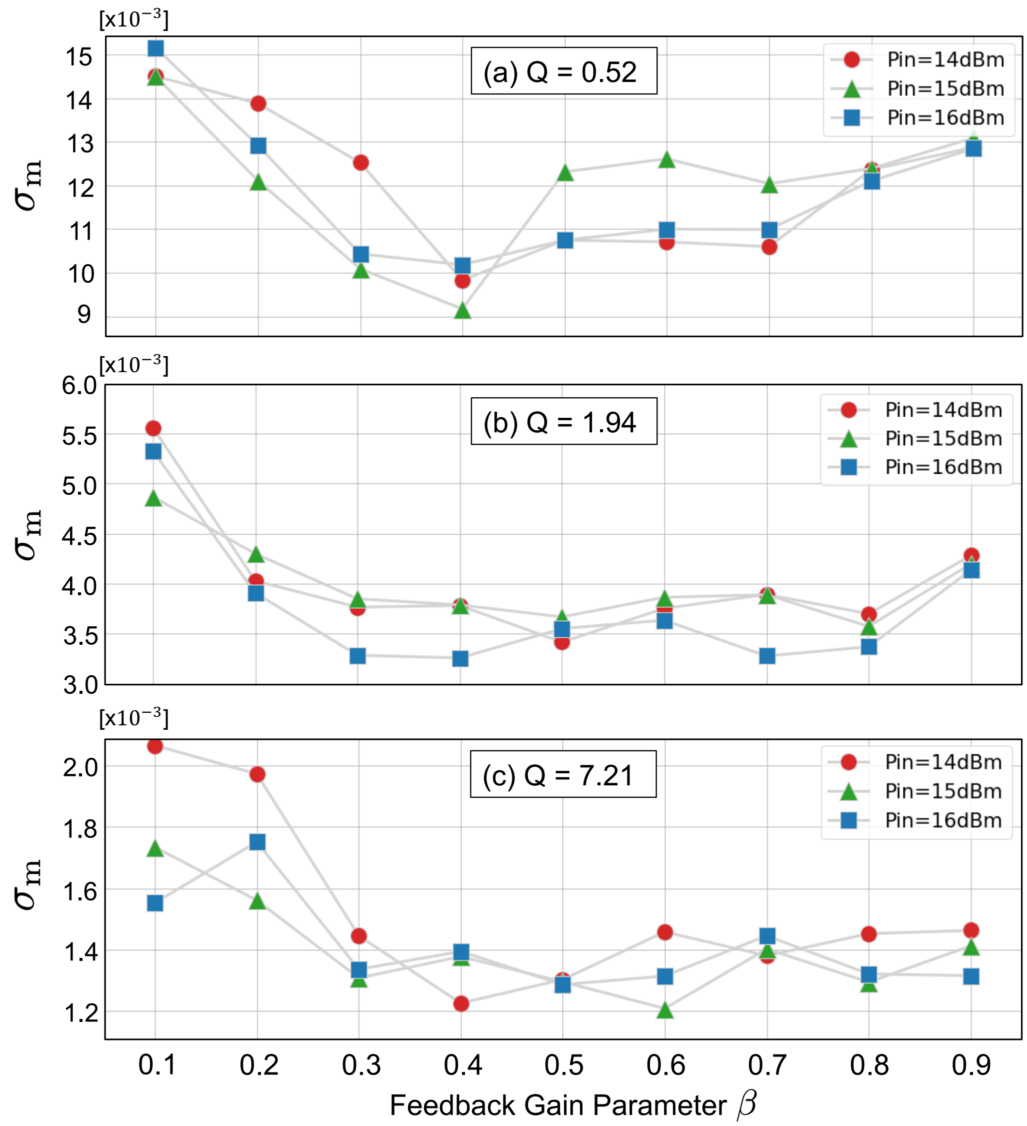

Figure 7.5: Variations in multiplicative noise contributions with the feedback gain parameter β below the threshold. In parts (a), (b), and (c), we examine the cases with $Q = 0.52, 1.94$, and 7.21 respectively, considering three different optical powers: 14 (in red), 15 (in green), and 16 dBm (in blue). It is worth noting that $\sigma_{\rm m}$'s exhibit a rapid decrease at very low gains, after which it stabilizes at nearly the same value as the gain increases. This behavior becomes more pronounced at higher Q-values. Furthermore, it is evident that the noise contributions remain consistent across the different optical power levels since they share the same gain control through the VOA.

by $V_{\pi\mathrm{RF}} = 5.5$ V and $V_{\pi\mathrm{DC}} = 6$ V. The FDL is 4.4 km long, resulting in a time-delay of 22 μs. It is important to acknowledge the potential impact of the length of the delay line, as it can cause wavelength fluctuations and deteriorate the phase noise performance through chromatic dispersion, but this work uses one delay length as the length-dependent noise can be lumped into our phenomenological noise sources [98].

To regulate β, the manually controlled VOA is inserted. Higher optical power levels require increased attenuation to ensure a uniform gain across the three optical power settings, resulting in an identical input to the detector for all cases. The 50 GHz high-speed PD (Finisar XPDV2120R-VF-FA) transforms the time-delayed optical signal into an RF signal. To compensate for loop losses, two RFAs with gains of $G_1 = 40.2$ dB (Mini-Circuits ZKL-1R5+) and $G_2 = 11.6$ dB (Mini-Circuits ZJL-7G+) are incorporated, with the first amplifier exhibiting a noise figure of 3 dB. The setup employs three different BPFs: a) Filter with parameters $\Omega_0 = 2\pi \times 510$ MHz, $\Delta\Omega = 2\pi \times 980$ MHz, and $Q \simeq 0.52$ (Mini-Circuits ZABP-510-S+) for the *broad* bandwidth. b) Filter with parameters $\Omega_0 = 2\pi \times 70$ MHz, $\Delta\Omega = 2\pi \times 36$ MHz, and $Q \simeq 1.94$ (Mini-Circuits ZX75BP-B70-S+) for the *intermediate* bandwidth. c) Filter with parameters $\Omega_0 = 2\pi \times 101$ MHz, $\Delta\Omega = 2\pi \times 14$ MHz, and $Q \simeq 7.21$ (Mini-Circuits SBP-101+) for the *narrow* bandwidth. These designations help to compare their relative Q-values. The RF power of the setup is measured using the RF power meter (Keysight V3500A).

7.3.3 Variation in Output RF Noise Power with the DC Bias (Transmission Point) of the Modulator

Although this work operates the setup at the QTP for noise measurement, it is valuable to explore the dynamics of the setup at various transmission points to get a deeper insight into the additive and multiplicative noise. The output powers of the modulator in different voltages and gains are depicted in Fig. 7.2. For $\beta = 0.3$ measurement, the *optical* output power of the modulator is minimized at approximately 8.6 V input, maximized around 2.8 V where a 5.8 V gap corresponds to the DC halfwave voltage of the modulator $V_{\pi\mathrm{DC}} = 6$ V. Additionally, the output power of the modulator is halved near 5.6 V, indicating it is the QTP where the *RF power* reaches its maximum. The measurements were performed sequentially with β values of 0.3, 0.5, and 0.7. It is also shown that the overall curve shifts leftward as the measurements progress, starting with $\beta = 0.3$ and concluding with $\beta = 0.7$ is measure last. This is attributed to the fact that the transmission curves of modulators tend to shift leftward or rightward as the modulator is heated up. No bias controller was used during these measurements to delicately control the transmission point.

Based on the definition of Jacobi-Anger expansion [63], one might expect the output power at the MATP should be equivalent to the output power at the MITP. However, Fig. 7.2 presents a slight difference between them, and to understand this point, we should do characterization of the PD. The experimental characterization of the PD is shown in Fig. 7.3. In our measurements, the input power to the PD is in between -13 dBm and -1 dBm at the MATP, and it is presented that the conversion gain is not a constant in the power budget, which needs to be accounted for when calculating the feedback gain parameter. However, at the MATP, the power budget is still at the above the threshold of the detector.

The input power to the PD at the MITP is less than -30 dBm. However, the detector hardly detects powers below -17 dBm, and it indicates that the range is below the threshold of the PD. Consequently, the power at the MITP corresponds to the zero input power, $\overline{P}(0)$. Therefore, the power gap between at the MITP and the QTP in Fig. 7.2 is related to the multiplicative noise contribution, as defined in Eq. (7.13).

7.3.4 Quantifying the Additive Noise Contribution

By turning off the laser, $\overline{P}(0)$ values are measured as follows: -29.01 dBm for the broad case, -40.41 dBm for the intermediate case, and -43.99 dBm for the narrow case. The values can also be analytically verified using Eq. (7.11) by taking into account the provided parameters, $T_0 = 295$ K, $I_{\text{ph}} \simeq 2$ mA, and $F = 3$ dB for the first amplifier. The errors between the experimental and analytical results fall within a range of ± 2 dB. Given the extremely low power levels under consideration, this level of error is regarded acceptable, accounting for measurement uncertainties stemming from the powermeter and temperature variations.

Utilizing Eq. (7.12), the additive noise contributions for the three setups are calculated as follows: $\sigma_{\text{a}} \simeq 4.527 \times 10^{-3}$ for the broad setup, $\sigma_{\text{a}} \simeq 1.218 \times 10^{-3}$ for the intermediate setup, and $\sigma_{\text{a}} \simeq 8.068 \times 10^{-4}$ for the narrow setup. It is important to note that to determine the actual magnitudes of the noise, we need to multiply σ_{a} by $\sqrt{1/\Delta\Omega}$, since this term was initially subtracted from σ_{a} to make the contributions dimensionless. Consequently, the effective magnitudes of the noise can be calculated using $\sigma_{\text{a}} \times \sqrt{1/\Delta\Omega}$ and the values are calculated approximately as: 5.769×10^{-8} s$^{1/2}$, 8.099×10^{-8} s$^{1/2}$, and 8.602×10^{-8} s$^{1/2}$ for the broad, intermediate, and narrow ones. In the configuration depicted in Fig. 7.1, the only difference among the three setups is the replacement of the filters, while all other components remain the same. Given the results, it is shown that the magnitudes of the three cases do not vary significantly, indicating that the noise effect from filters is relatively minimal. In addition, it is important to note that a larger bandwidth does not necessarily results in higher noise levels; the level of the center frequency also needs to be taken into consideration.

7.3.5 Quantifying the Multiplicative Noise Contribution

To quantify the multiplicative noise contributions, the RF powers are measured for the gains ranging from $\beta = 0.1$ to $\beta = 0.9$ at intervals of 0.1, as depicted by the red circles, blue squares, and red triangles in Fig. 7.4. Notably, the noise power increases as the linewidth of the filter broadens. Applying the measured powers and the values of the calculated σ_{a} into Eq. (7.13), the values of σ_{m} are calculated and presented in Fig. 7.5. It is valuable noting that σ_{m} displays a quick decrease at very low gains, followed by a stabilization at nearly the same value as the gain continues to increase below the threshold. This behavior becomes more pronounced at higher Q-values. Furthermore, it is evident that the noise contributions remain consistent across the different optical power levels, as they all share the same gain control through the VOA.

For the values of β greater than 0.3, the σ_{m} for the three cases can be approximated as follows: $\sigma_{\mathrm{m}} \simeq 11.9 \times 10^{-3}$ for the broad one, $\sigma_{\mathrm{m}} \simeq 3.92 \times 10^{-3}$, and $\sigma_{\mathrm{m}} \simeq 1.45 \times 10^{-3}$ for the narrow one. Then, we can determine the effective magnitude of these noise using $\sigma_{\mathrm{m}} \times \sqrt{1/\Delta\Omega}$ and the results are calculated approximately as follows: $1.517 \times 10^{-7}\ \mathrm{s}^{1/2}$, $2.606 \times 10^{-7}\ \mathrm{s}^{1/2}$, and $1.546 \times 10^{-7}\ \mathrm{s}^{1/2}$ for the broad, intermediate, and narrow setups. It is noteworthy that the magnitudes of the additive and multiplicative noise are comparable. Lastly, with the results of σ_{m} and σ_{a}, it is feasible to calculate the output power analytically through numerical simulation using Eqs. (7.4) and (7.5). The analytical results are represented as the solid lines in Fig. 7.4, demonstrating a high match with the experimental results.

One important fact is that we should focus on the actual noise magnitudes, $\sigma_{\mathrm{a,m}} \times \sqrt{1/\Delta\Omega}$, for comparing the magnitudes of the noise, not the measured powers as discussed. Although the noise magnitudes are linked to the powers, the increased powers do not necessarily imply increased noise, and it is imperative to consider that the power also depends on the bandwidth. Another perspective to comprehend is defining the noise contributions differently. In Eq. (7.1), we intentionally subtracted $\sqrt{1/\Delta\Omega}$ from $\sigma_{\mathrm{a,m}}$ to render them as dimensionless. However, if we choose not subtract, the right side of Eq (7.10) needs to be multiplied by $\Delta\Omega$ as we should replace $\sigma_{\mathrm{a,m}}$ by $\sigma_{\mathrm{a,m}} \times \sqrt{\Delta\Omega}$. This clearly highlights that power is contingent on both bandwidths and noise contributions.

7.4 Conclusion of the Chapter

The primary objective of this chapter was to quantify the additive and multiplicative noise contributions before the frequency-locking. We started from deriving the deterministic dynamic equation of the OEO and used Langevin approach by directly including the additive and multiplicative noise contributions into the deterministic form, similar to the approaches used in Chapter 6. However, the distinction from Chapter 6 was utilization of the real-valued signal in this chapter, instead of the complex envelope expression. This choice is made because there is no oscillating signal here, thus it is not necessary to consider the envelope expression, as it was due to the time-scale issue.

By using the obtained stochastic equation, we derived the equations for the additive and multiplicative noise. The additive noise is independent of the existence of actual oscillations, meaning it has no dependency on the gain parameter. Therefore, in order to quantify the additive noise, we measured the RF output powers by deactivating the laser source in the three filter setups. On the contrary, the multiplicative noise contribution is influenced by the noisy feedback gain parameter, making it a function of the gain. By manipulating the gain parameter through regulating the attenuator, we measured the output RF powers and calculated the associated multiplicative noise contributions. It was observed that these contributions remain at nearly constant values regardless of the increases of the gain parameters, despite quick decrease in the initial stage. However, it is important to note that as the noise contribution needs to be multiplied by the gain parameter to determine the ultimate noise magnitude, the impact of multiplicative noise becomes more substantial at higher powers.

Chapter 8: Conclusion

In Chapters 2, 3, and 4, we successfully derived the microwave envelope equations of the various OEOs where they used different approaches for frequency selections and conducted in-depth investigation into the significance of the dynamic equations. Based on the similarities between the envelope equations of the diverse OEOs, we derived the universal envelope equation in Chapter 5. We derived the universal microwave envelope equation based on the findings from the preceding sections and developed the models suitable for stability analysis. By employing these models, we conducted stability analyses of the OEOs, yielding the results consistent with those presented in earlier chapters and affirming the validity of the universal envelope equation. Crucially, the universal equation suggests that the dynamics of OEOs remain highly similar irrespective of their dynamical complexities. We also derived the universal envelope equation of the frequency-doubled setups so that it is also possible to open possibilities of researching the oscillating loop and separate output ports simultaneously.

The analysis of the universal envelope equation unveiled two distinct solutions: a trivial and an oscillatory solution, with their stabilities shift as the loop gain increases. Below the threshold gain, the trivial solution remains stable, and no oscillations manifest. The first bifurcation, known as the Hopf bifurcation, precisely occurs at the threshold gain, resulting in a switch in stability between the two solutions. In the interval from the threshold gain to the critical gain, the oscillatory solution remains stable, rendering this region optimal for pure microwave generation. The oscillatory solution is gain-dependent, with each gain in the region having its unique oscillatory solution. Moreover, it was demonstrated that different setups may exhibit different critical gains. Upon reaching the critical gain, the system undergoes the second bifurcation, referred to as the secondary Hopf bifurcation or the Neimark-Sacker bifurcation. Following the bifurcation, the amplitude modulations emerge, with the results present $2T$ and $4T$ periodicity. However, further increasing gain leads to the chaotic dynamics, where no clear amplitude modulation is observed.

The significance of Chapter 5 lies in the revelation that the universal envelope equation highlights the dynamic similarities among OEOs regardless of their complexities. This implies that dynamical behavior observed in one setup may be mirrored in others, facilitating interpretations or analyses applicable across different setups. For example, insights gained from a thorough investigation of the fundamental setup can be extrapolated to other OEOs, while the universal equation can serve as a pathway for such transfer of the knowledge.

In Chapters 6 and 7, we investigate the phase dynamics of OEOs. To explore the oscillators, we discern between two types of noise in the oscillators: the additive noise and the multiplicative noise. The additive noise contribution is attributed to the environmental and random fluctuations while the multiplicative noise is due to the noisy loop gain. Both contributions are directly incorporated into the deterministic equations for further analyses. In both chapters, we considered the fundamental setup only due to its simplicity and we learned that interpretations towards a specific OEO can be applicable to other OEOs in different configurations because of the universality between OEOs. However, the multiplicative noise exhibits different characteristics in the above-threshold and sub-threshold regimes, as its contribution is influenced by the presence of signals.

In Chapter 6, we examined the above-threshold regime where the multiplicative noise is nonlinearly mixed with the oscillating signals. Here, we converted the deterministic universal microwave envelope equation into a stochastic form that describes the phase dynamics, in the form of a SDDE. During the derivation of the phase equation, we directly integrated the two noise contributions into the deterministic envelope equation. With the phase equation established, we proceeded to derive the power spectral density of the phase, offering valuable insights into the phase noise spectrum of OEOs. We conducted thorough theoretical and numerical investigations of the spectrum, revealing a significant level of agreement between two results. This alignment serves to validate the theoretical expression for the phase noise spectrum.

In contrast, in Chapter 7, the primary objective was to quantify the additive and multiplicative noise contributions before the frequency-locking. We started from deriving the deterministic dynamic equation of the OEO and used Langevin approach by directly including the additive and multiplicative noise contributions into the deterministic form, akin to the methodologies used employed in Chapter 6. However, the distinction from Chapter 6 was utilization of the real-valued signal in this chapter, instead of the complex envelope expression. This choice is made because there is no oscillating signal here, thus it is not necessary to consider the envelope expression, as it was due to the time-scale issue.

Using the derived stochastic equation, we formulated the equations for the additive and multiplicative noise. The additive noise is independent of the existence of actual oscillations, meaning it has no dependency on the gain parameter. Thus, to quantify the additive noise, we measured the RF output powers by deactivating the laser source across the three setups. Conversely, the multiplicative noise contribution is influenced by the noisy feedback gain parameter, rendering it a function of the gain. By manipulating the gain parameter through regulating the attenuator, we measured the output RF powers and calculated the associated multiplicative noise contributions. It was observed that these contributions remain at nearly constant values regardless of the increases of the gain parameters, despite quick decrease in the initial stage. However, it is crucial to note that while the impact of multiplicative noise remains relatively constant regardless of gain parameter increases, its significance becomes more pronounced at higher powers, as the noise contribution needs to be multiplied by the gain parameter to determine the ultimate noise magnitude.

The contents of Chapter 3 are published in [63], Chapter 4 in [99], Chapter 5 in [63, 96], Chapter 7 in [100].

Bibliography

[1] J. Capmany and D. Novak, ”Microwave photonics combines two worlds,” *Nature Photon.*, vol. 1, pp.319-330, Jun. 2007, doi:10.1038/nphoton.2007.89.

[2] L. Maleki, “The optoelectronic oscillator,” *Nature Photon*. vol. 5, no. 12, pp. 728–730 2011, doi: 10.1038/nphoton.2011.293.

[3] Y. K. Chembo, D. Brunner, M. Jacquot, and L. Larger, ”Optoelectronic oscillators with time-delayed feedback,” *Rev. Mod. Phys.*, vol. 91, pp. 035006, Jul.-Sep. 2019, doi: 10.1103/RevModPhys.91.035006.

[4] T. Hao, Y. Liu, K. Tang, Q. Cen, W. Li, N. Zhu, Y. Dai, J. Capmany, J. Yao, and M. Lia, ”Recent advances in optoelectronic oscillators,” *Advanced Photonics*, vol. 2 no. 4, pp. 044001, Jul. 2020, doi: 10.1117/1.AP.2.4.044001.

[5] X. S. Yao and L. Maleki, ”High frequency optical subcarrier generator,” *Electron. Lett.*, vol. 30, no. 18, pp. 1525–1526, Apr. 1994, doi: 10.1049/el:19941033.

[6] X. S. Yao and L. Maleki, ”Optoelectronic oscillator for photonic systems,” *IEEE J. Quant. Electron.*, vol. 32, no. 7, pp. 1141–1149, Jul. 1996, doi: 10.1109/3.517013.

[7] X. S. Yao and L. Maleki, ”Microwave Optoelectronic Oscillator,” *J. Opt. Soc. Am. B*, vol. 13, no. 8, pp. 1725-1735, Aug. 1996, doi: 10.1364/JOSAB.13.001725.

[8] J.-P. Goedgebuer, L. Larger, and H. Porte, ”Optical cryptosystem based on synchronization of hyperchaos generated by a delayed feedback tunable laser diode,” *Phys. Rev. Lett.*, vol. 80, no. 10, Mar. 1998, doi: 10.1103/PhysRevLett.80.2249.

[9] L. Larger, J.-P. Goedgebuer, and F. Delorme, ”Optical encryption system using hyperchaos generated by an optoelectronic wavelength oscillator,” *Phys. Rev. E*, vol. 57, no. 7, Jun. 1998, doi: 10.1103/PhysRevE.57.6618.

[10] Y. K. Chembo, P. Colet, L. Larger, and N. Gastaud, ”Chaotic breathers in delayed electro-optical systems,” *Phys. Rev. Lett.*, vol. 95, no. 20, Nov. 2005, doi: 10.1103/PhysRevLett.95.203903.

[11] G. Tanaka, T. Yamane, J. B. Heroux, R. Nakane, N. Kanazawa, S. Takeda, H. Numata, D. Nakano, and A. Hirose ”Recent advances in physical reservoir computing: A review,” *Neural Network*, vol. 115, pp. 100-123, Mar. 2019, doi: 10.1016/j.neunet.2019.03.005.

[12] Y. K. Chembo, ”Machine learning based on reservoir computing with time-delayed optoelectronic and photonic systems,” *Chaos: An Interdisciplinary J. Nonlinear Sci.*, vol. 30, no. 1, pp. 013111–013121, doi: 10.1063/1.5120788.

[13] Y. Jin, Q. Zhao, H. Yin, and H. Yue, ”Handwritten numeral recognition utilizing reservoir computing subject to optoelectronic feedback,” *2015 11th Inter. Conf. on Natural Comp. (ICNC)*, doi: 10.1109/ICNC.2015.7378156.

[14] J. Qin, Q. Zhao, H. Yin, Y. Jin, and C. Liu, ”Numerical simulation and experiment on optical packet header recognition utilizing reservoir computing based on optoelectronic feedback,” *IEEE Photon. J.*, vol. 9, no. 1, Feb. 2017, doi: 10.1109/JPHOT.2017.2658028.

[15] Z. Xue, S. Li, X. Xue, X. Zheng, and B. Zhou, ”Photonics-assisted joint radar and communication system based on an optoelectronic oscillator,” *Opt. Express*, vol. 29, no.14, pp. 22442-22454, Jun. 2021, doi: 10.1364/OE.430910.

[16] Z. Ge, T. Hao, J. Capmany,W. Li, N. Zhu, and M. Li, “Broadband random optoelectronic oscillator,” *Nature Commun.*, vol. 11, no. 1, pp. 5724, Nov. 2020, doi: 10.1038/s41467-020-19596-x.

[17] X. S. Yao and G. Lutes, ”A high-speed photonic clock and carrier recovery device,” *IEEE Photon. Tech. Lett.*, vol. 8, no. 5, pp. 688-690, May 1996, doi: 10.1109/68.491596.

[18] T. Hao, Q. Cen, S. Guan, W. Li, Y. Dai, N. Zhu, and M. Li, ”Optoelectronic parametric oscillator,” *Nature Light. Sci. Appl.* vol. 9, no. 1, pp. 102 Jun. 2020, doi: 10.1038/s41377-020-0337-5.

[19] W. Li, W. T. Wang, W. H. Sun, L. X. Wang, J. G. Liu, and N. H. Zhu, ”Generation of flat optical frequency comb using a single polarization modulator and a Brillouin-assisted power equalizer,” *IEEE Photon. J.*, vol. 6, no.2, Apr. 2024, doi: 10.1109/JPHOT.2014.2311455.

[20] X. Xie, T. Sun, H. Peng, C. Zhang, P. Guo, L. Zhu, W. Hu, and Z. Chen, ”Low-noise and broadband optical frequency comb generation based on an optoelectronic oscillator,” *Opt. Lett.*, vol. 39, no. 4, pp. 785-788, Feb. 2014, doi: 10.1364/OL.39.000785.

[21] X. S. Yao, L. Maleki, Y. Ji, G. Lutes, and M. Tu, ”Dual-loop opto-electronic oscillator,” *IEEE Inter. Freq. Cont. Sym.*, pp. 545-549, 1998, doi: 10.1109/FREQ.1998.717952.

[22] X. S. Yao and L. Maleki, ”Multiloop optoelectronic oscillator,” *IEEE J. Quant. Electron.*, vol. 36, no. 1, Jan. 2000, doi:10.1109/3.817641.

[23] D. Eliyahu and L. Maleki, ”Low phase noise and spurious level in multi-loop opto-electronic oscillators,” *IEEE Inter. Freq. Cont. Sym.*, pp. 405-410, 2003, doi: 10.1109/FREQ.2003.1275126.

[24] A. Coillet, R. Henriet, P. Salzenstein, K. P. Huy, L. Larger, and Y. K. Chembo, ”Time-domain dynamics and stability analysis of optoelectronic oscillators based on whispering-gallery mode resonators,” *IEEE J. Quant. Electron.*, vol. 19, no. 5, Sep.-Oct. 2013, doi: 10.1109/JSTQE.2013.2252152.

[25] K. Saleh, G. Lin, and Y. K. Chembo, ”Effect of laser coupling and active stabilization on the phase noise performance of optoelectronic microwave oscillators based on whispering-gallery-mode resonators,” *IEEE Photon. J.*, vol. 7, no. 1, Feb. 2015, doi: 10.1109/JPHOT.2014.2381661.

[26] K. Saleh and Y.K. Chembo, ”Phase noise performance comparison between microwaves generated with Kerr optical frequency combs and optoelectronic oscillators,” *Electron. Lett.*, pp. 264-266, Feb. 2017, doi: 10.1049/el.2016.3160.

[27] J. Zhang and J. Yao, ”Parity-time–symmetric optoelectronic oscillator,” *Sci. Adv.*, vol. 4, no. 6, Jun. 2018, doi: 10.1126/sciadv.aar6782.

[28] M. Li, L. Li, R. Cao, J. Zhang, and J. Yao, ”Optoelectronic oscillator with improved sidemode suppression by joint use of spectral Vernier effect and parity-time symmetry,” *Opt. Exp.*, vol. 30, no. 16, pp. 28774-28782, Jul. 2022, doi: 10.1364/OE.460524.

[29] Y. Liu, T. Hao, W. Li, J. Capmany, N. Zhu, and M. Li, ”Observation of parity-time symmetry in microwave photonics,” *Light: Sci. App.*, vol. 7, no. 18, Jul. 2018, doi: 10.1038/s41377-018-0035-8.

[30] Y. K. Chembo, M. Jacquot, J. M. Dudley, and L. Larger, ”Ikeda-like chaos on a dynamically filtered supercontinuum light source,” *Phys. Rev. A*, vol. 94, no. 2, pp. 023847, Aug. 2016, doi: 10.1103/PhysRevA.94.023847.

[31] G. R. G. Chengui, P. Woafo, and Y. K. Chembo, ”The simplest laser-based optoelectronic oscillator: an experimental and theoretical study,” *IEEE J. Light. tech.*, vol. 34, no. 3, pp. 873-878, Feb. 2016, doi: 10.1109/JLT.2015.2508784.

[32] Y. K. Chembo, L. Larger, H. Tavernier, R. Bendoula, E. Rubiola, and P. Colet, ”Dynamic instabilities of microwaves generated with optoelectronic oscillators,” *Opt. Lett.*, vol. 32, no. 17, pp. 2571-2573, Sep. 2007, doi: 10.1364/OL.32.002571.

[33] Y. K. Chembo, L. Larger, and P. Colet, ”Nonlinear dynamics and spectral stability of optoelectronic microwave oscillators,” *IEEE J. Quant. Electron.*, vol. 44, no. 9, pp. 858–866, Sep. 2008, doi: 10.1109/JQE.2008.925121.

[34] Y. K. Chembo, L. Larger, R. Bendoula, and P. Colet, ”Effects of gain and bandwidth on the multimode behavior of optoelectronic microwave oscillators,” *Opt. Express*, vol. 16, no. 12, pp. 9067–9072, Jun. 2008, doi: 10.1364/OE.16.009067.

[35] Y. K. Chembo, K. Volyanskiy, L. Larger, E. Rubiola, and P. Colet, ”Determination of phase noise spectra in optoelectronic microwave oscillators: a Langevin approach,” *IEEE J. Quant. Electron.* vol. 45, no. 2, pp. 178-186, Feb. 2009, doi: 10.1109/JQE.2008.2002666.

[36] A. B. Ustinov, A. A. Nikitin, V. V, Lebedev, A. A. Serebrennikov, A. V. Shamray, A. V. Kondrashov1, and B. A. Kalinikos, ”A low phase noise tunable microwave spin wave optoelectronic oscillator,” *J. Phys. Conf. Ser.* no. 1038, 2013, doi: 10.1088/1742-6596/1038/1/012033.

[37] D. Eliyahu, D. Seidel, and L. Maleki, ”Phase noise of a high performance OEO and an ultra low noise floor cross-correlation microwave photonic homodyne system,” *IEEE Inter. Freq. Cont. Sym.*, pp. 811-814, 2008, doi: 10.1109/FREQ.2008.4623111.

[38] Y. K. Chembo, A. Hmima, P.-A. Lacourt, L. Larger, and J. M. Dudley, ”Generation of ultralow jitter optical pulses using optoelectronic oscillators with time-lens Soliton-assisted compression,” *IEEE J. Light. tech.*, vol. 27, no. 22, pp. 5160-5167, Nov. 2009, doi: 10.1109/JLT.2009.2028033.

[39] M. Fleyer, A. Sherman, M. Horowitz, and M. Namer, ”Wideband-frequency tunable optoelectronic oscillator based on injection locking to an electronic oscillator,” *Opt. Lett.*, vol. 41, no. 9, pp. 1993-1996, Apr. 2016, doi: 10.1364/OL.41.001993.

[40] O. Okusaga, J. P. Cahill, A. Docherty, C. R. Menyuk, W. Zhou, and G. M. Carter, ”Suppression of Rayleigh-scattering-induced noise in OEOs,” *Opt. Express*. vol. 21, no. 19, pp. 22255-22262, Sep. 2013, doi: 10.1364/OE.21.022255.

[41] D. Zhu, S. Pan, and D. Ben, ”Tunable frequency-quadrupling dual-loop optoelectronic oscillator,” *IEEE Photon. Tech. Lett.*, vol. 24, no. 3, pp. 194–196, Feb. 2012, doi: 10.1109/LPT.2011.2176332.

[42] W. T. Wang, W. Li, and N. H. Zhu, ”Frequency quadrupling optoelectronic oscillator using a single polarization modulator in a Sagnac loop,” *Opt. Comm.*, vol. 318, pp. 162–165, May 2014, doi: 10.1016/j.optcom.2013.12.044.

[43] Y. Wang, Y. Shan, L. Pan, X. Wang, C. Meng, W. Dong, and X. Zhang, ”A tunable frequency-decuple optoelectronic oscillator based on frequency comb and stimulated brillouin scattering,” *Opt. Quant. Electron.*, vol. 49, no. 253, Jun. 2017, doi: 10.1007/s11082-017-1082-8.

[44] X. Xiao, S. Li, Z. Xie, S. Peng, D. Wu, X. Xue, X. Zheng, and B. Zhou, ”Photonic harmonic up-converter based on a self-oscillating optical frequency comb using a DP-DPMZM,” *Opt. Comm.*, vol. 413, pp. 48–53, Apr. 2018, doi: 10.1016/j.optcom.2017.12.001.

[45] A. Ly, V. Auroux, R. Khayatzadeh, N. Gutierrez, A. Fernandez, and O. Llopis, ”Highly spectrally pure 90-GHz signal synthesis using a coupled optoelectronic oscillator,” *IEEE Photon. Tech. Lett.*, vol. 30, no. 14, pp. 1313–1316, Jul. 2019, doi: 0.1109/LPT.2018.2845747.

[46] W. Li and J. Yao, ”An optically tunable optoelectronic oscillator,” *IEEE J. Light. Tech.*, vol. 28, no. 18, pp. 2640-2645, Sep. 2010, doi: 10.1109/JLT.2010.2058792.

[47] J. Zheng, W. Sun, W. Wang, Y. Tong, W.Y. Wang, X. Wang, H. Yuan, J. Liu, and N. Zhu, ”Frequency-doubling OEO using the polarization property of LiNbO3 modulator,” *IEEE Photon. Tech. Lett.*, vol. 27, no. 17, pp. 1864-1867, Sep. 2015, doi: 10.1109/LPT.2015.2443974.

[48] L. Wang, N. Zhu, W. Li, and J. Liu, ”A frequency-doubling optoelectronic oscillator based on a dual-parallel Mach–Zehnder modulator and a chirped fiber nragg grating,” *IEEE Photon. Tech. Lett.*, vol. 23, no. 22, pp. 1688-1690, Nov. 2011, doi:10.1109/LPT.2011.2167141.

[49] S. Shang, A. Wen, Y. Gao, and W. Zhang, ”Tunable frequency-doubled optoelectronic oscillator based on a phase modulator in a Sagnac loop,” *Optik*, vol. 145, pp. 617–622, Sep. 2017, doi: 10.1016/j.ijleo.2017.08.009.

[50] Y. Chen, W. Li, A. Wen, and J. Yao ”Frequency-multiplying optoelectronic oscillator with a tunable multiplication factor,” *IEEE Trans. Microwave. Theo. Tech.*, vol. 61, no. 9, pp. 3479–3485, Aug. 2013, doi: 10.1109/TMTT.2013.2273756.

[51] J. D. Bull, N. A. Jaeger, H. Kato, M. Fairburn, A. Reid, and P. Ghanipour, ”40-GHz electro-optic polarization modulator for fiber optic communications systems,” *Proc. SPIE,* vol. 5577, pp. 133-143, Dec. 2004, doi: 10.1117/12.567640.

[52] X. S. Yao, ”High-quality microwave signal generation by use of Brillouin scattering in optical fibers,” *Opt. Lett.*, vol. 22, no. 17, pp. 1329–1331, Sep. 1997, doi: 10.1364/ol.22.001329.

[53] B. Wu, M. Wang, J. Sun, B. Yin, H. Chen, T. Li, and S. Jian, ”Frequency- and phase-tunable optoelectronic oscillator based on a DPMZM and SBS effect,” *Opt. Comm.*, vol. 363, pp. 123–127, Mar. 2016, doi: 10.1016/j.optcom.2015.10.067.

[54] J. Liu, B. Zheng, and C. Shu, ”Self-oscillating optical frequency comb based on a Raman-pumped Brillouin optoelectronic oscillator,” *IEEE Photon. Tech. Lett.*, vol. 29, no. 12, pp. 1003–1006, Jun. 2017, doi: 10.1109/LPT.2017.2700895.

[55] G. Tong, T. Jin, H. Chi, X. Zhu, T. Lai, and X. Wu, ”A novel optoelectronic oscillator based on Brillouin-induced slow light effect,” *IEEE Photon. Tech. Lett.*, vol. 29, no. 16, pp. 1375–1378, Jul. 2017, doi: 10.1109/LPT.2017.2723158.

[56] J. Yao, ”Microwave photonics,” *J. Light. Tech.*, vol. 27, no. 3, pp. 314–335, Feb. 2009, doi: 10.1109/JLT.2008.2009551.

[57] J. Capmany, B. Ortega, and D. Pastor, ”A tutorial on microwave photonic filters,” *J. Light. Tech.*, vol. 24, no. 1, pp. 201-229, Jan. 2006, doi: 10.1109/JLT.2005.860478.

[58] W. Li and J. Yao, “A wideband frequency tunable optoelectronic oscillator incorporating a tunable microwave photonic filter based on phase-modulation to intensity-modulation conversion using a phase-shifted fiber Bragg grating,” *IEEE Trans. Micro. Theo. Tech.*, vol. 60, no. 6, pp. 1735–1742, Jun. 2012, doi: 10.1109/TMTT.2012.2189231.

[59] H. Peng, C. Zhang, X. Xie, T. Sun, P. Guo, X. Zhu, L. Zhu, W. Hu, and Z. Chen, ”Tunable DC-60 GHz RF generation utilizing a dual-loop optoelectronic oscillator based on stimulated Brillouin scattering,” *IEEE J. Light. Tech.*, vol. 33, no. 13, pp. 2707-2715, Jul. 2015, doi: 10.1109/JLT.2015.2403073.

[60] H. Peng, Y. Xu, X. Peng, X. Zhu, R. Guo, F. Chen, H. Du, Y. Chen, C. Zhang, L. Zhu, W. Hu, and Z. Chen, ”Wideband tunable optoelectronic oscillator based on the deamplification of stimulated Brillouin scattering,” *Opt. Express*, vol. 25, no. 9, pp. 10287-10305, May 2017, doi: 10.1364/OE.25.010287.

[61] M. Shi, L. Yi, W. Wei, and W. Hu, ”Generation and phase noise analysis of a wide optoelectronic oscillator with ultra-high resolution based on stimulated Brillouin scattering,” *Opt. Express*, vol. 26, no. 13, pp. 16113–16124, Jun. 2018, doi: 10.1364/OE.26.016113.

[62] M. Merklein, B. Stiller, I. V. Kabakova, U. S. Mutugala, K. Vu, S. J. Madden, B. J. Eggleton, and R. Slavik, ”Widely tunable, low phase noise microwave source based on a photonic chip,” *Opt. Lett.*, vol. 41, no. 20, pp. 4633-4636, Oct. 2016, doi: 10.1364/OL.41.004633.

[63] M. Ha and Y. K. Chembo, ”On the universality of microwave envelope equations for narrowband optoelectronic oscillators,” *IEEE J. Light. Tech.*, vol. 40, no. 18, pp. 6131-6138, Sep. 2022, doi: 10.1109/JLT.2022.3190695.

[64] S. Romisch, J. Kitching, E. Ferre-Pikal, L. Hollberg, and F.L. Walls, ”Performance evaluation of an optoelectronic oscillator,” *IEEE Trans. Ultra., Ferro., and Freq. Cont.*, vol. 47, no. 5, pp. 1159-1165, Sep. 2000, doi: 10.1109/58.869060.

[65] O. Lelièvre, V. Crozatier, P. Berger, G. Baili, O. Llopis, D. Dolfi, P. Nouchi, F. Goldfarb, F. Bretenaker, L. Morvan, and G. Pillet, ”A model for designing ultralow noise single- and dual-Loop 10-GHz optoelectronic oscillators,” *IEEE J. Light. Tech.*, vol. 35, no. 20, pp. 4366-4374, Oct. 2017, doi: 10.1109/JLT.2017.2729018.

[66] E. C. Levy, M. Horowitz, and C. R. Menyuk, ”Modeling optoelectronic oscillators,” *J. Opt. Soc. Am. B*, vol. 26, no. 1, pp. 148-159, Jan. 2009, doi: 10.1364/JOSAB.26.000148.

[67] T. Erneux, L. Larger, M. W. Lee, and J. -P. Goedgebuer, “Ikeda Hopf bifurcation revisited,” *Physica D*, vol. 194, pp. 49–64, Jan. 2004, doi: 10.1016/j.physd.2004.01.038.

[68] E. Rubiola, ”Phase noise and frequency stability in oscillators,” *Cambridge, U.K.: Cambridge Univ. Press*, 2008, doi: 10.1000/ISBN-13978-0-521-88677-2.

[69] J. Zheng, J. Wang, J. Yu, M. Zhu, Z. Dong, X. Wang, T. Su, J. Liu, N. Zhu, and G.K. Chang, ”Photonic microwave-signal-mixing technique using phase-coherent orthogonal optical carriers for radio-over-fiber application,” *Opt. Lett.*, vol. 39, no. 18, pp. 5263-5266, Sep. 2014, doi: 10.1364/OL.39.005263.

[70] G. K. Gopalakrishnan, W. K. Burns, R. W. McElhanon, C. H. Bulmer, and A. S. Greenblatt, ”Performance and modelling of broadband LiNbO3 traveling wave optical intensity modulators,” *IEEE J. Light. Tech.*, vol. 12, no. 10, pp. 1807–1818, Oct. 1994, doi: 10.1109/50.337494.

[71] S. Pan and J. Yao, ”A frequency-doubling optoelectronic oscillator using a polarization modulator,” *IEEE. Photon. Tech. Lett.*, vol. 21, no. 13, pp. 929-931, Jul. 2009, doi: 10.1109/LPT.2009.2020685.

[72] D. H. Chang, H. R. Fetterman, H. Erlig, H. Zhang, A. C. Oh, C. Zhang, and W. H. Steier, ”39-GHz optoelectronic oscillator using broad-band polymer electrooptic modulator,” *IEEE Photon. Tech. Lett.*, vol. 40, no. 2, pp. 191–193, Feb. 2002, doi: 10.1109/68.980509.

[73] T. Sakamoto, T. Kawanishi, and M. Izutsu, "Optoelectronic oscillator employing reciprocating optical modulator for millimetre-wave generation," *Electron. Lett.*, vol. 43, no. 19, pp. 1031–1033, Sep. 2007, doi: 10.1049/el:20071780.

[74] F. Van Dijk, A. Enard, X. Buet, F. Lelarge, and G.-H. Duan, "Phase noise reduction of a quantum dash mode-locked laser in a millimeter-wave coupled opto-electronic oscillator," *IEEE J. Light. Tech.*, vol. 26. no. 15, pp. 2789–2794, Aug. 2008, doi: 10.1109/JLT.2008.927608.

[75] M. Bagnell, J. Davila-Rodriguez, and P. J. Delfyett, "Millimeter-wave generation in an optoelectronic oscillator using an ultrahigh finesse etalon as a photonic filter," *J. Light. Tech.*, vol. 32, no. 6, pp. 1063–1067, Dec. 2013, doi: 10.1109/JLT.2013.2294944.

[76] D. Eliyahu, W. Liang, E. Dale, A. A. Savchenkov, V. S. Ilchenko, A. B. Matsko, D. Seidel, and L. Maleki, "Resonant widely tunable opto-electronic oscillator," *IEEE Photon. Tech. Lett.*, vol. 25, no. 15, pp. 1535–1538, Aug. 2013, doi: 10.1109/LPT.2013.2270913.

[77] X. Xie, C. Zhang, T. Sun, P. Guo, X. Zhu, L. Zhu, W. Hu, and Z. Chen, "Wideband tunable optoelectronic oscillator based on a phase modulator and a tunable optical filter," *Opt. Lett.*, vol. 38, no. 5, pp. 655–657, Mar. 2013, doi: 10.1364/OL.38.000655.

[78] W. Li, J. G. Liu, and N. H. Zhu, "A widely and continuously tunable frequency doubling optoelectronic oscillator," *IEEE Photon. Tech. Lett.*, vol. 27, no. 13, pp. 1461–1464, Jul. 2015, doi: 10.1109/LPT.2015.2425912.

[79] D. Lu, B. Pan, H. Chen, and L. Zhao, "Frequency-tunable optoelectronic oscillator using a dual-mode amplified feedback laser as an electrically controlled active microwave photonic filter," *Opt. Lett.*, vol. 40, no. 18, pp. 4340–4343, Sep. 2015, doi: 10.1364/OL.40.004340.

[80] B. Pan, D. Lu, L. Zhang, and L. Zhao, "A widely tunable optoelectronic oscillator based on directly modulated dual-mode laser," *IEEE Photon. J.*, vol. 7, no. 6, pp. 1400707, Dec. 2015, doi: 10.1109/JPHOT.2015.2498906.

[81] J. S. Suelzer, T. B. Simpson, P. Devgan, and N. G. Usechak, "Tunable, low-phase-noise microwave signals from an optically injected semiconductor laser with opto-electronic feedback," *Opt. Lett.*, vol. 42, no. 16, pp. 3181-3184, Aug. 2017, doi: 10.1364/OL.42.003181.

[82] Y. Chen, S. Liu, and S. Pan, "Multi-format signal generation using a frequency-tunable optoelectronic oscillator," *Opt. Express*, vol. 26, no. 3, pp. 3404-3420, Feb. 2018, doi: 10.1364/OE.26.003404.

[83] X.-D. Lin, Z.-M. Wu, T. Deng, X. Tang, L. Fan, Z.-Y. Gao, and G.-Q. Xia, ”Generation of widely tunable narrow-linewidth photonic microwave signals based on an optoelectronic oscillator using an optically injected semiconductor laser as the active tunable microwave photonic filter,” *IEEE Photon. J.*, vol. 10, no. 6, pp. 5502209, Oct. 2018, doi: 10.1109/JPHOT.2018.2878781.

[84] H. Tang, Y. Yu, Z. Wang, L. Xu, and X. Zhang, ”Wideband tunable optoelectronic oscillator based on a microwave photonic filter with an ultra-narrow passband,” *Opt. Lett.*, vol. 43, no. 10, pp. 2328–2331, May 2018, doi: 10.1364/OL.43.002328.

[85] L. Chen and X. Bao, ”Analytical and numerical solutions for steady state stimulated Brillouin scattering in a single-mode fiber,” *Opt. Comm.*, vol. 15, no. 1-3, pp. 65-70, Jun. 1998, doi: 10.1016/S0030-4018(98)00147-3.

[86] G. P. Agrawal, ”Nonlinear fiber optics,” Fifth Edition, Academic Press 2013, doi: 10.1007/3-540-46629-0.

[87] J. M. Choi, R. K. Lee, and A. Yariv, ”Control of critical coupling in a ring resonator–fiber configuration: application to wavelength-selective switching, modulation, amplification, and oscillation,” *Opt. Lett.*, vol. 26, no. 16, pp. 1236-1238, Aug. 2001, doi: 10.1364/OL.26.001236.

[88] A. Rasoloniaina, V. Huet, T. K. N. Nguyên, E. Le Cren, M. Mortier, L. Michely, Y. Dumeige, and P. Féron, ”Controling the coupling properties of active ultrahigh-Q WGM microcavities from undercoupling to selective amplification,” *Sci. Rep.*, vol. 4, no. 4023, Feb. 2014, doi: 10.1038/srep04023.

[89] R. M. Nguimdo, Y. K. Chembo, P. Colet, and L. Larger, ”On the phase noise performance of nonlinear double-loop optoelectronic microwave oscillators,” *IEEE J. Quant. Electron.*, vol. 48, no. 11, pp. 1415-1423, Nov. 2012, doi:10.1109/JQE.2012.2215843.

[90] K. Saleh, R. Henriet, S. Diallo, G. Lin, R. Martinenghi, I. V. Balakireva, P. Salzenstein, A. Coillet, and Y. K Chembo, ”Phase noise performance comparison between optoelectronic oscillators based on optical delay lines and whispering gallery mode resonators,” *Opt. Express*, vol. 22, no. 26, pp. 32158–32173, Dec. 2014, doi: 10.1364/OE.22.032158.

[91] R. M. Nguimdo, K. Saleh, A. Coillet, G. Lin, R. Martinenghi, and Y. K. Chembo, ”Phase noise performance of optoelectronic oscillators based on whispering-gallery mode resonators,” *IEEE J. Quant. Electron.*, vol. 51, no. 11, pp. 1–8, Oct. 2015, doi: 10.1109/JQE.2015.2488981.

[92] K. Saleh, G. Lin, and Y. K. Chembo, ”Effect of laser coupling and active stabilization on the phase noise performance of optoelectronic microwave oscillators based on whispering-

gallery mode resonators," *IEEE Photon. J.*, vol. 7, no. 1, pp. 1–11, Feb. 2015, doi: 10.1109/JPHOT.2014.2381661.

[93] X. Liu, W. Pan, X. Zou, L. Yan, B. Luo, and B. Lu, "Investigation on tunable modulation index in the polarization modulator-based optoelectronic oscillator," *IEEE J. Quant. Electron.*, vol. 50, no. 2, pp. 68–73, Feb. 2014, doi: 10.1109/JQE.2013.2294378.

[94] Y. Bao, E. Banyas, and L. Illing, "Periodic and quasiperiodic dynamics of optoelectronic oscillators with narrow-band time delayed feedback," *Phys. Rev. E*, vol. 98, no. 6, Dec. 2014, Art. no. 062207, doi: 10.1103/PhysRevE.98.062207.

[95] Y. K. Chembo, "Laser-based optoelectronic generation of narrowband microwave chaos for radars and radio-communication scrambling," *Opt. Lett.*, vol. 42, no. 17, pp. 3431-3334, Aug. 2017, doi: 10.1364/OL.42.003431.

[96] M. Ha and Y. K. Chembo, "Microwave envelope equations for narrowband optoelectronic oscillators," *SPIE Terahertz, RF, Millimeter, and Submillimeter-Wave Tech. and App. XVI*, vol. 12420, pp. 29-34, Mar. 2023, doi: 10.1117/12.2647188.

[97] D. B. Leeson, "A simple model of feedback oscillator noise spectrum," *Proc. IEEE*, vol. 54, no. 2, pp. 329–330, Feb. 1966, doi: 10.1109/PROC.1966.4682.

[98] K. Volyanskiy, Y. K. Chembo, L. Larger, and E. Rubiola, "Contribution of laser frequency and power fluctuations to the microwave phase noise of optoelectronic oscillators," *IEEE J. Light. Tech.*, vol. 28, no. 18, pp. 2730-2735, Sep. 2010, doi: 10.1109/JLT.2010.2064230.

[99] M. Ha and Y. K. Chembo, "Nonlinear dynamics of continuously tunable optoelectronic oscillators based on stimulated Brillouin amplification," *Opt. Express*, vol. 29, no. 10, pp. 14630-14648, May 2021, doi: 10.1364/OE.421861.

[100] M. Ha and Y. K. Chembo, "Quantifying additive and multiplicative noise in optoelectronic oscillators: an experimental and theoretical analysis," *IEEE J. Light. Tech.*, doi: 10.1109/JLT.2024.3388909.